

Microstructure Investigation of Modified Inconel 706 Superalloys after Different Thermal Treatments

vorgelegt von
Diplom-Physiker
Vitaliy Kindrachuk
aus Kyiv, Ukraine

von der Fakultät III - Prozesswissenschaften
der Technischen Universität Berlin
zur Erlangung des akademischen Grades

Doktor der Naturwissenschaften
– Dr. rer. nat. –

genehmigte Dissertation

Promotionsausschuss:

Vorsitzender: Prof. Dr. H. Schubert

Berichter: Prof. Dr. J. Banhart

Berichter: Prof. Dr. J. Rösler

Tag der wissenschaftlichen Aussprache: 09.12.2005

Berlin 2006

D 83

CONTENT

1. Introduction.....	5
2. Experiment and methods	11
2.1 Heat treatments.....	11
2.2 Specimen preparation.....	12
2.3 Experimental methods.....	14
2.3.1 Three dimensional atom probe microscopy	14
2.3.2 Statistical analysis of atom probe data: wavelength dependent filtering (WDF)	19
2.3.3 Electron microscopy	22
2.4 Three dimensional finite element method.....	25
3. Experimental results.....	27
3.1 Inconel 706 superalloy	27
3.1.1 Solution treatment at 980°C for 3 h and 10 h	27
3.1.2 Microstructure after direct ageing.....	30
3.1.3 Microstructure after modified stabilization heat treatment.....	34
3.1.4 Microstructure after modified stabilization heat treatment and after ageing at 750°C for 750 h	39
3.1.5 Microstructure after modified stabilization heat treatment and after ageing at 750°C for 5000 h	42
3.2 Re-containing Inconel 706 superalloy	44
3.2.1 Microstructure after modified stabilization heat treatment.....	44
3.2.2 Microstructure after modified stabilization heat treatment and after ageing at 750°C for 750 h	53
3.3 DT 706 superalloy	61
3.3.1 Microstructure after modified stabilization heat treatment.....	61
3.3.2 Microstructure after modified stabilization heat treatment and after ageing at 750°C for 750 h	65
3.3.3 Microstructure after modified stabilization heat treatment and after ageing at 750°C for 5000 h	69

4.	Calculation of internal coherent stresses and elastic strain energies in Inconel 706 after direct ageing.....	71
4.1	Motivation	71
4.2	Material model.....	72
4.3	Results of FE calculations	75
4.3.1	Mean normal stress and elastic strain energy distribution: case of individual γ' precipitate	75
4.3.2	Mean normal stress and elastic strain energy distribution: case of individual γ'' precipitate	76
4.3.3	Mean normal stress and elastic strain energy distribution: case of individual γ'/γ'' precipitate	77
4.4	Coherency of interfaces.....	80
5.	Discussion	83
5.1	Inconel 706 and its Re-containing modification	83
5.1.1	Microstructure before and after heat treatment	83
5.1.2	FEM analysis	87
5.2	DT 706 as a modified Inconel 706 superalloy	90
6.	Summary	93
	References	97

1 Introduction

The development of stationary gas and steam turbines with high efficiencies above 55 % requires new materials with improved high temperature properties not only for the blades but also for thermally and mechanically high-loaded discs and rotors. This requires in many cases a partial substitution of ferritic steels by nickel-base superalloys. Nowadays the service temperature of industrial steam turbines will be increased up to 700°C - 720°C which cannot be realized without the employment of nickel-base alloys for the hot parts of the turbines. For the production of large wrought parts in particular, the Inconel 706 alloy is suitable and offers an attractive alternative.

The so-called superalloys are materials designed to keep their mechanical properties for extended periods of time in highly oxidizing and corrosive atmospheres at temperatures above 650°C. The range of applications for which superalloys are used includes aircraft and land-based gas turbines, rocket engines, chemical, and petroleum plants, steam power plants, nuclear reactors and petrochemical equipment.

Superalloys are based on Group VIII B elements and usually consist of various combinations of iron, nickel, cobalt, and chromium, as well as smaller amounts of tungsten, molybdenum, tantalum, niobium, titanium, and aluminum. The three major classes of superalloys are nickel-, iron- and cobalt-based alloys. A major subgroup, those that have metallurgical characteristics similar to nickel-base alloys but have relatively large iron contents, consists of the so-called nickel-iron superalloys.

The main advantage of superalloys is their outstanding strength at the service temperature at which gas and steam turbines operate. This is firstly due to their close-packed face centered cubic lattice, which makes these alloys more strong than their body centered counterparts. Secondly, age-hardening due to precipitation of intermetallic or carbide compounds contributes to strength. The highest interest is concentrated on nickel-base and nickel-iron superalloys, as they have better mechanical properties than cobalt-base superalloys because of the γ' precipitation.

In the 1950's the International Nickel Company (INCO) investigated the strengthening effects of various alloying elements in an alloy Inconel 600 [Eiselstein 1991]. This alloy was developed as a high strength steam piping material for steam power plants. The development gave evidence of strengthening effects due to alloying molybdenum and niobium with varying amounts of nickel. This led to the development of Inconel 625 and Inconel 718. Inconel 718 became the alloy most frequently used for rotor aerospace applications [Helms 1996]. However, the development of gas and steam turbines has increased the demand for diameter superalloy billets for rotating components [Helms 1996]. The production of ingots of superalloys was limited in size to 610 mm because of the segregation tendency [Helms 1996]. Therefore, INCO tried to develop a new superalloy that could be

quenched to larger sizes than Inconel 718 without segregation problems [Eiselstein 1970]. The new alloy was expected to have better machinability and to be less expensive than Inconel 718. In that way Inconel 706 was developed. The patent for it was issued by INCO in 1972 [Schilke 1994]. Compared with Inconel 718, Inconel 706 has a chemical composition of no molybdenum, reduced niobium, aluminum, chromium, nickel and carbon, and increased titanium and iron. The reduction of niobium decreases the tendency for segregation. The increase of titanium was made in order to compensate for the decrease of niobium as the primary hardening element. The decrease of aluminum avoids rapid age hardening which could make welding difficult. To lower the cost of Inconel 706 the nickel content was chosen as low as possible. Finally, the produced ingots of Inconel 706 approached 914 mm in diameter [Helms 1996, Schilke 1994].

The most important precipitating phases that occur in Inconel 706 are

- $\text{Ni}_3(\text{Al}, \text{Ti})$ -based γ' , $L1_2$ crystal structure;
- $\text{Ni}_3(\text{Nb}, \text{Ti})$ -based γ'' , DO_{22} crystal structure;
- $\text{Ni}_3(\text{Ti}, \text{Nb})$ -based η , DO_{24} crystal structure.

Sometimes mention of the δ phase (Ni_3Nb -based, DO_a crystal structure) [Moll 1971, Moll 1971a, Kuhlman 1994] can be found in the literature. However, it seems that the δ phase is constituent of the microstructure of Inconel 718 [Sundaraman 1988, Cozar 1991] and not of Inconel 706 [Schilke 1994, Mukherji 2003, Takahashi 1994, Shibata 1997, Härkegard 1997].

The heat treatment conditions and the alloy composition determine whether γ' and γ'' precipitation occurs sequentially or simultaneously [Takahashi 1994, Shibata 1997]. Whether γ' or γ'' is more stable is determined by the atomic ratio $\text{Ti}+\text{Al}$ to Nb [Cozar 1973, Takahashi 2001, Collier 1988]. Cozar and Pineau [Cozar 1973] have reported the morphology evolution of γ' and γ'' precipitates in Inconel 718. The $\gamma'/$ matrix interfaces were found to be favorable nucleation sites for γ'' . After ageing for 8 h at 750°C nearly all the cubic γ' particles have their six faces coated with a layer of γ'' . This morphology is referred to as “compact”. An important observation is that a “compact” morphology can only be obtained if an isolated γ' precipitate has reached a minimum critical size. Otherwise a co-precipitate of “non-compact” type appears (i.e. there are surfaces of a γ' particle not coated with a layer of γ'' phase). Therefore, three different types of precipitates are possible: individual γ' , γ'' and γ'/γ'' co-precipitates. According to [Shibata 1996] the orientation at the γ'/γ'' interface is subjected to the conditions $(001)_{\gamma''} // \{001\}_{\gamma'}$ and $[100]_{\gamma''} // \langle 100 \rangle_{\gamma'}$. The orientation of γ'' to the matrix obeys the same conditions as γ' .

Co-precipitation of “compact” morphology plays an important role for the stabilization of the microstructure of superalloys [Shibata 1997]. Moreover, the mechanical properties (tensile strength, 0.2 % yield strength, hardness, creep rupture life) of Inconel 706 are at most improved due to co-precipitation of “compact” morphology. By investigating the precipitation behavior of Inconel 706 and of its compositional modifications [Shibata 1997] it was shown that co-precipitation occurs only in the presence of both titanium and niobium. Co-precipitation of “compact” morphology happens if the contents of the three strengthening elements confirm to the limits: 1.5 wt.% Ti or more, 1.5 wt.% Nb or more and between 0.3 and 0.5 wt.% Al [Takahashi 2001]. By increasing the Ti+Al to Nb ratio and Al to Ti one can achieve the “compact” morphology [Gou 1994].

Precipitation of the η phase occurs predominantly at the grain boundaries. η grows with extended exposure at elevated temperatures [Takahashi 1994, Shibata 1997]. The η phase has a specific orientation relationship with the γ matrix, namely $(0001)_\eta // (111)_\gamma$ and $\langle 11\bar{2}0 \rangle_\eta // \langle 1\bar{1}0 \rangle_\gamma$ [Speich 1963, Clark 1967]. It has been reported [Zhang 1996, Takahashi 1994] that existence of the η phase at grain boundaries remarkably improves creep strength, although ductility and toughness decrease.

It is known that nickel-iron superalloys are sensitive to stress assisted grain boundary oxidation (SAGBO) at service temperature [Kang 1994, Nazmy 1997]. It was demonstrated [Härkegard 1997] that an Inconel 706 alloy free of η precipitates at grain boundaries, was susceptible to SAGBO. Creep crack growth exceeding 1 mm/h was observed under tensile stress and rupture strains below 1 % were registered. At the same time an alloy with η precipitates at grain boundaries could be subjected to strains above 5 % without rupture. Therefore, η precipitation at grain boundaries stabilizes Inconel 706 against oxidation induced cracking.

Unfortunately, the η phase can nucleate and grow not only intergranularly but also intragranularly. This is undesirable since mechanical properties of the alloy degrade [Heck 1994]. The formation of η precipitates is attributed to transformations of γ [Smith 1953] or γ' [Clark 1967, Remy 1979, Merrick 1962]. η forms intragranularly if it forms via γ' . This is explained by the possibility for the matrix to decrease its elastic stress.

The topic of many actual investigations is to optimize Inconel 706 in order to make it applicable for rotors in steam turbines at temperatures of 700°C or even slightly higher for service times up to 200 000 h. Ageing of the heat treated alloy above 700°C may lead to considerable degradations of alloy properties due to microstructural changes. Optimization refers therefore, to the proper heat treatment and compositional modification of Inconel 706. Presently modifications of the Inconel 706

superalloy, namely rhenium (Re)-containing Inconel 706 and so called DT 706 superalloy are under investigation [DFG 2002]. The Re-alloyed Inconel 706 contains 0.69 at.% (2.23 wt.%) of Re. Rhenium concentrates in the matrix and can significantly reduce coarsening of precipitates by forming pile-ups at phase interfaces [Giamei 1985]. The DT 706 superalloy differs from the pure Inconel 706 alloy in the content of Ti, Al, Ni and Fe. The microstructure of the Inconel 706 superalloy is analyzed after direct ageing (DA) and modified stabilization heat treatment (MST). These heat treatments are the most established heat treatments used for Inconel 706 [Mukherji 2003, Wanderka 2004, Kindrachuk 2004]. For the long time behaviour under service conditions one has to investigate the alloys after ageing at 700°C for 200 000 h. However, 200 000 h is too long time interval. In order to simulate the effect of the long time interval ageing [Mannan 2000, Berger 2001] the alloys are aged at a higher temperature of 750°C, but for a shorter time interval 5000 h. The heat treated alloys are investigated also after ageing at 750°C for an intermediate time interval 750 h. To accomplish the optimization one has to know the microstructure in detail, its effect on the mechanical properties and the development of the microstructure under service conditions.

Therefore, the aims of the present thesis are:

- to investigate in details the microstructure of the superalloys, to analyse the composition of the phases after different heat treatments (DA and MST);
- to understand the morphology development of the precipitates;
- to investigate the microstructure development under service conditions;
- to investigate the influence of Re on the microstructure stability;
- to characterize the microstructural changes due to small deviations in composition of Inconel 706.

The precipitates relevant for the improvement of the alloys Inconel 706 and DT 706, have sizes within nm-range. In order to analyze the composition of such small precipitates quantitatively the three-dimensional atom-probe (3DAP) is used. 3DAP is an analytical method able to map out the three-dimensional distribution of chemical species on a nano-scale and makes it possible to detect precipitates within the reconstructed volume. The technique used for the analysis of microstructure is transmission electron microscopy (TEM). In order to understand the reason for co-precipitation and to predict the morphology evolution of precipitates, finite element analysis (FEM) is applied.

Chapter 2 describes the experiments: heat treatments, preparation of specimens and the experimental methods used. The experimental results are presented in Chapter 3. The results are given separately for Inconel 706, for Inconel 706 alloyed with rhenium and for the DT 706 alloy. The

FEM analysis of elastic stresses and strains in Inconel 706 after the DA heat treatment is given in Chapter 4. The results are discussed in Chapter 5 and summarized in Chapter 6.

2 Experiment and methods

2.1 Heat treatments

The nominal composition of all the alloys investigated is shown in Table 2.1. Chemical compositions presented in this work are given in atomic percent. All heat treatments are represented in Fig. 2.1. Inconel 706 was solution-treated at 980°C for 3 h, stabilized at 820°C for 10 h and then double-aged at 720°C for 8 h and at 620°C for 8 h (Fig. 2.1a). In the following this heat treatment will be called the modified stabilization heat treatment MST [Mukherji 2003, Wanderka 2004]. The modified stabilization heat treatment for DT 706 alloy (MST/DT) differs slightly from that of Inconel 706. The samples were solution-treated at 1000°C for 3 h, stabilized at 835°C for 10 h and then aged at 720°C for 8 h (Fig. 2.1b). In addition, after the MST heat treatment, Inconel 706 and DT 706 samples were aged at 750°C for 750 h (MST750 and MST750/DT respectively) and for 5000 h (MST5000 and MST5000/DT respectively).

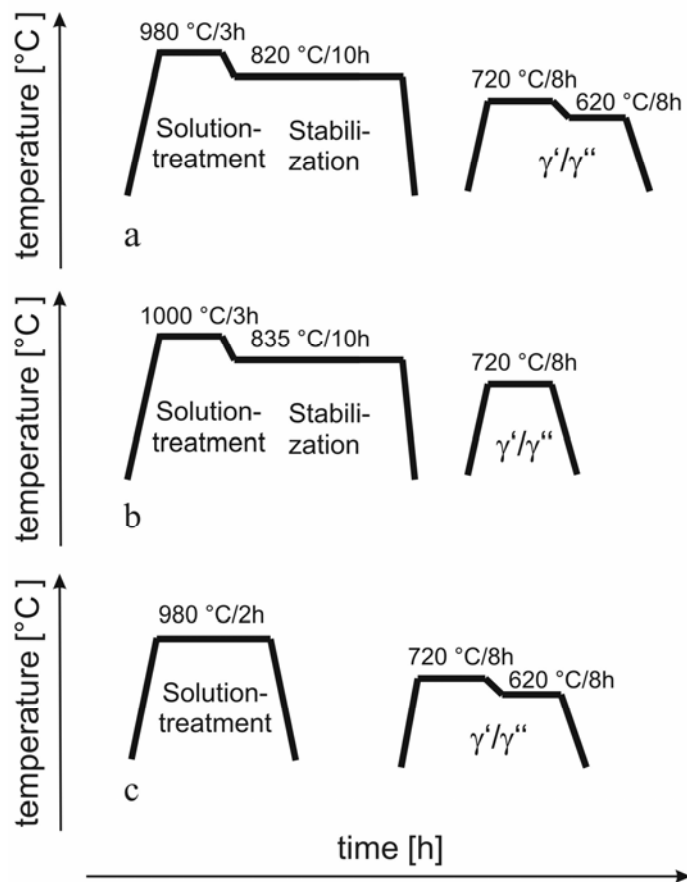


Fig. 2.1 (a) MST, (b) MST/DT and (c) DA heat treatments.

Table 2.1. Nominal composition of Inconel 706, Re-containing Inconel 706 and DT 706 superalloys in at.%.

	Ni	Al	Ti	Nb	Cr	Fe	Re
Inconel 706	40.68	0.44	1.85	1.87	17.52	37.63	-
Inconel 706-Re	44.9	0.42	2.04	1.92	17.6	32.4	0.69
DT 706	52.01	1.2	2.21	1.84	19.64	23.1	-

Inconel 706 was also studied after direct ageing (DA). Using DA the alloy was solution-treated at 980°C for 2 h and then double-aged at 720°C for 8 h and at 620°C for 8 h (Fig. 2.1c).

2.2 Specimen preparation

Preparation for the three dimensional atom probe (3DAP)

An analysis by means of the 3DAP requires specimens shaped as very sharp needles with a uniform cross section. The end radius of the tip of the specimen should be between 20–50 nm [Miller 1989]. First the material to be examined was cut into plates of about 250 μm thickness and an area of about 1–2 cm^2 by a circular corundum saw. Both sides of the plates were polished using emery wheels with gradually increasing graining from 600 to 2400. Then they were cut with a diamond wire saw into small rods, with almost quadratic cross-section. After this the rods were cleaned in an ultrasonic bath with acetone. The small rods were then rolled between two pieces of emery paper in order to round off the corners. The almost round rods were clamped in small copper tubes, approximately 13 mm long. The further preparation of the specimens was accomplished by electrochemical polishing at room temperature in two steps.

The electrolyte used for the first polishing was 15 % perchloric acid, balance acetic acid. The electropolishing process is shown in Fig. 2.2. The applied voltage between the specimen and the platinum cathode was 10–15 V. The strongest material removal from the surface of the specimen takes place in the vicinity of the air-electrolyte boundary. Therefore, moving the electrolyte up and down along the specimen produced a necked region, called the “waist”.

The second stage of the electropolishing process produces fine tips using the micropolishing technique shown in Fig. 2.3. The counter electrode is a platinum wire loop, about 2 mm in diameter. The loop is filled with electrolyte 2 % perchloric acid, balance butoxyethanol. The specimen and the wire loop are mounted on a micromanipulator. The electropolishing is observed through a low power

(31x) optical microscope. The pulse voltage used varies from 5 to 10 V. The pulses length can be set manually, with the optimal duration found to lie in the range 0.01–0.1 s. The polishing voltage was turned off immediately after formation of a fine tip, which is carefully cleaned in methanol in order to prevent any etching of the tip by the residual electrolyte.

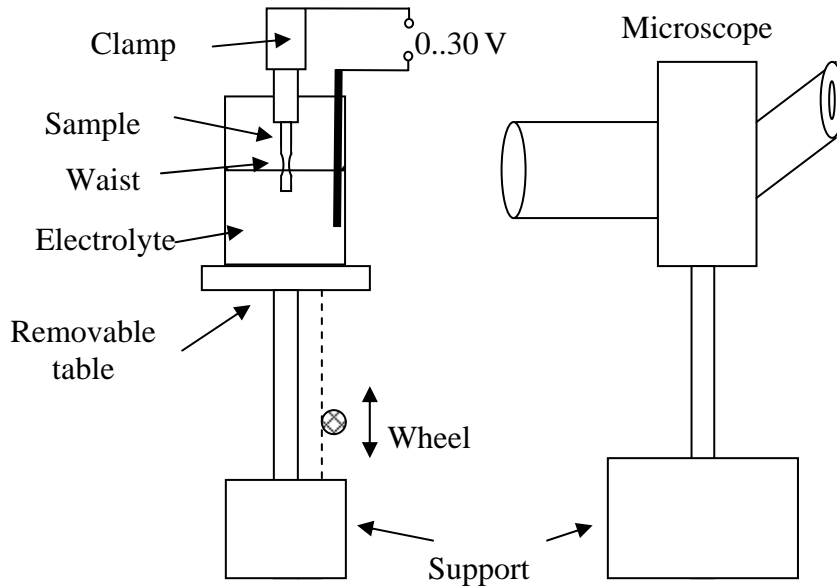


Fig. 2.2 The first stage of the electropolishing process. The specimen is moved slowly up and down. This step produces a necked region in the center of the blank.

Once prepared, specimens were examined in the transmission electron microscope (TEM). A TEM micrograph of a suitable tip is represented in Fig. 2.4. The specific features of interest such as geometry of the tip, grain boundaries and precipitates in the apex region can be observed. Only part of the apex can be analyzed in the 3DAP. The second stage of electropolishing can be repeated once more if the tip is not sharp enough for the 3DAP experiment or if the apex does not contain any features of interest.

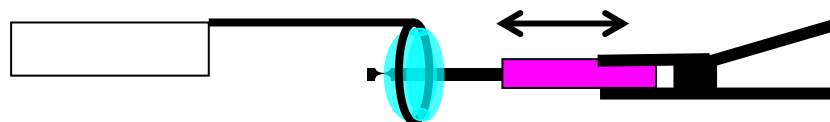


Fig. 2.3 Micropolishing is the second stage of the electropolishing process. Micropolishing is continued until the weight of the left part of the blank is too heavy to be supported by the thin neck.

Preparation for the transmission electron microscopy

For TEM observation disks of 3 mm in diameter and 250 μm thick were punched out of the samples to be examined. Both sides of the disks were polished down to 100 μm thickness using emery wheels with gradually increasing graining from 1200 to 4000.

Finally, thin foils were prepared by electropolishing (TENUPOL-3, STRUERS) in a solution of 10 % perchloric acid and 90 % ethanol with 7 g thiourea at a temperature between -20°C and -15°C . The applied voltage was 20 V, the current was in the range 48–84 mA. Usually approximately 5 specimens of each investigated condition were prepared for TEM analysis. The polishing device switches off automatically as soon as a hole in the middle of the sample appears. TEM observations were carried out using a Philips CM30 and a EM400 microscopes.

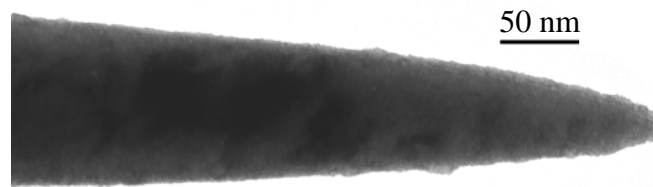


Fig. 2.4 TEM micrograph of a tip which is suitable for 3DAP.

2.3 Experimental methods

2.3.1 Three dimensional atom probe microscopy

The three-dimensional atom-probe is an analytical microscope able to map out the three-dimensional distribution of chemical species on an atomic scale [Kellogg 1980, Cerezo 1988, Bostel 1989, Blavette 1993, Leisch 1994]. 3DAP makes it possible to measure quantitatively the composition in a small region that can be selected arbitrarily in the reconstructed volume. In the present work, a three-dimensional atom probe was used to carry out a high resolution microchemical analysis.

The three-dimensional atom probe is a combination of two parts, a field ion microscope (FIM) [Müller 1960, 1965, 1969] and a time-of-flight (TOF) mass spectrometer [Miller 1989, 1996]. These techniques are described in the following.

The **field ion microscope** enables a stereographic image to be obtained of the surface of a fine tip (specimen) with very high resolution. This conducting needle-like tip should have an end radius of typically 50–100 nm, being prepared employing electrochemical polishing. The tip is maintained at a cryogenic temperature 60 K in order to reduce the transverse velocity of the imaging gas atoms. The

image is obtained due to ionization of image gas atoms on a fluorescent screen. The procedure is as follows. A small amount of an inert gas ($10^{-4} - 10^{-3}$ Pa), usually He or Ne, is admitted into the FIM. Then a high electric field is applied to the tip. The atoms of the selected image gas become polarized by the inhomogeneous electric field and are drawn towards the surface of the tip. If the electric field is high enough, the trapped atoms of the image gas may become field ionized. In this process, an electron from a gas atom tunnels through the surface potential barrier into a vacant energy level in the specimen, leaving a positively charged gas ion near the surface. In order to reach this ionization, the electric field is typically between 20 and 50 V/nm [Wagner 1982, Miller 1996]. The electric field at the apex of a tip is inversely proportional to the radius of the apex. Therefore, it is necessary to reduce the end radius of the tip to reach the required electric field. The corresponding applied voltage is between 5 and 10 kV if the radius of the apex is 20–50 nm. The positive image gas ions are accelerated and fly away from the specimen towards the channel plate where the field ion image is formed. It corresponds approximately to the projection of the surface structures of the tip by means of atomic resolution on the screen. The magnification M of the projected surface is

$$M = \frac{R}{r \cdot \beta}.$$

The distance between the tip and the channel plate is R , r is the apex radius and β is the compression coefficient of the image, which describes the deviation from the stereographic projection and has the value of 1.8 in our microscope. Thus, a projected image of the needle tip can achieve magnifications of $10^5 - 10^7$.

The typical image of a field evaporated, single crystal specimen consists of a number of spots, arranged in intersecting sets of concentric rings. These rings correspond to the atomic terraces of prominent crystallographic planes on the specimen surface. Bright spots correspond to ionization above the ledge and corner atoms on these planes. The overall pattern resembles a stereographic projection of the surface, which can be indexed using standard crystallographic techniques [Drechsler 1960]. The image contrast from alloys and two-phase materials do not usually show distinct rings, as are observed for pure metals.

If the electric field is increased to a sufficiently high value, atoms are removed from the surface by field evaporation. It is important that the applied electric field is higher than the critical evaporation field, which depends on the chemical composition of a phase. The field evaporation rate can be well controlled so only a few atoms are removed from the surface.

An atom probe experiment is started with producing a field ion image in order to smooth the surface of the tip and to align the specimen in the correct position for the experiment. The schematic principle of the 3DAP is presented in Fig. 2.5. After removing the image gas, the 3DAP experiment

can be started. The surface atoms are field evaporated by applying an additional voltage to the specimen in form of a series of high voltage pulses with nanosecond rise time. The pulse fraction used was 20 %, and the pulse repetition rate was 1 kHz. The ionized atoms are removed from the surface and are analyzed in the time of flight mass spectrometer when they arrive at the detector. The 3DAP detector CAMECA consists of a microchannel plate (MCP) and a 10 cm x 10 cm detector, which consists of an array of 100 multianodes with a parallel time recording system. The incident ions generate secondary electrons, which undergo rapid multiplication as they are accelerated through the channel plate. The cloud of electrons flies then towards the multianode detector and strikes against several anodes. The lateral arrangement of the evaporated ion can be precisely determined if at least three anodes are hit [Blavette 1996]. The calculation of the center of the charge-cloud yields the lateral position of the evaporated ion. Based upon the distance between the tubes of the MCP, only 60 % of evaporated ions are analyzed by the 3DAP detector.

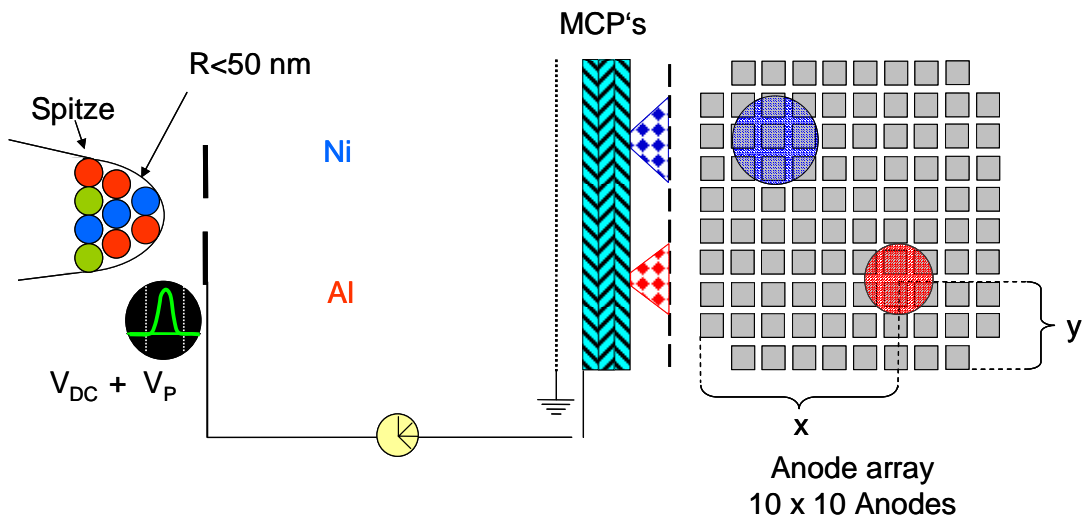


Fig. 2.5 Schematic diagram of the 3DAP.

Knowing the time-of-flight t one obtains the mass-to-charge state ratio m/n for each detected ion

$$\frac{m}{n} = \frac{2e \cdot U_{tot} \cdot t^2}{d^2},$$

where U_{tot} is the total voltage (direct current and pulses) applied to the specimen, d is the distance travelled by the ion from the specimen to the TOF detector, e is the elementary charge. By this means, the chemical analysis can be performed.

The arrangement of atoms along the axis of the tip can be determined during the evaporation process. An uniform evaporation of the specimen is possible due to the computer control of the direct

voltage applied to the specimen, so that the field evaporation rate (number of ions per number of pulses) remains approximately constant. In conclusion, the 3DAP microscope permits the elemental reconstruction of a small volume of the specimen with the near atomic resolution.

The lateral resolution on the surface of the specimen is possible only with an accuracy of about 0.5 nm [Miller 1989] since the electric field distribution is not known exactly, so deviations from the assumed ion trajectories occur. The depth resolution is determined by the distance between the atomic planes and is about 0.2 nm [Deconihout 1995].

The 3DAP reconstruction as well as different statistical analyses were done using the visualization program *AVS Version 5.3 of Advanced Visual System Inc.* The atoms of the examined volume are spatially displayed on the screen of the computer. The data must be further processed applying statistical methods in order to extract useful physical information.

Mass spectra

The mass spectrum shows the total number of observations of each mass-to-charge ratio. An example of a mass spectrum of a γ' precipitate in Inconel 706 is shown in Fig. 2.6. However, the chemical information derived from the mass spectra can be ambiguous if a peak consists of overlapping isobars. This overlap introduces some uncertainty for the identification of an individual ion and needs correction for the determination of the composition of the alloy (of the matrix, in the present example). Three overlaps occur in the mass spectra of Inconel 706 and DT 706 superalloys. Fe and Cr share a common isobar, ^{54}Fe and ^{54}Cr . Therefore, the peak at mass-to-charge 27 is the overlap $^{54}\text{Fe}^{2+}/^{54}\text{Cr}^{2+}$. In a similar manner the peak at 25 is the overlap $^{50}\text{Ti}^{2+}/^{50}\text{Cr}^{2+}$. The peak at 31 is also an overlap, however because of different charge states $^{62}\text{Ni}^{2+}/^{93}\text{Nb}^{3+}$. It should also be noted that complex combinations with hydrogen like $(\text{AlH})^{2+}$ can also occur. The latter forms the peak at 14.

In order to determine the composition, the correction should be made based on the abundance of all isotopes of the overlapping elements. The deconvolution of the number of atoms in the overlapping peaks in the mass spectrum was done as following

$$\begin{cases} \# \text{Ti}(25) = \frac{\# \text{Ti}(23) + \# \text{Ti}(23.5) + \# \text{Ti}(24) + \# \text{Ti}(24.5)}{8\% + 7.5\% + 73.7\% + 5.5\%} \cdot 5.3\%, \\ \# \text{Cr}(25) = \frac{\# \text{Cr}(26) + \# \text{Cr}(26.5)}{83.8\% + 9.5\%} \cdot 4.35\%, \end{cases}$$

$$\left\{ \begin{array}{l} \#Cr(27) = \frac{\#Cr(26) + \#Cr(26.5)}{83.8\% + 9.5\%} \cdot 2.36\%, \\ \#Fe(27) = \frac{\#Fe(28) + \#Fe(28.5)}{91.73\% + 2.14\%} \cdot 5.82\%, \end{array} \right.$$

$$\left\{ \begin{array}{l} \#Ni(31) = \frac{\#Ni(29) + \#Ni(30) + \#Ni(30.5) + \#Ni(32)}{67.8\% + 26.4\% + 1.16\% + 0.95\%} \cdot 3.71\%, \\ \#Nb(31) = \#(^{62}Ni^{2+} / ^{93}Ni^{3+}) - \#Ni(31). \end{array} \right.$$

The assignment of peaks in the mass spectrum was accomplished by defining mass-to-charge windows for each element such that all the ions with mass-to-charge ratios within a specific mass range are said to be of the type of elements assigned to that window.

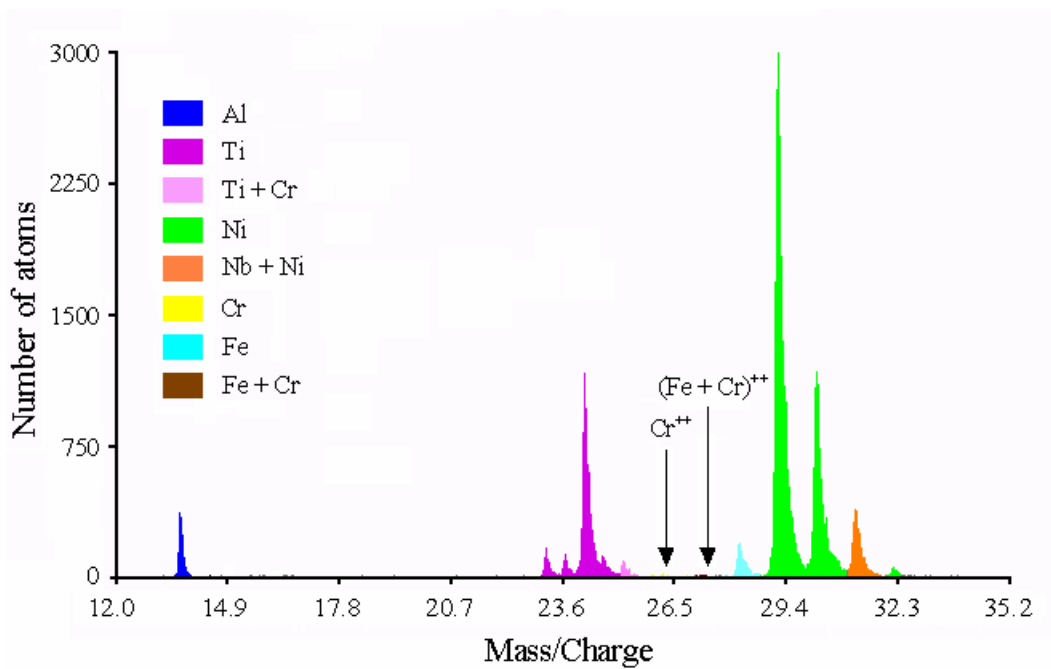


Fig. 2.6 Mass spectrum of a γ' precipitate in Inconel 706.

Reconstruction of atoms

After identification of the ions, each ion is assigned a color based on elemental identity. In this way the arrangement of each species of atoms (or of ions with mass-to-charge ratios within a specific mass window) can be displayed in the three-dimensional reconstruction. The AVS program allows to display the arrangement of several species of atoms simultaneously.

Depth profile

A depth profile (known also as composition profile or concentration depth profile) is the sequence of average compositions obtained by dividing the ion-by-ion sequence into blocks of a fixed depth

containing the atoms of the material removed from the specimen [Wagner 1982]. The choice of this fixed depth is a compromise between minimizing the statistical sampling noise and maintaining the spatial resolution. If the fixed depth is too large, then the information is lost because data are averaged. Therefore, in each individual case the task is to choose a proper value of the fixed depth in order to gain meaningful physical or chemical information.

Such depth profiles were used to obtain the chemical gradients across the interfaces γ/γ' , γ/γ'' and γ'/γ'' . The depth profiles are taken along a box which is selected in such a way that the interface of interest is cut perpendicularly. The box is then divided into slices. The concentration is calculated in each slice and is plotted versus the corresponding depth of a slice. The distance between two adjacent slices is called the moving step and can be varied. In this manner one builds depth profiles through the interfaces. The calculated statistical error of the concentration in a slice is

$$2\sigma = 2 \cdot \sqrt{\frac{c(1-c)}{N}}, \quad (2.1)$$

where c is the concentration value in the slice and N is the total number of atoms in the slice. This formula is also valid for calculating the error of the concentration value of a given element in a precipitate. The concentration is calculated in a box which is fully located inside the reconstructed precipitate. In that case N is the total number of atoms in the box.

2.3.2 Statistical analysis of atom probe data: wavelength dependent filtering (WDF)

The 3DAP offers the possibility to determine the composition in regions of nanometer size. However, such small regions contain only a small number of atoms. Consequently, the actual concentration will vary even in the case of macroscopic homogeneity because of statistical fluctuations. For example, let us consider a binary alloy of 50 at.%. If the measurement of the concentration is performed in a region of one cubic nanometer (which contains about 100 atoms), then the uncertainty of the result amounts to 10%. This is evident from (2.1). Therefore, in order to detect non-random, i.e. chemically relevant concentration fluctuations on the nanometer scale it is necessary to evaluate the experimental data by means of statistical tools which separate the non-statistical concentration fluctuations from the statistical noise and yield quantitative information [Wagner 1982, Miller 1996]. The WDF method was developed to solve such tasks [Czubayko 2000]. The method is based on a Fourier analysis of the data.

The WDF analysis can detect small quasi-periodic deviations from a statistically random, i.e. homogeneous distribution of atoms by comparison of the variances $\sigma_{\text{ran}}^2(L)$ of a random distribution with that of the experimental data $\sigma_{\text{exp}}^2(L)$ after averaging over a systematically increasing length scale

L . However, the WDF method does not characterize the exact shape of the non-random fluctuations. It provides the characteristic properties, wavelength and amplitude, of its prominent Fourier component. A non-random concentration fluctuation occurs if the reduced deviation $\Sigma^2(L) = \frac{\sigma_{\text{exp}}^2(L) - \sigma_{\text{ran}}^2(L)}{\sigma_{\text{ran}}^2(L)}$ exceeds the expected statistical uncertainty (see Fig. 2.7). For such a fluctuation with the concentration amplitude of ΔC and the wavelength λ the reduced deviation exhibits a peak with a maximum at $L = \lambda$. At this maximum

$$\Delta C = \Sigma^2(\lambda) \cdot \sigma_{\text{ran}}^2(L) \cdot \sqrt{\left(\frac{e\pi}{2}\right)^3}. \quad (2.2)$$

A commonly used method to detect deviations from randomness is the analysis of the frequency distribution. Here, the frequency to find given numbers of atoms of a particular species among a fixed number of all alloy atoms is compared with the frequency to find these atomic species in a hypothetical, homogeneous alloy of the same average concentration. A χ^2 – test reveals the deviation from a random distribution. However, this test does not give details like the concentration amplitude or wavelength of the non-stochastical fluctuations. The preference in the present work is given to the WDF method.

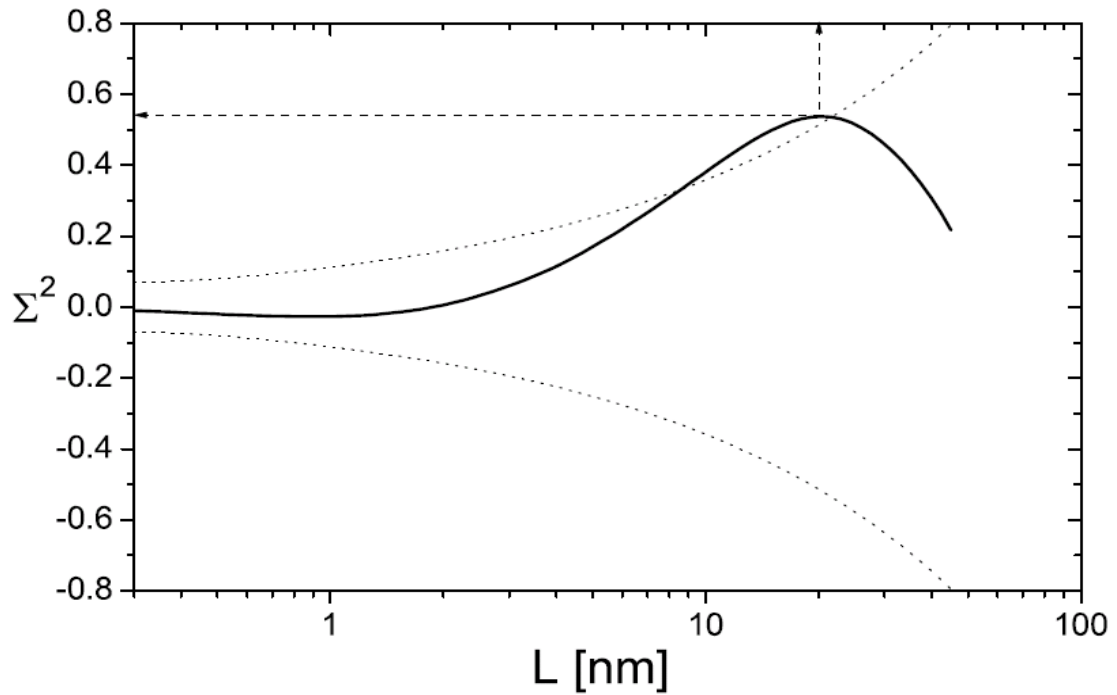


Fig. 2.7 WDF analysis of the Re distribution in the γ matrix of the nickel-base superalloy Re31 [Rüsing 2002]. The maximum indicates, that Re is heterogeneously distributed in the γ matrix with a principal wavelength of 20 nm. Accordingly to (2.2), the root-mean-square amplitude of this distribution amounts to $\Delta C_{\text{Re}} \cong 3.6 \text{ at.}\%$. The dashed lines indicate the expected statistical uncertainty.

2.3.3 Electron microscopy

Fig. 2.8 presents a diagram of the principal emissions from an electron bombardment on a solid sample: secondary electrons (SE), backscattered electrons (BSE), transmitted electrons (TE), elastically and in-elastically scattered electrons, characteristic X-rays. An overview of the methods can be found in [Bethge 1987, Reimer 1997]. The scanning electron microscope (SEM) works by bouncing electrons off the surface and forming an image from SE and BSE. These electrons are collected by a positively charged detector. TE are used in transmission electron microscopy (TEM). TEM and SEM allow a good deal of analytical data to be collected in addition to the formed image. In particular, radiated X-rays have unique, discrete energy values characteristic of the atomic structure of the atom from which they emitted. If one collects these X-rays and analyzes their energy the method is called energy dispersive X-ray analysis (EDX). Characteristic X-rays make a qualitative and a quantitative analysis of elements in solid specimens possible. Combining the information from TEM or SEM together with the X-ray information allows for a complete mapping of an object's surface.

Electron microscopy was used in the present work as an important supplementary technique.

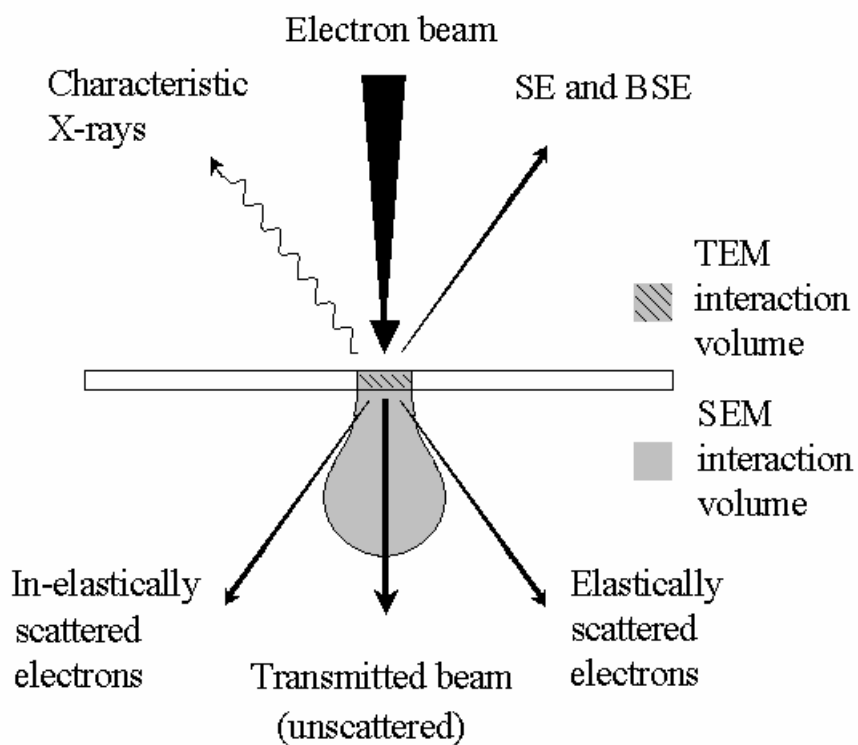


Fig. 2.8 A diagram showing the most important interactions between a beam of high-energy incident electrons and a piece of matter (the specimen). TEM samples should be thin enough to be beam transparent. On the contrary, SEM samples should be thick enough, to allow for a complete absorption of the primary beam. The size of the corresponding SEM interaction volume is of a few cubic micrometers, depending on the sample material and the acceleration voltage.

Transmission electron microscopy (TEM)

The investigations were carried out using two transmission electron microscopes of a Philips: CM 30 and EM 400. The EM 400 TEM was mainly used for tests of the tips quality after electropolishing. It is equipped with a tungsten-cathode and is operated with an acceleration voltage of 120 kV. The EM 400 microscope permits tilting a specimen by $\pm 45^\circ$ around the X-axis and by $\pm 30^\circ$ around the Y-axis. Its point resolution is of 0.5 nm.

The conventional TEM specimens were analyzed in the CM 30. The acceleration voltage of the microscope is 300 kV. Electrons are emitted by a LaB_6 hairpin cathode. The spherical aberration is strongly reduced to 1.2 nm due to a super-twin lens. This increases the point resolution up to 0.2 nm and the lattice resolution to 0.14 nm. The TEM CM 30 is equipped with a detector for EDX analyses, allowing to determine the chemical composition of phases.

High resolution transmission electron microscopy (HRTEM) was used at the TEM Tecnai F20 (FEI Company) for the structural characterization of nano-regions in a crystal. Single atomic planes can be directly observed due to the HRTEM. HRTEM micrographs can be obtained only from very thin specimens, whose thickness does not exceed 40 nm. All the HRTEM micrographs shown in this work are images along the $\langle 100 \rangle$ zone axis.

Dislocations can be well observed with TEM. They can be imaged under two-beam conditions [Hirsch 1965a]. A feature of dislocation images is the invisibility of dislocations in BF and DF images when $g \cdot b = 0$, where g is the reciprocal lattice vector for the operative reflecting plane and b is the Burgers vector. This condition also determines the ratio of invisible dislocations [Hirsch 1965a]. In general, the contrast of dislocations in TEM images has the nature of strained contrast.

Electron diffraction

The microscope produces a diffraction pattern from a specific region of the specimen. In all cases in which quantitative information about the microstructure of the material is required, diffraction patterns and images are correlated. Crystalline materials give very strong electron diffraction patterns. The γ' , γ'' and η precipitates in the Inconel 706 and DT 706 superalloys are ordered phases which produce extra spots in the diffraction pattern. The spots arise from the atomic ordering of the phases. These spots may be used to check the crystal structure and its orientation relationship with the matrix.

Energy dispersive X-ray analysis (EDX)

EDX offers nano-scale information of the chemistry of materials. As the energy of the incident electrons increases above 1 kV they are able to interact with the inner shells of specimen atoms. This causes an orbital electron to jump from a lower energy level shell to a higher energy shell. When it drops back, a quantum of energy in the form of a “hard” or short-wavelength X-ray is emitted. Electron transitions from one shell to another involve precise energy quanta, so that the emitted X-ray is of a very well-defined wavelength or energy. Because the transition energies differ for each individual atomic species, the emitted wavelengths are characteristic of the atoms forming the specimen. By measuring the wavelength or energy of each of the emitted X-rays with an X-ray spectrometer, a qualitative analysis of the atoms composing the specimen may be made. If the relative intensity of the particular X-ray corresponding to a particular atomic species is measured, a quantitative analysis of the specimen can be made.

The Cliff-Lorimer method [Cliff 1975] was used to carry out the quantitative analysis. Cliff and Lorimer have observed that matrix corrections are not needed for analyzing very thin films because self-absorption in the film is negligible. In this case, peak intensities are proportional to concentration and specimen thickness. They removed the effects of variable specimen thickness by taking ratios of intensities for elemental peaks and introduced a “K-factor” in order to relate the intensity ratio to concentration ratio:

$$\frac{C_A}{C_B} = K_{AB} \cdot \frac{I_A}{I_B},$$

where I_A (or I_B) is the peak intensity for element A (or B respectively) and C_A (or C_B) is the concentration in weight percent or mass fraction. Each pair of elements requires a different K-factor which depends on detector efficiency, ionization cross section and fluorescence yield of the two elements concerned. An individual K-factor relates the concentration of two elements to their X-ray peak intensities. When more than two elements are to be analyzed, a number of K-factors can be derived by using external standards to relate known concentrations with measured intensities.

It should be noted that K-factors depend on experimental conditions (time of measurement, intensity, applied voltage, size of the electron beam). Therefore, the calibration measurements on the solution treated Inconel 706 were carried out under the same experimental conditions as the measurements on Inconel 706 and DT 706 superalloys by means of the EDX analysis, namely applied voltage 300 kV, impulses per second 2000 – 3000, time of measurement 100 s, size of the electron beam 10 or 20 nm. The derived K-factors are listed in Table 2.2. The lateral resolution of the EDX analysis is determined by the size of the electron beam. Therefore, the EDX analysis was used to

measure the chemical composition of the η precipitates, the sizes of which are of the order of a few micrometers.

Table 2.2. K-factors for the quantitative analysis of elements derived from test measurements.

Element	Ni	Al	Ti	Nb	Cr	Fe
K-factor	1	1.23	0.76	1.99	0.8	0.89

2.4 Three dimensional finite element method

The term “finite element” was first used by Clough [Clough 1960] in the context of plane stress analysis and has been in common usage since that time. The finite element method (FEM) is a computational technique used to obtain approximate solutions of boundary value problems in engineering. Simply stated, a boundary value problem is a mathematical problem in which one or more dependent variables must satisfy a differential equation everywhere within a known domain of independent variables and satisfy specific conditions at the boundary of the domain. Boundary value problems are also sometimes called field problems. The field variables are the dependent variables of interest governed by the differential equation. The boundary conditions are the specified values of the field variables (or related variables such as derivatives) at the boundaries of the field. Depending on the type of physical problem being analyzed, the field variables may include physical displacement, temperature, heat flux, fluid velocity etc. [Hutton 2004].

The 3D FEM analysis was done using program *Mentat Version 2003 of MARC Analysis Research Corporation*. Certain steps in formulating a finite element analysis of a physical problem are common to all such analyses, whether structural, heat transfer, fluid flow, or some other problem. These steps are embodied in commercial finite element software packages. The steps are preprocessing, solution and postprocessing. The preprocessing step is described as defining the model and includes:

- definition of the geometric domain of the problem;
- definition of the element type to be used;
- definition of the material properties of the elements (physical laws);
- definition of the physical constraints (boundary conditions) and loadings.

The meshed geometric domain, used in the present work for the analysis of stresses around and within a γ' precipitate, is shown in Fig. 2.9. The boundary conditions can be applied according to the task.

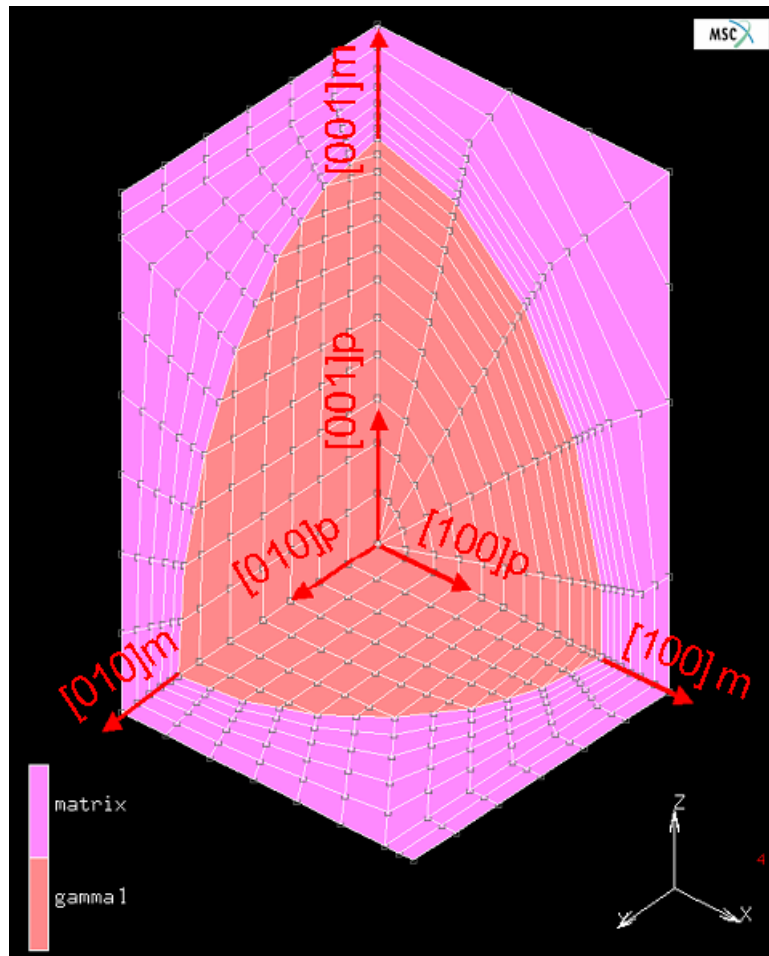


Fig. 2.9 The meshed geometric domain, used in the present work for the analysis of stresses around and within a γ' precipitate. The arrows show the crystallographic directions of the phases. The direction $[100]_p$ denotes the $[100]$ direction of the γ' precipitate whereas $[100]_m$ denotes the $[100]$ direction of the γ matrix, and so on. The finite elements to be used are 8-noded three dimensional bricks and 6-noded prisms. The orange elements correspond to the precipitate, the pink elements correspond to the matrix.

The finite element software solves the governing algebraic equations in matrix form and computes the unknown values of the primary field variable, i.e. displacement.

Analysis and evaluation of the solution results is referred to as postprocessing. An important objective is to judge whether the results are physically reasonable. Postprocessing also includes visualization of deformed structural shapes, stresses and elastic strain energies.

3 Experimental results

3.1 Inconel 706 superalloy

3.1.1 Solution treatment at 980°C for 3 h and 10 h

The specimens after solution heat treatment for 3 h and for 10 h were investigated by TEM with the aim to compare the dislocation density. This is important since the dislocations can act as heterogeneous sites for the nucleation of precipitates in solids [Cahn 1957, Christian 1965]. The TEM images (see. Fig. 3.1) were produced under two-beam dynamical conditions [Edington 1976] so that dislocations are clearly recognized. Corresponding electron diffraction patterns and directions of g vectors are indicated in the insets. The dislocation density is calculated as the number of intersections with the foil surface in an area of 1 cm^2 . The proportion of invisible dislocations is also taken into account according to [Hirsch 1965]. As a result the dislocation density amounts to $6 \cdot 10^8\text{ cm}^{-2}$ for the specimen treated for 3 h and $3 \cdot 10^8\text{ cm}^{-2}$ for the specimen treated for 10 h. In other words the dislocation density reduces by a factor of 2 after solution heat treatment for 10 h as compared to that for 3 h.

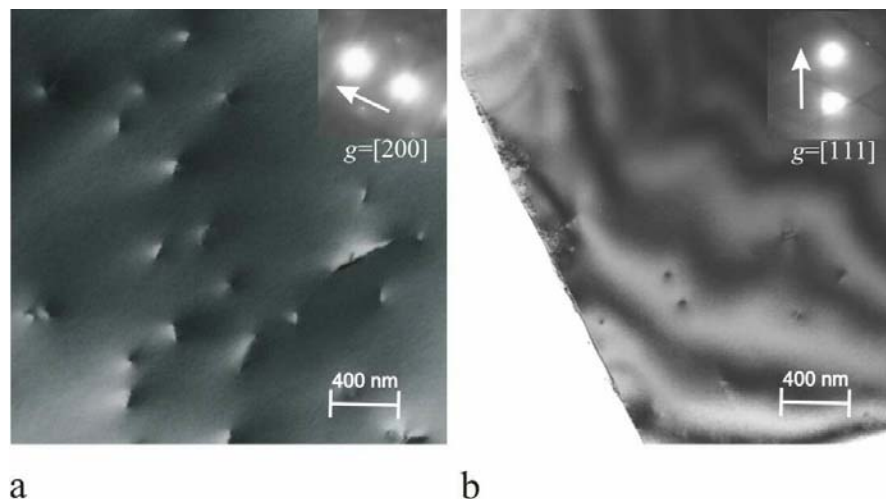


Fig. 3.1. Bright field images of dislocations in Inconel 706 superalloy after solution treatment at 980°C for (a) 3 h and for (b) 10 h. The images were done under two-beam conditions. The diffraction patterns and corresponding directions of g vectors are given in the insets.

The results of 3DAP characterizations of the alloy, after solution treatment for 3 h and for 10 h, are represented in Fig. 3.2. The reconstruction of Nb atom positions was done in a volume of $13.4 \times 13.4 \times 270 \text{ nm}^3$ for the specimen solution treated for 3 h and in a volume of $10.2 \times 10.2 \times 427 \text{ nm}^3$ for the specimen solution treated for 10 h. As the elements should be uniformly distributed in the whole alloy after solution heat treatment it is useful to compare the nominal composition of the alloy with the measured concentrations by atom probe. The measured volume contains 38.52 at.% Ni, 0.69 at.% Al, 2.69 at.% Ti, 2 at.% Nb, 18.34 at.% Cr and 37.73 at.% Fe. These values are in agreement with the nominal composition except of the value for Ti which is slightly too high.

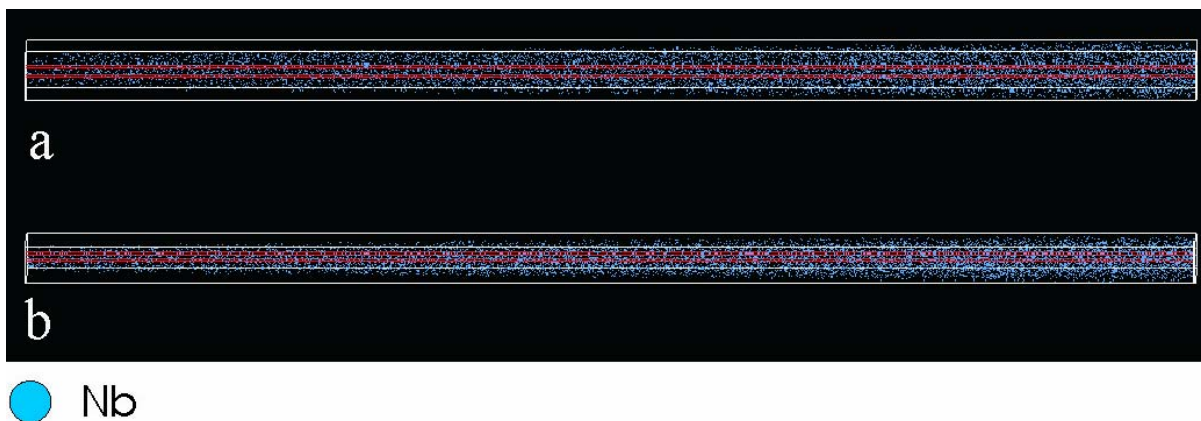


Fig. 3.2. Three-dimensional reconstruction of Nb atom positions in Inconel 706 alloy after solution treatment at 980°C for (a) 3 h (only 50 % of the measurement is shown in a volume of $7.8 \times 7.8 \times 181 \text{ nm}^3$) and for (b) 10 h (only 40 % of the measurement is shown in a volume of $7.8 \times 7.8 \times 241 \text{ nm}^3$). Only parts of the measurements are shown since the reconstructed volumes are too long. The red boxes are used for WDF analyses.

The 3D reconstructions of Nb atoms do not show any obvious inhomogeneity. The reconstruction of other alloying elements gives similar images, where the density of points depends on the concentration of elements. A visual analysis of depth profiles (not shown here) through the reconstructed volumes is not useful because it does not give evidence on the spatial distribution and strength of the detected heterogeneity. After applying a conventional statistic techniques such as frequency distribution of element concentrations for atom probe data, the alloy after solution heat treatments seems to be homogeneous. On the other hand wavelength dependent filtering (WDF) reveals that this alloy indeed contains nonrandom concentration fluctuations. Fig. 3.3 presents plots of the reduced variance together with the expected statistical uncertainty using the same sample volume as shown in Fig. 3.2 (namely the red boxes were used for the WDF analysis).

After solution heat treatment at 980°C for 3 h the fluctuations of Al and Ti lie in the range of statistical oscillations (Fig. 3.3a). However this is not the case for Ni and for Nb. The maximum of Σ^2 for Ni at 2–3 nm indicates that Ni is heterogeneously distributed in the matrix with a principal wavelength of 2–3 nm. The root-mean-square amplitude of this quasi-periodic distribution was estimated from the height of the maximum and amounts to $\Delta C_{Ni} \cong 4.4$ at.%. Nb experiences light decomposition with two principal wavelengths of 10 nm and longer than 133.5 nm (i.e. longer than the half length of the reconstructed volume). The corresponding concentration amplitudes are $\Delta C_{Nb}(10 \text{ nm}) \cong 0.7$ at.% and $\Delta C_{Nb}(> 133.5 \text{ nm}) \cong 0.4$ at.%.

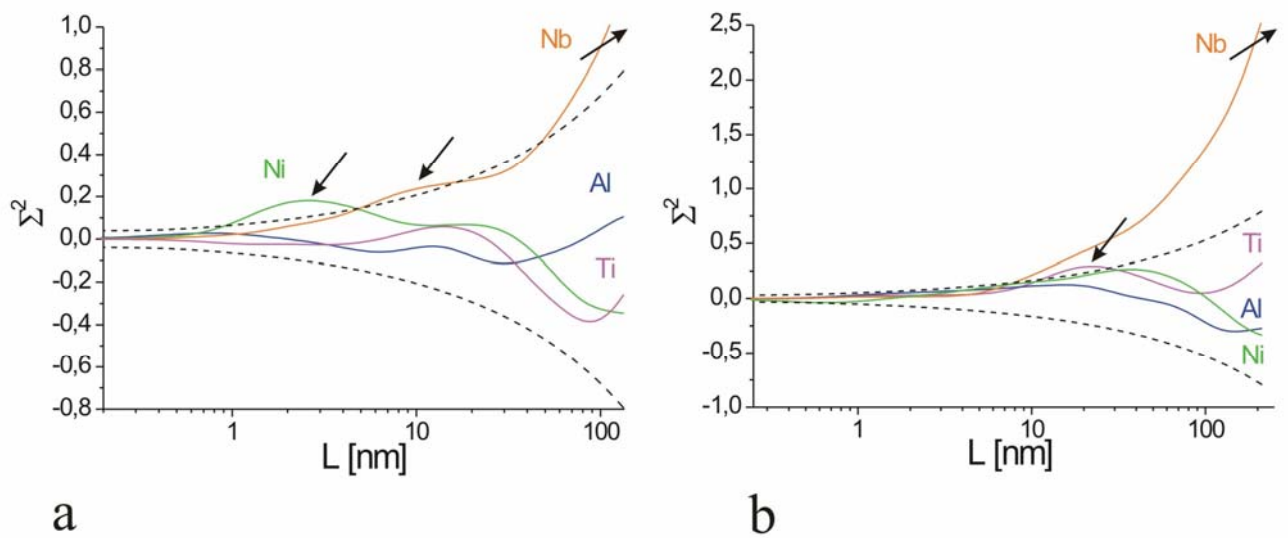


Fig. 3.3. WDF analyses of atom probe data shown (a) in Fig. 3.2a and (b) in Fig. 3.2b. Concentration values are determined in 0.1 nm thick slices with a cross section of $1.5 \times 1.5 \text{ nm}^2$ (see the red boxes in Fig. 3.2).

Qualitative changes happen after the solution treatment at 980°C for 10 h. Ti and especially Nb indicate inhomogeneous distributions whereas Al and Ni lie in the range of statistical oscillations (Fig. 3.3b). The principal wavelength and concentration amplitude of Ti fluctuation are 23 nm and $\Delta C_{Ti} \cong 0.64$ at.% respectively. The principal wavelength of Nb fluctuation is longer than 212 nm, the concentration amplitude amounts to $\Delta C_{Nb} \cong 0.54$ at.% .

Generally several WDF analyses were carried out for each reconstruction presented in Fig. 3.2. For this purpose the red boxes were moved to other positions, remaining parallel to the reconstructed volume. Ni and Nb seem to be heterogeneously distributed after solution treatment at 980°C for 3 h. Ti and Al show heterogeneous distributions only in some cases. Al is homogeneously distributed after solution treatment for 10 h. Al At the same time WDF analyses clearly show that Nb is

heterogeneously distributed in the matrix with a principal wavelength longer than 212 nm. The corresponding concentration amplitude is $\Delta C_{\text{Nb}} (> 212 \text{ nm}) \cong 0.6 \text{ at.}\%$.

3.1.2 Microstructure after direct ageing

Small precipitates about 10 nm long can be seen in the TEM image of Fig. 3.4a, [DFG 2002]. The SEM image in Fig. 3.4b represents the grain-boundary regions of the Inconel 706 alloy after DA heat treatment. The grain-boundary regions are free of η precipitates, as it is clear from the SEM image. The intragranular η precipitates are not observed either.

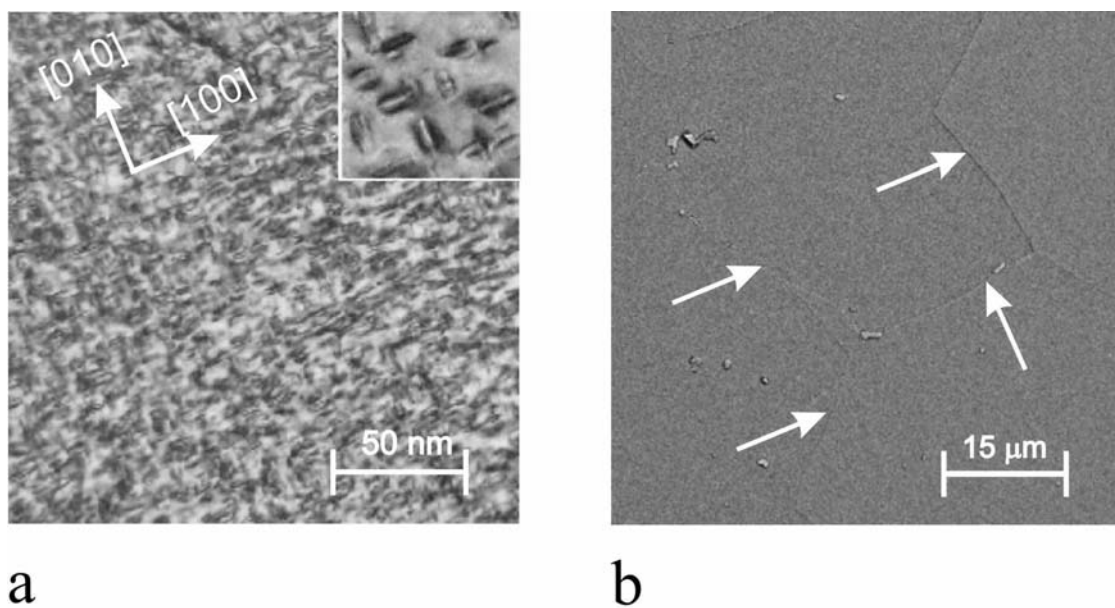


Fig. 3.4. (a) TEM micrograph of fine γ' , γ'' precipitates and γ'/γ'' co-precipitates in Inconel 706 after DA heat treatment. The image in the inset shows non-compact type of co-precipitates. (b) SEM image of the DA sample representing the microstructure at the grain boundaries (indicated by the arrows). They are free of η precipitates.

The detailed precipitate morphology after DA heat treatment can be clarified due to the 3DAP analysis. Fig. 3.5a shows three-dimensional reconstructed positions of Ti and Al atoms in a volume of $8 \times 8 \times 94 \text{ nm}^3$. This volume contains six regions enriched in Ti but only four enriched in Al. Since Al is usually a constituent of the $\text{Ni}_3(\text{AlTi})$ based γ' phase, the four regions enriched in Al (numbers 2 to 5) are identified as γ' phases. The other two regions (numbers 1 and 6) are enriched in Ti and in Nb (not shown here) and are identified as $\text{Ni}_3(\text{TiNb})$ based γ'' phase. However, two precipitates (numbers 2

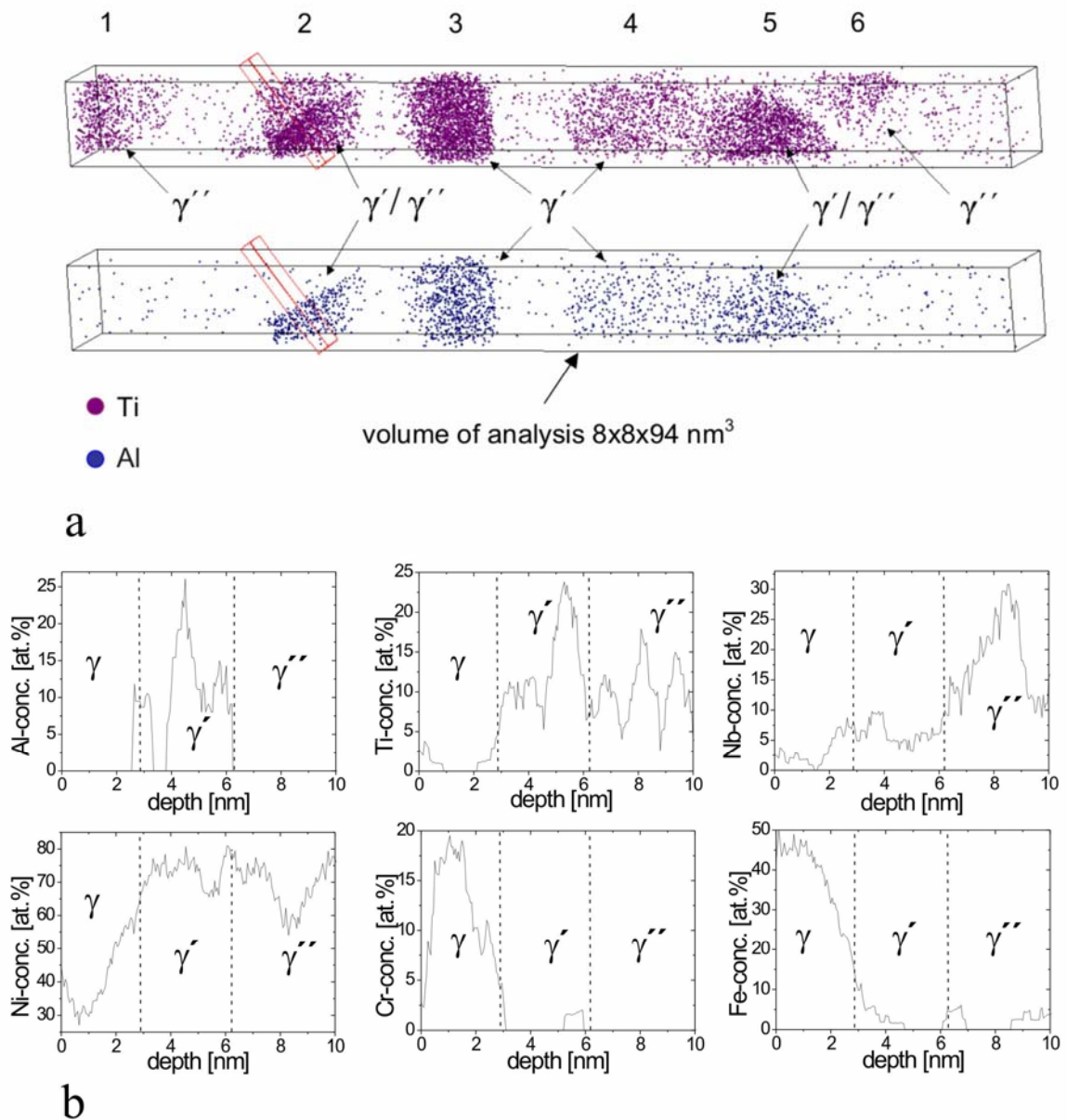


Fig. 3.5. (a) Three-dimensional mapping of Ti (lilac) and Al (blue) after DA heat treatment. The analyzed volume of $8 \times 8 \times 94 \text{ nm}^3$ contains six numbered precipitates. (b) Concentration depth profiles of the primary alloying element across the γ'/γ'' interface in the second co-precipitate (see Fig. 3.5a). The concentration values were determined in 0.7 nm thick slices with a cross section of $1.5 \times 1.5 \text{ nm}^2$ and with a moving step of 0.1 nm .

and 5) contain only partially Al. They were identified as γ'/γ'' co-precipitates. The region depleted both in Ti and Al is the γ matrix. Microchemical information near and across interfaces is obtained from concentration depth profiles. For the co-precipitate number 2 in Fig. 3.5a the concentration depth profiles were taken along a box of $1.5 \times 1.5 \times 10 \text{ nm}^3$ indicated in the analyzed volume. This box was selected such that the γ'/γ'' interface is cut perpendicularly. The corresponding set of depth profiles for the main alloying elements is shown in Fig. 3.5b. The concentration distribution reveals an Al-rich region corresponding to the γ' phase. An enrichment of Nb and Ni of the matrix near the γ/γ' interface was also observed. Cr and Fe seem to be depleted in this region. The phase boundary between γ' and γ'' is very sharp and has a width of about one atomic plane. The concentration distribution of Nb within the γ'' phase is not uniform, a depletion of Nb at both interfaces (to γ' - and to γ -phase) was observed.

Individual γ' and γ'' precipitates were also investigated by atom probe tomography. In order to compare the phase chemistry and the element distribution of individual precipitates, of co-precipitates and of the matrix, the average concentration of each phase is listed in Table 3.1. Significant differences in the γ' and γ'' phases of individual and co-precipitates were observed. In particular, the average concentration of Al is significantly higher in the γ' phase of the co-precipitates than in the γ' phase of the individual precipitates. Ti, in contrast, is much lower in the γ' phase of the co-precipitates. Furthermore, the average composition of the γ'' phase differs mainly by Nb content which is higher in the co-precipitates as compared with the individual precipitates.

A detailed investigation of the individual γ' precipitates shows an enrichment of Nb in the matrix near the γ/γ' interface, as is seen in the concentration depth profile in Fig. 3.6a. Two-dimensional concentration distribution of Nb is represented in Fig. 3.6b as a cross section through the analyzed volume using false colors. Small clusters of Nb with concentrations up to 18 at.% around the γ' precipitate are visible. The interface has a width of about 1 nm. Cr and Fe have negative chemical gradients towards precipitates.

The volume fractions of the matrix f_γ can be estimated by making use of mass conservation. We denote the nominal concentration for a certain element as c_n , the concentration of this element in the matrix, in the γ' and in the γ'' phases as c_γ , $c_{\gamma'}$ and $c_{\gamma''}$, respectively. If we furthermore ignore the small amount of other phases, e.g. that of the η phase (which mostly concentrates at the grain

Table 3.1. Composition of phases (in at.%) in Inconel 706 after DA and after MST heat treatments as measured by three-dimensional atom probing (the symbols have indices corresponding to the nature of phases; for example γ'_{ind} indicates γ' phase as an individual precipitate; γ'_{co} means γ' phase as part of a co-precipitate).

	Ni	Al	Ti	Nb	Cr	Fe
<i>Direct ageing</i>						
γ	36.9 ± 0.3	0.65 ± 0.05	1.1 ± 0.1	1.6 ± 0.1	17.0 ± 0.3	42.7 ± 0.3
γ'_{co}	70.5 ± 1	4.6 ± 0.7	16.5 ± 1	5.2 ± 0.8	0.5 ± 0.3	2.7 ± 0.5
γ''_{co}	69.2 ± 0.7	-	9.7 ± 0.4	18.1 ± 0.7	-	2.1 ± 0.2
γ'_{ind}	69.8 ± 0.7	4.2 ± 0.3	16.3 ± 0.6	5.3 ± 0.3	0.6 ± 0.1	3.2 ± 0.3
γ''_{ind}	70.5 ± 0.9	0.9 ± 0.2	10.0 ± 0.6	15.1 ± 0.7	1.0 ± 0.2	2.6 ± 0.3
<i>Modified stabilization heat treatment</i>						
γ	36.8 ± 0.5	0.47 ± 0.1	1.0 ± 0.1	1.0 ± 0.1	16.1 ± 0.6	44.2 ± 0.7
γ'_{co}	70.2 ± 0.6	3.5 ± 0.3	17.0 ± 0.6	6.1 ± 0.3	0.7 ± 0.1	2.1 ± 0.2
γ''_{co}	69.9 ± 0.7	-	7.0 ± 0.3	20.6 ± 0.7	0.7 ± 0.1	1.8 ± 0.2
γ'_{ind}	70.1 ± 0.6	5.1 ± 0.4	17.2 ± 0.5	3.8 ± 0.3	0.4 ± 0.1	3.1 ± 0.3

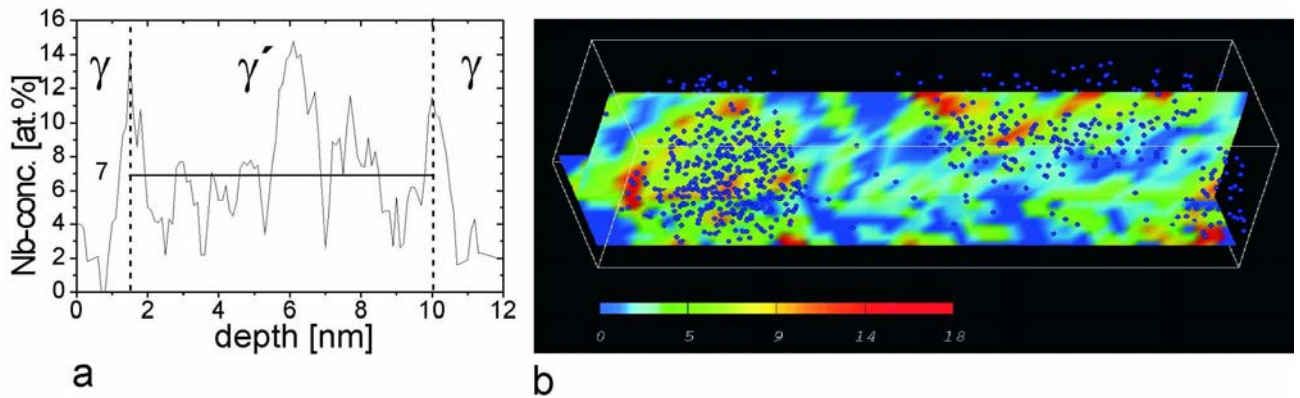


Fig. 3.6. (a) Concentration depth profile of Nb across a γ' precipitate. (b) Two-dimensional concentration map of Nb. Color change from blue to red indicates an increase in the concentration of Nb. The blue circles show the three-dimensional reconstruction of Al.

boundaries), then the relation

$$\frac{c_n - c_{\gamma''}}{c_{\gamma'} - c_{\gamma''}} = f_{\gamma'} \cdot \frac{c_{\gamma} - c_{\gamma''}}{c_{\gamma'} - c_{\gamma''}} + f_{\gamma'}, \quad (3.1)$$

holds, where $f_{\gamma'}$ is the molar fraction of the γ' phase in the alloy. We suppose that the quantities of γ' (and of γ'') phase are equally distributed between the individual and co-precipitates. In general equation (3.1) can be evaluated for each element using the lever rule diagram [Blavette 1986]. In our case, however, only Cr, Ni and Fe are significant as matrix elements and the denominators in equation (3.1) are close to zero. Therefore, we can simplify (3.1) to

$$f_{\gamma} = \frac{c_n - c_{\gamma''}}{c_{\gamma} - c_{\gamma''}}. \quad (3.2)$$

Using the data of Table 3.1, we get $f_{\gamma} = 87 \pm 4 \%$ for the DA heat treatment.

3.1.3 Microstructure after modified stabilization heat treatment

A bimodal precipitate distribution, consisting of fine γ'/γ'' co-precipitates and larger γ'' needles aligned along the $\langle 001 \rangle$ direction is observed in the MST specimens (Fig. 3.7a, [DFG 2002]). The large needles are γ'' phases, as can be seen from the diffraction patterns. The fine co-precipitates in the MST condition are small in size, between 15 – 20 nm, and are predominantly of the non-compact type. The needle-like γ'' precipitates after MST heat treatment are 100 nm long and 10 nm wide.

Platelike η phase (Fig. 3.7b) within the grains is also occasionally observed in MST specimens (see also [Mukherji 2003]). The SEM image also shows serrated η plates at the grain boundaries in the MST samples.

The morphology of precipitates in the MST specimens is shown also in Fig. 3.8 which is a high angle annular dark field STEM (HAADF-STEM) micrograph. The variation of the contrast within the precipitates indicates different chemical composition. Bright contrast results from Nb, which is a constituent element of the γ'' Ni_3Nb -based phase. With regard to the contrast the precipitates indicated by 1, 2 and 3 in the figure are identified as γ'/γ'' co-precipitates. The other (4, 5) are individual γ'' precipitates. The precipitate number 6 is a $\gamma'/\gamma''/\gamma'$ “sandwich”, consisting of three slices.

A high resolution TEM image of a small co-precipitate embedded in the matrix is shown in Fig. 3.9. The diffraction pattern of the [001] zone from the precipitate shown in the inset of the figure identifies this precipitate as a γ'/γ'' co-precipitate. This co-precipitate consists of two parts, the left

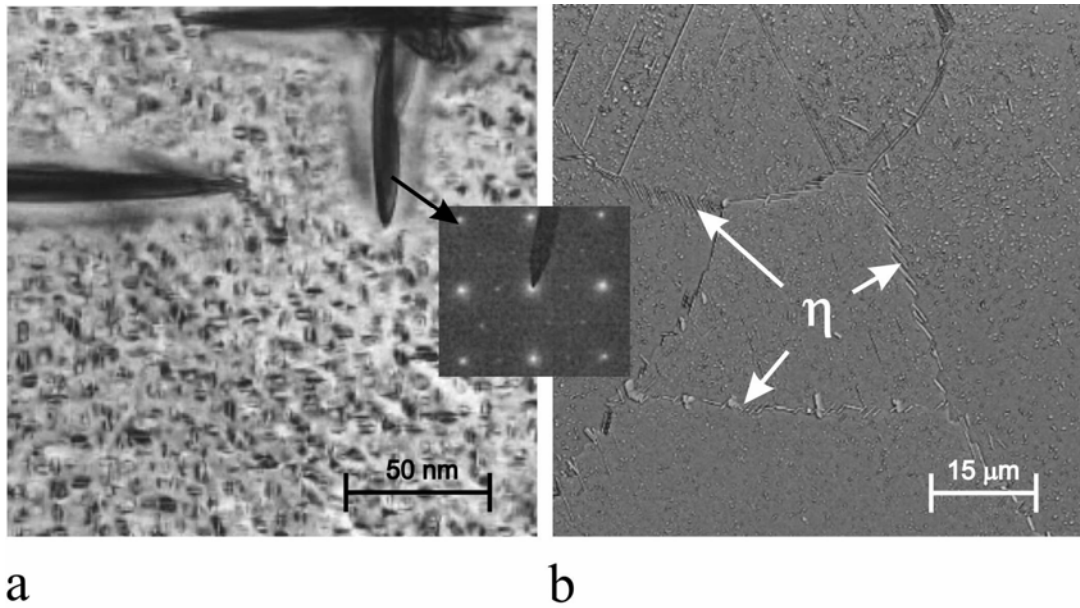


Fig. 3.7. (a) TEM micrograph of small (the size is between 15 and 20 nm) γ' , γ'' precipitates and γ'/γ'' co-precipitates in Inconel 706 after a heat treatment under the MST conditions. Larger needlelike precipitates are observed in addition to above mentioned small precipitates. SAED from the needle in the image clearly identifies it as a γ'' precipitate. (b) SEM image of the MST sample shows η plates at the grain boundaries (indicated by the arrows).

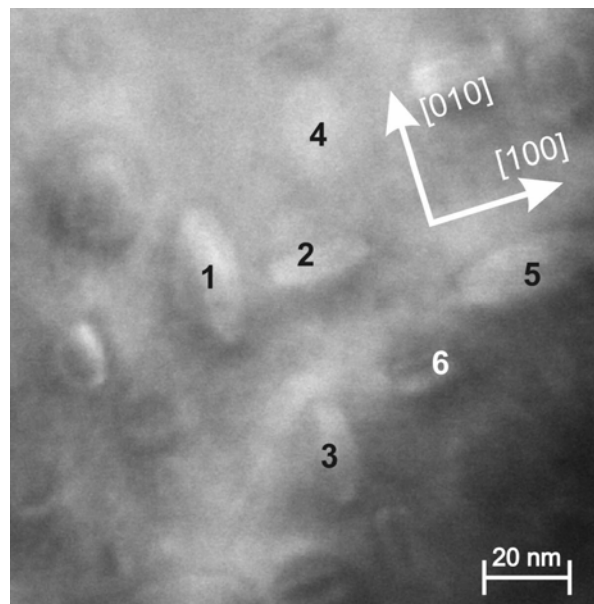


Fig. 3.8. HAADF-STEM image of small oval individual and co-precipitates. Bright contrast results from Nb which is a constituent element of the γ'' Ni_3Nb -based phase. Therefore, the precipitates 1, 2 and 3 are identified as γ'/γ'' co-precipitates; 4 and 5 are individual γ'' precipitates and the sixth precipitate is a $\gamma'/\gamma''/\gamma'$ “sandwich”, consisting of three slices.

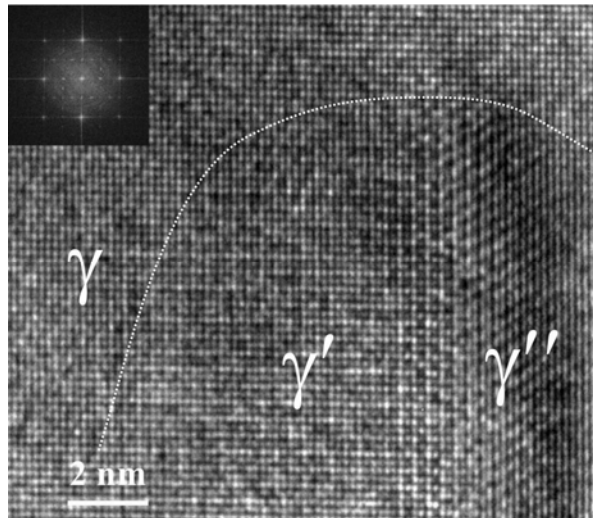


Fig. 3.9. HRTEM micrograph of a γ'/γ'' precipitate embedded in the matrix of the MST sample. The Fourier-transform of the HRTEM image is shown at the upper left. The dashed line shows the interface between the matrix and the co-precipitate. The left part of the co-precipitate corresponds to the γ' phase and the right to the γ'' phase, being semi-coherent with the matrix.

part (γ' phase) of the precipitate is coherent to the matrix and the right part (γ'' phase) is semi-coherent to the matrix and the γ' phase.

Fig. 3.10a shows the reconstruction of Ti, Nb and Al atom positions in Inconel 706 after MST heat treatment in a volume of $8 \times 8 \times 23 \text{ nm}^3$. Two regions enriched in Ti, Nb and Al are visible which correspond to the two different types of precipitates in the investigated volume. One of them is an individual γ' precipitate and the other one is a $\gamma''/\gamma'/\gamma''$ co-precipitate. This fine co-precipitate is of the non-compact morphology with a core of γ' being coated with γ'' phases on its top and bottom. Atomic layers of the γ' precipitate are visible in Fig. 3.10a, and by suitable rotation of the $\gamma''/\gamma'/\gamma''$ co-precipitate also in Fig. 3.10b. The length scale of the measured volume is calibrated by the lattice spacing. As shown in Fig. 3.10b, the atomic planes remain parallel while crossing the γ'/γ'' boundaries. This signifies that the γ' and γ'' phases are coherent in cross direction of the co-precipitate. The coherency between γ , γ' and γ'' is maintained as schematically illustrated in Fig. 3.10c. The presumable positional relationship of the unit cell inside the “sandwich” is schematically shown in this figure. By assuming this structure, we expect coherency of (001) atomic planes at the both interfaces γ''/γ' and γ'/γ'' in the co-precipitate.

The microchemical information about the $\gamma''/\gamma'/\gamma''$ co-precipitate is obtained from concentration depth profiles taken along a square rod which was aligned approximately perpendicular to the γ'/γ''

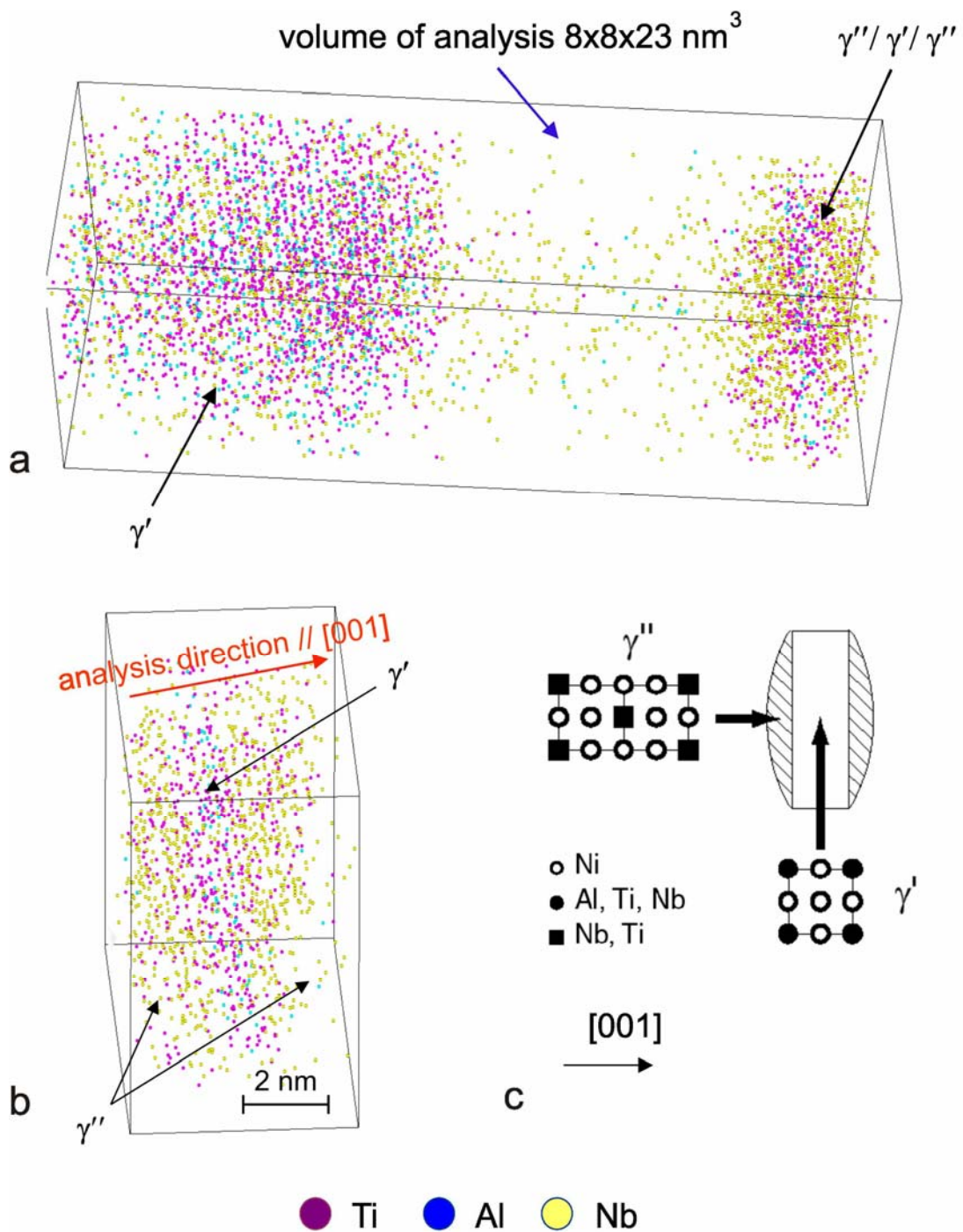


Fig. 3.10. (a) Three-dimensional mapping of Ti (lilac), Al (blue) and Nb (yellow) after MST heat treatment. (b) Two precipitates are visible. The precise structure of the $\gamma''/\gamma'/\gamma'''$ co-precipitate and (c) the corresponding outline sketch are exhibited as well. The analyzed volume is 8x8x23 nm³.

interface. The composition depth profiles taken with a cross section of $3 \times 3 \text{ nm}^2$ are shown in Fig. 3.11. The concentration values were calculated for slices of 0.5 nm thickness with a measuring step of 0.05 nm. The depth profiles reveal that the transition from the Al-enriched γ' phase to Al-depleted γ'' phase occurs over one atomic plane. The concentration distribution of elements (see Fig. 3.11) within the precipitate and near the interfaces is similar to that observed in the sample after DA heat treatment. In particular Ti is depleted towards the matrix, and Nb becomes saturated in the γ' phase close to the γ'/γ'' interfaces. It is noted that the composition profiles were taken perpendicular to the internal γ''/γ' and γ'/γ'' interfaces but not perpendicular to the γ''/γ interface. Therefore, the phase boundary between γ'' and γ phases is narrower than 1 nm. The compositions of each phase after MST heat treatment is listed in Table 3.1. Comparing these data, it is interesting to note that the composition of the γ' phase whether in the individual precipitate or in the co-precipitate is nearly equal, and it is comparable to the composition of the individual precipitates produced after DA heat treatment.

Using the data of Table 3.1 and equation (3.2), we get $f_\gamma = 86 \pm 3 \%$ for the MST heat treatment.

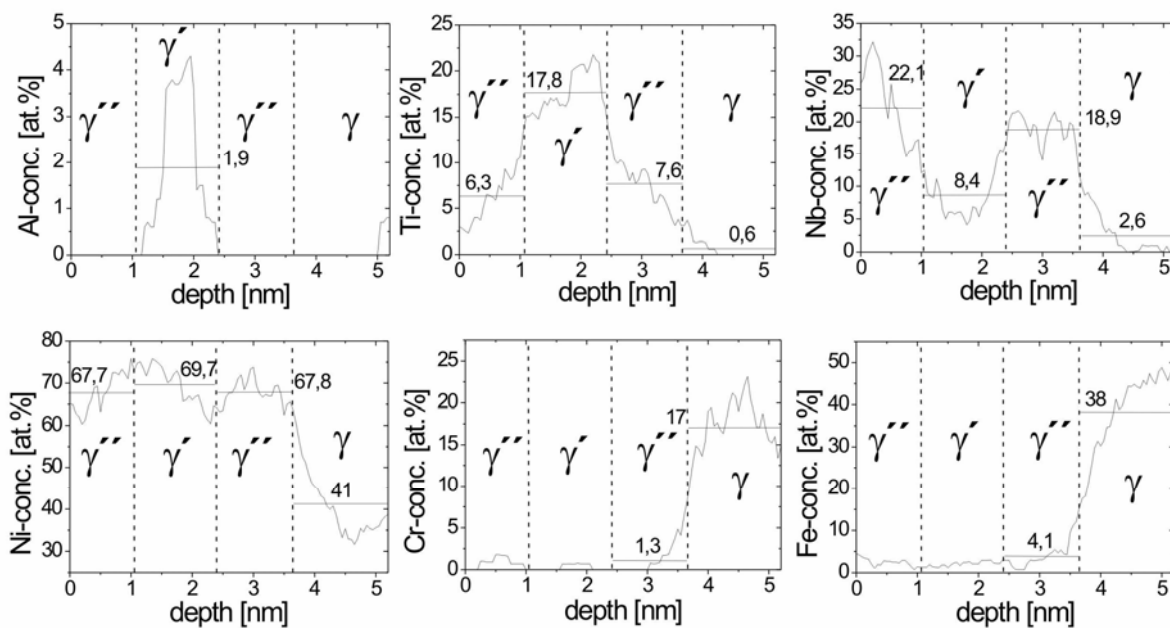


Fig. 3.11. Depth profiles of the primary alloy element across the co-precipitate (see Fig. 3.10b). The concentration values were determined in 0.5 nm thick slices with a cross section of $3 \times 3 \text{ nm}^2$ and with a moving step of 0.05 nm.

3.1.4 Microstructure after modified stabilization heat treatment and after ageing at 750°C for 750 h

A bright-field TEM image of the microstructure of the MST sample after ageing at 750°C for 750 h is shown in Fig. 3.12a [DFG 2002]. The γ' phase grows and form cubic precipitates with sizes around 60 nm, whereas the γ'' phase are discs, which are approximately 300 nm in diameter. There are also some γ' cubes arranged directly at the γ'' plates. An important observation is that nucleation and growth of η plates takes place during ageing. An η plate is well discernible in the TEM micrograph. It differs from the γ'' plates by a differing orientation. The size of η plates can be estimated from the SEM image in Fig. 3.12b as 5 – 8 μm on the average. However some η plates can be a few tens of micrometers large.

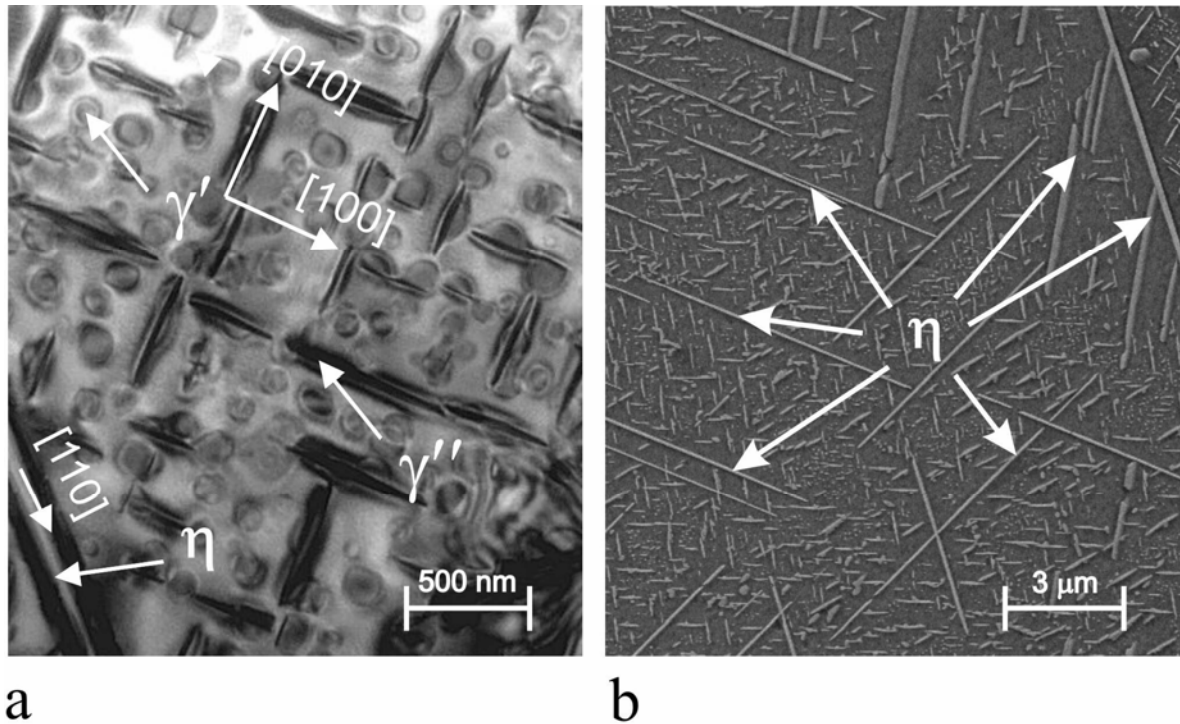


Fig. 3.12. (a) TEM micrograph of fine γ' , γ'' precipitates and γ'/γ'' co-precipitates in Inconel 706 after a heat treatment under MST conditions and after ageing at 750°C for 750 h. (b) SEM image of the MST750 sample representing the microstructure at the grain boundaries (indicated by the arrows). They are free of η precipitates.

Fig. 3.13a shows the reconstruction of Ti and Fe atom positions in a volume of 6.4x6.4x32 nm³. The Ti-enriched region contains hardly any Al (see Table 3.2, row $\gamma''_{3\text{DAP}}$). Therefore, it corresponds to the γ'' phase. The remaining region, depleted in both Ti and Al and enriched in Fe is the γ matrix (see the composition in Table 3.2, row $\gamma_{3\text{DAP}}$). The micro-chemical information across the interface is

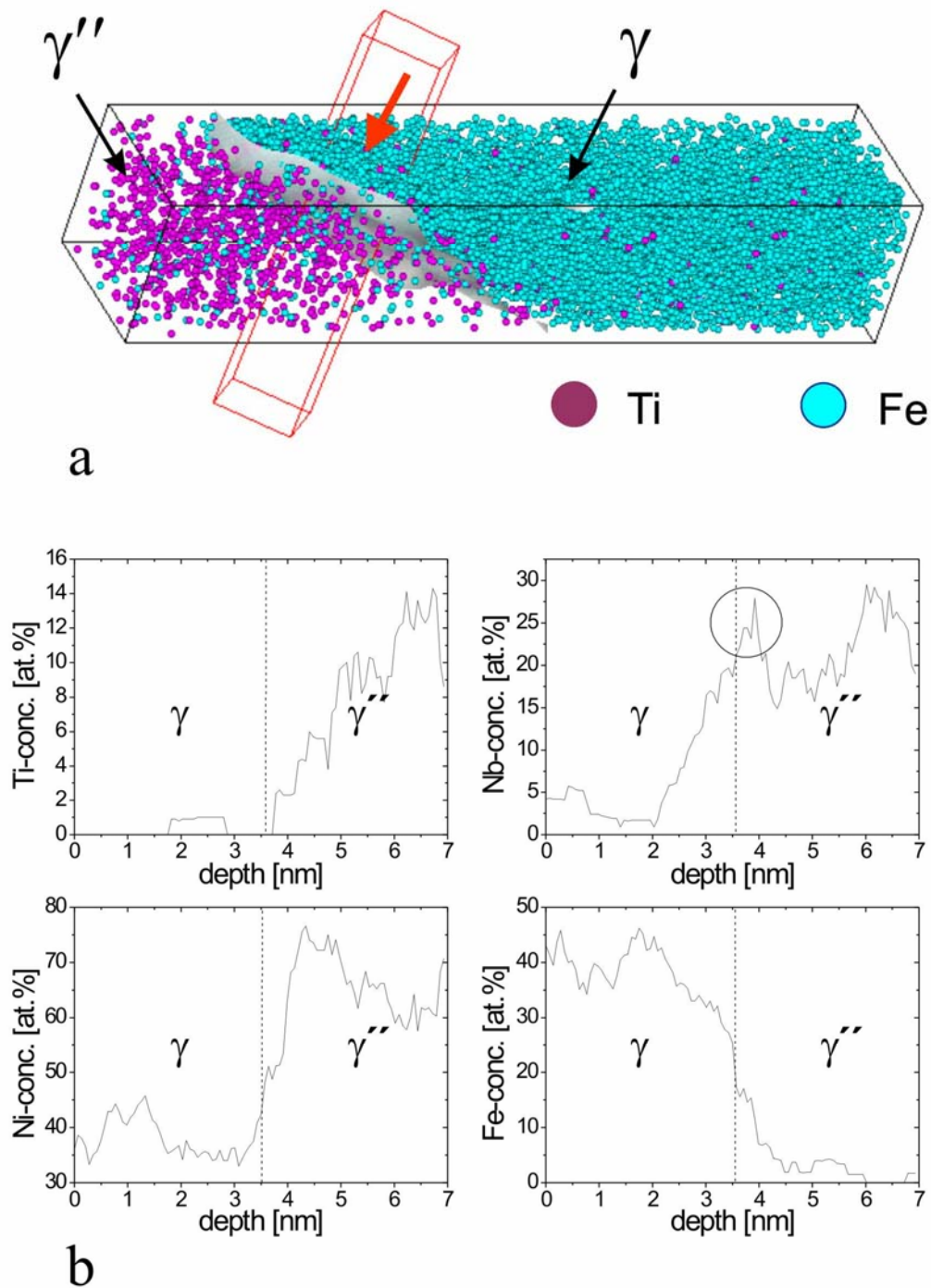


Fig. 3.13. (a) Three-dimensional mapping of Ti (lilac) and Fe (blue) in the MST750 sample. The analyzed volume of $6.4 \times 6.4 \times 32 \text{ nm}^3$ contains a γ'' precipitate. (b) Concentration depth profiles of the primary alloy element across the γ/γ'' interface (see Fig. 3.13a). The concentration values were determined in 0.7 nm thick slices with a cross section of $1.5 \times 1.5 \text{ nm}^2$ and with a moving step of 0.07 nm.

obtained from the concentration depth profiles which were taken along a box of $1.5 \times 1.5 \times 7 \text{ nm}^3$, as indicated in the analyzed volume. This box is oriented perpendicular to the γ''/γ interface. The corresponding set of depth profiles for the main alloying elements is shown in Fig. 3. 13b. The profile for Al is not shown because this element is practically lacking in both phases γ and γ'' . The profile for Cr is similar to that of Fe. Therefore, the Cr-profile is not given either. The dashed lines indicate the γ''/γ interfaces. The transition from the Nb/Ti/Fe enriched region to the Nb/Ti/Fe depleted one occurs within 2 nm. The transition region for Ni is narrower, about 1 nm. Let us mention the strong negative gradient of Ti-concentration within the precipitate towards the γ''/γ interfaces. This causes Ti-depletion in the vicinity of the interface. On the contrary, the region close to the interface is strongly enriched with Nb, which evidently replaces Ti.

Table 3.2. Chemical composition of phases (in at.%) as measured by the 3DAP and EDX in Inconel 706 after ageing at 750°C for 750 h.

	Ni	Al	Ti	Nb	Cr	Fe
$\gamma_{3\text{DAP}}$	36.3 ± 0.5	0.47 ± 0.08	0.75 ± 0.1	1.2 ± 0.1	20.1 ± 0.4	41.1 ± 0.5
γ_{EDX}	36 ± 1	1.3 ± 0.6	0.9 ± 0.3	1.5 ± 0.6	19.0 ± 0.7	41.4 ± 0.3
$\gamma'_{3\text{DAP}}$	70.4 ± 1	3.42 ± 0.5	19.7 ± 1	3.67 ± 0.5	0.05 ± 0.05	2.85 ± 0.4
$\gamma''_{3\text{DAP}}$	71.9 ± 2	0.2 ± 0.2	8.5 ± 1	16.8 ± 1	0.8 ± 0.4	1.8 ± 0.6
γ''_{EDX}	70.4 ± 1.2	0.3 ± 0.7	7.8 ± 0.5	10.9 ± 0.6	3.2 ± 0.5	7.3 ± 0.3
η_{EDX}	71.2 ± 2	1.6 ± 1	12.9 ± 0.3	6.0 ± 0.2	1.9 ± 0.5	6.4 ± 0.8

An internal part of a γ' precipitate was also measured in the 3DAP. The corresponding composition of the precipitate is listed in Table 3.2, see row $\gamma'_{3\text{DAP}}$. The composition of η plates was measured by means of EDX analysis (row η_{EDX}). Additionally the compositions of γ'' plates and of the γ matrix, as measured by the EDX analysis are given (rows γ''_{EDX} and γ_{EDX}). EDX measurements of the composition of the γ matrix are in good agreement with analogous measurement using the 3DAP. However these two methods yield different compositions for the γ'' phase, especially concerning the content of Nb as well as of Cr and Fe. EDX yields about 6 at.% lower content of Nb and instead higher content of Fe and Cr in the γ'' phase, as compared to the measurements by 3DAP. The EDX method is less exact compared to 3DAP, because the composition of a precipitate measured by the EDX method is an average composition of the region containing the precipitate and the surrounding matrix. Therefore, in the γ'' phase more matrix-formers Fe and Cr are present as

measured by EDX. Consequently, the composition of the η phase (as measured by EDX, Table 3.2) should be also interpreted accounting for the remarks concerning the content of Nb, Fe and Cr.

Since the alloy structure after MST750/IN is more complicated as compared with that after MST/IN or MST/DA, it is difficult to apply the level rule diagram approach in order to reveal the volume fractions of the phases after MST750/IN.

3.1.5 Microstructure after modified stabilization heat treatment and after ageing at 750°C for 5000 h

A bright-field TEM image of the alloy microstructure after MST5000/IN heat treatment is shown in Fig. 3.14a. There are no small precipitates or co-precipitates visible, instead large traces of η precipitates, which are a few micrometers long. These traces lie along the $\langle 110 \rangle$ direction in the [001] oriented foil. The real shape of the η precipitates can be found from the SEM image of a FIM tip. Fig. 3.14b shows several η plates intersecting the tip. The thickness of the plates is smaller than 200 nm. The tip imaged in Fig. 3.14b is not suitable for further measurements using 3DAP. Focused ion beam (FIB) milling is necessary to make it suitable for 3DAP measurements. When an η plate lies approximately parallel to the tip axis after electropolishing, as shown in Fig. 3.15, then the sample can be investigated by the 3DAP. The complexity of the sample preparation is due to preferential matrix polishing as compared to the η phase. The chemical compositions of the η phase and of the matrix are listed in Table 3.3.

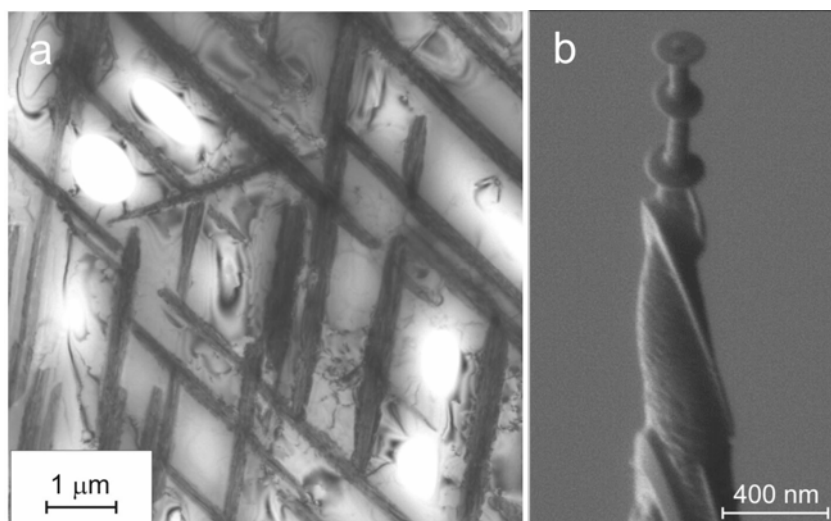


Fig. 3.14. (a) Bright field TEM image of the Inconel 706 alloy after ageing at 750°C for 5000 h. Traces of η plates are visible. (b) SEM image of a tip reveals six η plates crossing through the matrix.



Fig. 3.15. BF TEM image of a tip suitable for a 3DAP experiment (Inconel 706 alloy aged at 750°C for 5000 h).

Table 3.3. Chemical composition of phases (in at.%) in Inconel 706 after ageing at 750°C for 5000 h as measured by the 3DAP.

	Ni	Al	Ti	Nb	Cr	Fe
γ	40.3 ± 0.2	0.49 ± 0.03	0.31 ± 0.02	0.90 ± 0.04	16.8 ± 0.2	41.2 ± 0.2
η	68 ± 2	1.2 ± 0.5	13.9 ± 1.5	12.5 ± 1.4	0.1 ± 0.1	4.4 ± 0.9

One can derive the equation similar to (3.1), in order to determine the volume fraction f_η of the η phase and $f_\gamma = 1 - f_\eta$ of the matrix. Let us denote the nominal concentration for a certain element c_n , the concentration of this element in the γ matrix c_γ and in the η phases c_η . Thus we obtain the following relation between the concentrations,

$$\frac{c_n}{c_\eta} = f_\gamma \cdot \frac{c_\gamma - c_\eta}{c_\eta} + 1. \quad (3.3)$$

Evaluating equation (3.3) for each element using the data given in Table 3.3 one obtains the volume fractions f_γ of the γ matrix, namely $f_\gamma = 93 \pm 2 \%$.

3.2 Re-containing Inconel 706 superalloy

3.2.1 Microstructure after modified stabilization heat treatment

Fig. 3.16a shows a bright field TEM micrograph and corresponding specific area electron diffraction patterns of the Re-containing Inconel 706 alloy after modified stabilization heat treatment. Small precipitates of coffee-bean-like morphology are elongated along the $\langle 001 \rangle_\gamma$ directions. The length of these precipitates is approximately 15 – 20 nm. The diffraction pattern clearly displays superlattice reflections from γ' and γ'' phases. Stabilization heat treatment produces long plate-like η precipitates that are formed mainly on grain boundaries, occasionally in the grain interior (see Fig. 3.16b [DFG 2002]). These precipitates are semi-coherent with the γ matrix in accordance with observations by Shibata, 1996.

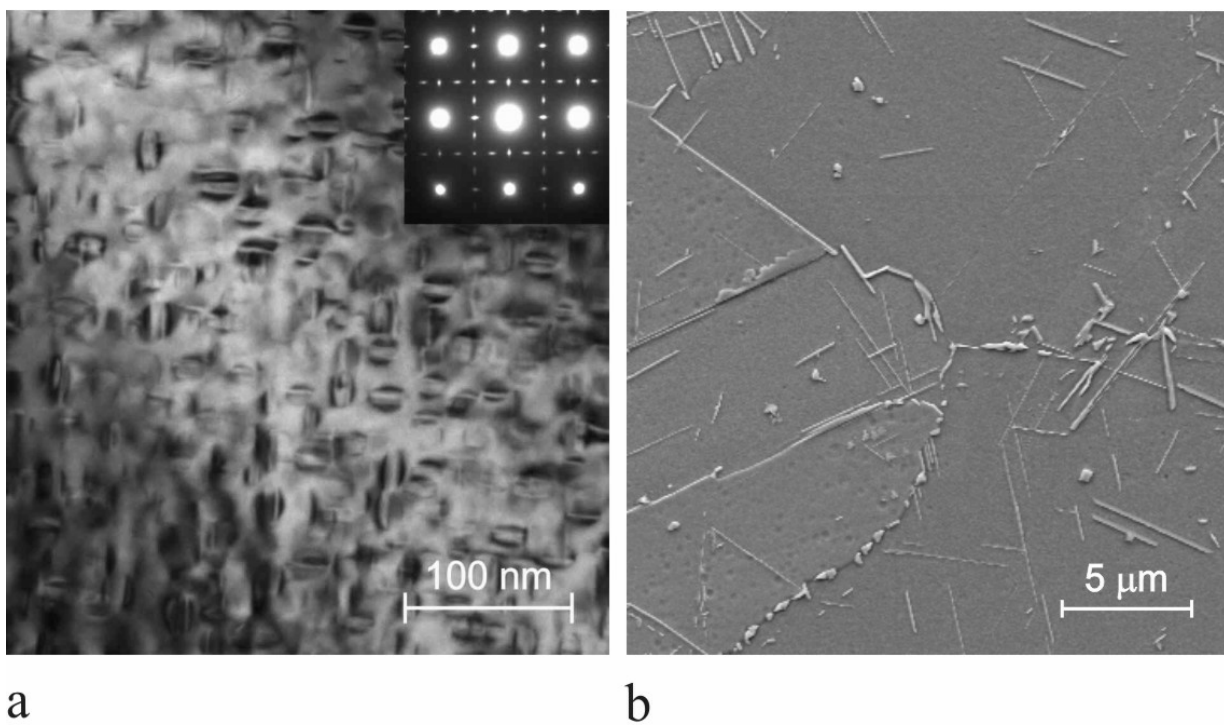


Fig. 3.16. The microstructure of Re-containing Inconel 706 alloy after the MST heat treatment: (a) bright field TEM image of fine γ' , γ'' and γ'/γ'' precipitates. A $[001]_\gamma$ zone axis diffraction pattern is represented in the inset; (b) SEM image with typical plate-like η precipitates at the grain-boundaries formed after MST heat treatment.

Unfortunately the TEM micrograph in Fig. 3.16a does not give the complete information about the morphology of the precipitates since one sees mainly the distribution of stress contrast in the

microstructure. Therefore, measurements with high spatial resolution are carried out by means of the 3DAP. Fig. 3.17 displays the 3D reconstructions of Ti (red) and Al (cyan) atom positions in a volume of $14 \times 14 \times 235 \text{ nm}^3$. This volume consists of a number of regions enriched in Ti and/or in Al. Since Al is a constituent of the $\text{Ni}_3(\text{AlTi})$ based γ' phase, the regions enriched in Al are identified as γ' phases, whereas the regions enriched only in Ti are identified as $\text{Ni}_3(\text{TiNb})$ based γ'' phase. The advantage of the 3DAP measurements is that this approach allows us to identify the morphology of any precipitate reconstructed in Fig. 3.17. The morphology of these precipitates is investigated in connection with the distribution of elements at the phase boundaries. Microchemical information is obtained from concentration depth profiles. With this purpose, every precipitate or co-precipitate in Fig. 3.17 was analyzed in detail and depth profiles are built along boxes aligned perpendicular to the interface of the interest.

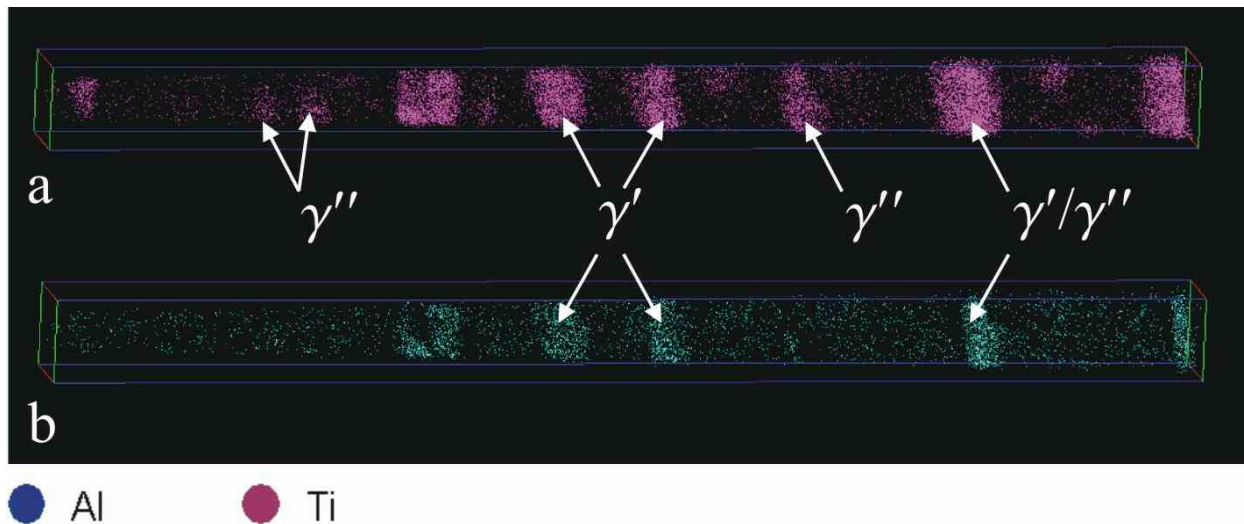


Fig. 3.17. Three-dimensional reconstruction of (a) Ti (lilac) and (b) Al (cyan) atom positions in a Re-containing Inconel 706 alloy after modified stabilization heat-treatment. The type of some precipitates is explained. The reconstructed volume is $14 \times 14 \times 235 \text{ nm}^3$.

Parts of two γ'/γ'' co-precipitates from Fig. 3.17 are represented in Fig. 3.18. They both have a well developed γ'' phase which is predominant as compared with γ' . The co-precipitate in Fig. 3.18b looks like a plate-like γ'' precipitated with an attached hemisphere of γ' phase. The γ'' phase in Fig 3.18a is not yet so strongly developed. Depth profiles are taken along the indicated red boxes, oriented perpendicular to internal γ'/γ'' interfaces, as shown in the images. These profiles are summarized in Fig. 3.19. They reveal Al-enriched regions corresponding to the γ' phase and Nb-enriched regions corresponding to γ'' . Significant variations of concentrations of Ni, Nb and Ti are

visible within the co-precipitates. An important observation is the increase of Ni content of about 10 at.% within the co-precipitate close to γ/γ' and γ/γ'' external interfaces (see both Fig. 3.19a and Fig. 3.19b). Ni has a smaller atomic radius than Nb and Ti. Therefore, Ni-enriched regions within co-precipitates are expected to experience compressive stresses. In other words, the diffusion of Nb and Ti atoms through Ni-enriched regions is difficult, i.e. through those areas of external interfaces which are oriented parallel to the internal γ'/γ'' boundary (or perpendicular to the $[001]_{\gamma''}$ direction). Since Nb and Ti are precipitate formers further coarsening of co-precipitates in Fig. 3.18 seems to be advantageous perpendicular to the $[001]_{\gamma''}$ direction, i.e. parallel to the γ'/γ'' boundary. This conclusion is in agreement with the morphology of the co-precipitates being observed in Fig. 3.18.

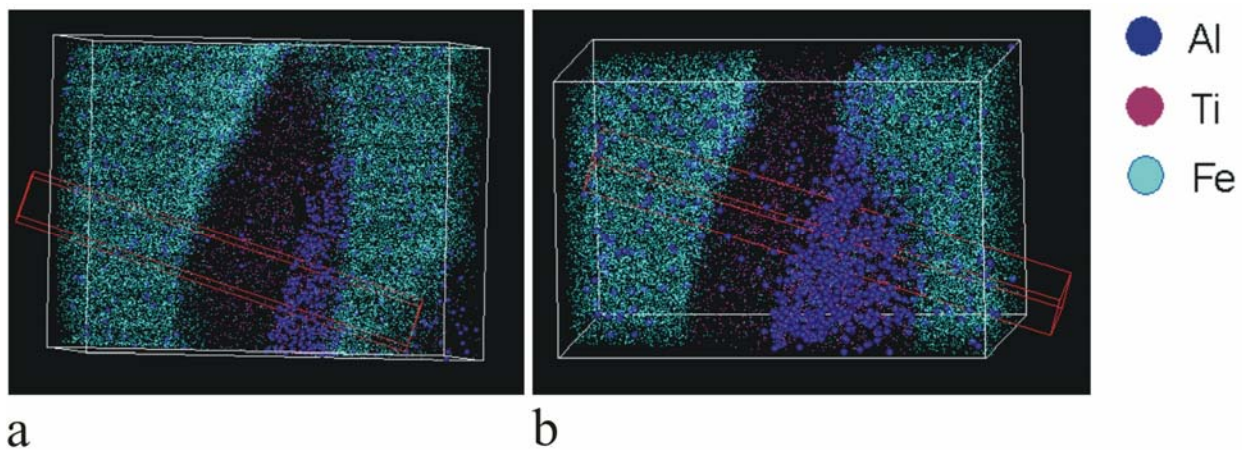
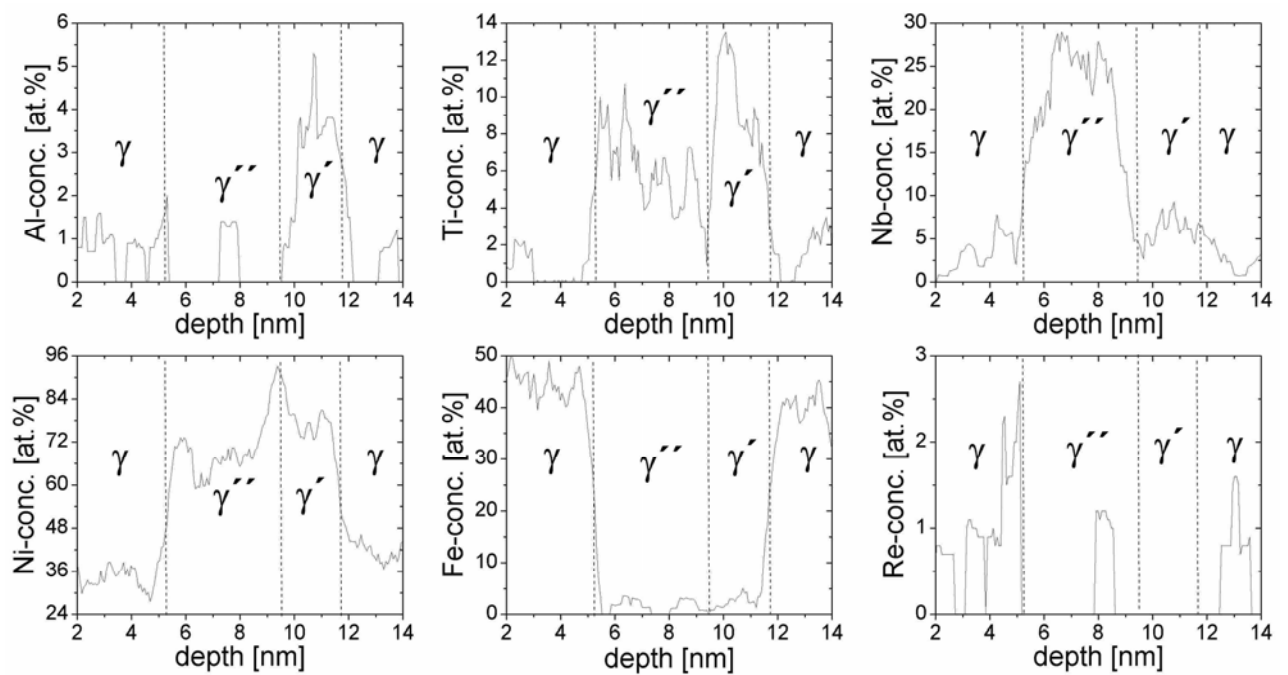


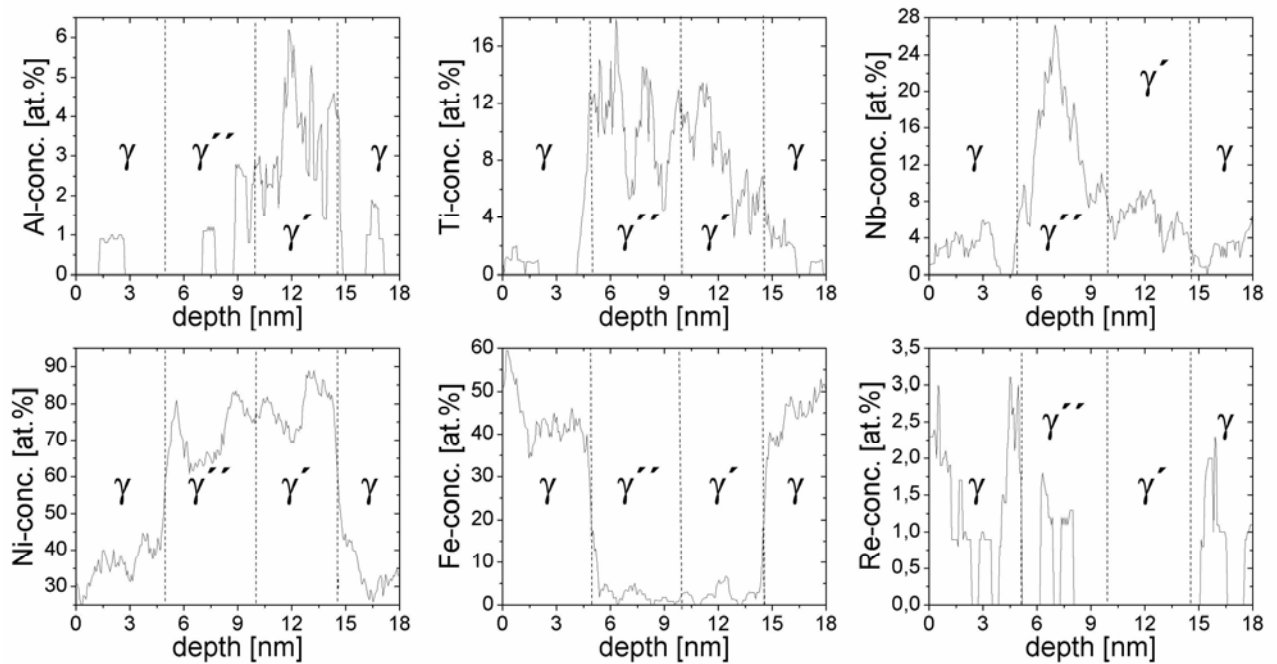
Fig. 3.18. Three-dimensional reconstruction of Ti (lilac), Al (dark blue) and Fe (blue) atom positions in the investigated volumes (a) $12 \times 12 \times 18.4 \text{ nm}^3$ and (b) $13 \times 13 \times 16.5 \text{ nm}^3$. Two co-precipitates with mainly developed γ'' phase are shown. The enrichment of Fe atoms corresponds to the matrix. Red boxes are oriented perpendicular to the γ'/γ'' interface.

The vicinity of the γ'/γ'' interface also experiences some compression (see Ni distributions in Fig. 3.19). Nb and Ti are depleted at internal interfaces. However, Ti depletion at the internal interface is not evident for the co-precipitate shown in Fig. 3.18a. Here a replacement of Ni by Ti by about 5 at.% takes place. Based on the behavior of primary elements at the internal interfaces, one can conclude that they prevent diffusion of Ti and Nb between parts of the co-precipitates. Apparently γ' and γ'' phases of the co-precipitates growth independently of one another.

The precipitate shown in Fig. 3.20a looks like a single γ'' precipitate. However, one sees an enrichment of Al atoms (blue) on the left side of the precipitate. The respective region is represented as a hatched area in the depth profiles and is about 1 nm wide, see Fig. 3.20b. It is clear from the



a



b

Fig. 3.19. Depth profiles of the primary alloy elements (a) across the co-precipitate in Fig. 3.18a; (b) across the co-precipitate in Fig. 3.18b. Concentration values are determined in 0.7 nm thick slices with a cross section of $2 \times 2 \text{ nm}^2$. The profiles are built with a moving step of 0.07 nm from left to right, see Fig. 3.18.

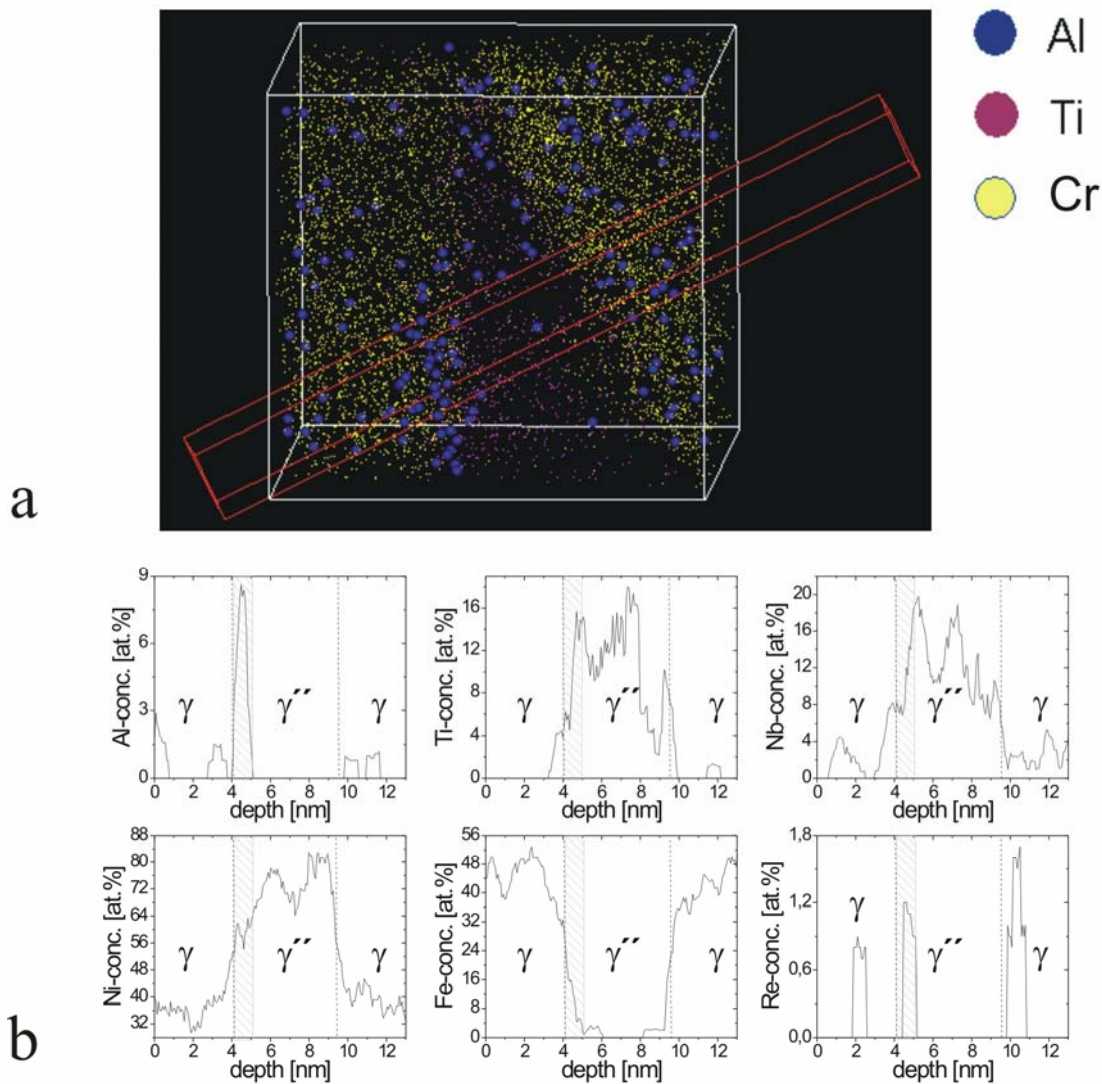


Fig. 3.20. (a) Three-dimensional reconstruction of spatial arrangement of Ti (lilac), Al (dark blue) and Cr (yellow) atoms in a volume of $11 \times 11 \times 12 \text{ nm}^3$. (b) Depth profiles of the primary alloy elements across the co-precipitate in Fig. 3.20a. The hatched area corresponds to the Al-enriched region. Concentration values are determined in 0.7 nm thick slices with a cross section of $2 \times 2 \text{ nm}^2$. The profiles are built with a moving step of 0.07 nm from left to right, see Fig. 3.20a.

profiles that the region enriched in Al lies within the transition region γ/γ'' and closer to the precipitate. Al enrichment is concerned with the Ti and Nb enrichments as well, which are necessary for creating the γ' phase. Therefore, this region can indeed be the γ' phase. Consequently, part of the reconstructed precipitate should be a part of a γ'/γ'' co-precipitate. Another possibility could be that γ' phase nucleates heterogeneously. At the same time Ni experiences some depletion in the Al-enriched region, indicating probably some stress relaxation around the γ/γ'' interface. Ni enrichment

takes place within the precipitate close to the opposite γ/γ'' interface (see the Ni distribution in Fig. 3.20b). This agrees with the examined co-precipitates, reconstructed in Fig. 3.18. The concentration distribution of Ni varies significantly with an amplitude of about 6 at.%, anti-correlating in general with Ti and Nb concentration variations. The depth profiles in Fig. 3.20b are constructed perpendicular to that γ/γ'' interface, which is completely depleted in aluminum. Therefore, according to these depth profiles one concludes, that the γ/γ'' interface has a width of about 1 nm.

Another group of co-precipitates exhibit a predominant γ' phase as a predominant one. They are summarized in Fig. 3.21 and Fig. 3.22. This case is especially interesting because γ' particles are potential nucleation sites for the γ'' phase [Cozar 1973]. The depth profiles shown in Fig. 3.21b are in good agreement with the assumption made before. Firstly, the internal γ'/γ'' interface of the co-precipitate indicates an enrichment of Nb on the side of the γ' phase which is the key element for the formation of the γ'' phase. Secondly, the internal interface is not exposed to compressive stress, unlike the concentration distribution of Ni. On the contrary, Ni is replaced by roughly 8 at.% Nb in the region surrounding the γ'/γ'' interface as indicated in the profiles. The Ni enrichment within the co-precipitate close to γ/γ' and γ/γ'' interfaces should be mentioned, in analogy with the above analyzed co-precipitates. The transition zone from Nb-depleted to Nb-enriched region around the γ'/γ'' interface has a range of about 1.5 nm. However the transition region for Al and Ti is narrower and occurs over a range of 0.5 – 1 nm, indicating the width of the internal interface.

Fig. 3.22a shows two precipitates which are placed close to one another. The heterogeneous distribution of Al indicates that the precipitate on the left is a γ'/γ'' co-precipitate. This conclusion is also confirmed by the depth profiles presented in Fig. 3.22c. Al- and Nb-enriched regions are easy to identify here and correspond to γ' and γ'' phases, respectively. The precipitate on the right in Fig. 3.22a looks like a γ' precipitate. However the morphology of this precipitate can be better examined after a small rotation of the entire analyzed volume, as shown in Fig. 3.22b. One sees that the γ' precipitate is coated with a shell of γ'' phase. The concentration of Fe amounts to 30 at.% within the matrix gap between the precipitates, whereas the concentration of Fe in the matrix is 38.2 at.% on the average. This means that Fe is removed from the gap between the precipitates being replaced mostly by Ni atoms. Presumably the precipitates have a tendency to merge. Analysis of the region surrounding the internal γ'/γ'' interface indicates both enrichment of Ni and depletion of Ti by about 7 at.%. This can verify the assumption above stated that internal γ'/γ'' interfaces undergo some compression and serve as barriers hindering diffusion of Nb and Ti atoms between the γ' and

γ'' phases of the co-precipitates. There are only those co-precipitates implied which have developed both γ' and γ'' phases.

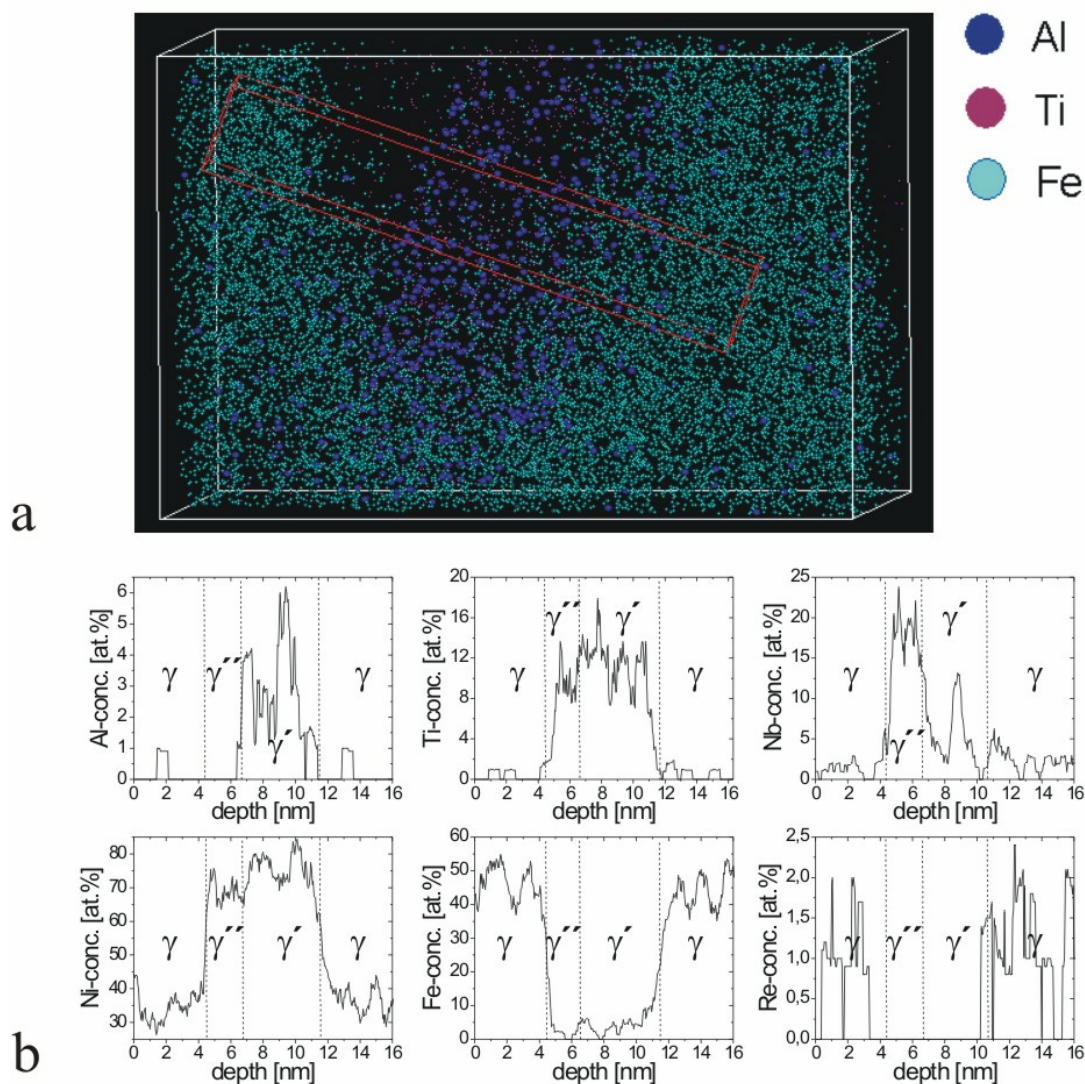


Fig. 3.21. (a) Three-dimensional reconstruction of spatial arrangement of Ti (lilac), Al (dark blue) and Fe (light blue) atoms within a volume of 10x10x15 nm³, representing co-precipitates with the predominant γ' phase. (b) Corresponding depth profiles are built perpendicular to the internal γ'/γ'' interface from left to right with a moving step of 0.05 nm. Concentration values are determined in 0.7 nm thick slices with a cross section of 2x2 nm².

Fig. 3.23 is given in addition to Fig. 3.22b. Here the part of a co-precipitate which has a sandwich-like $\gamma''/\gamma'/\gamma''$ morphology is presented. The Al-enriched region corresponds to a roughly 2 nm thick γ' slice intersecting the co-precipitate. The matrix between two co-precipitates is depleted

in Fe (35.5 ± 2 at.%) and Cr (14.6 ± 2 at.%) and enriched in Ni (44.4 ± 2 at.%) as compared to the averaged value, see Table 3.4. According to the 3DAP measurements, the γ'' phase within the co-precipitate contains approximately 78.28 at.% Ni, 8.58 at.% Ti, 11.65 at.% Nb, 0.38 at.% Cr and 1.12 at.% Fe. Neither Al nor Re has been found in the γ'' phase within experimental uncertainties.

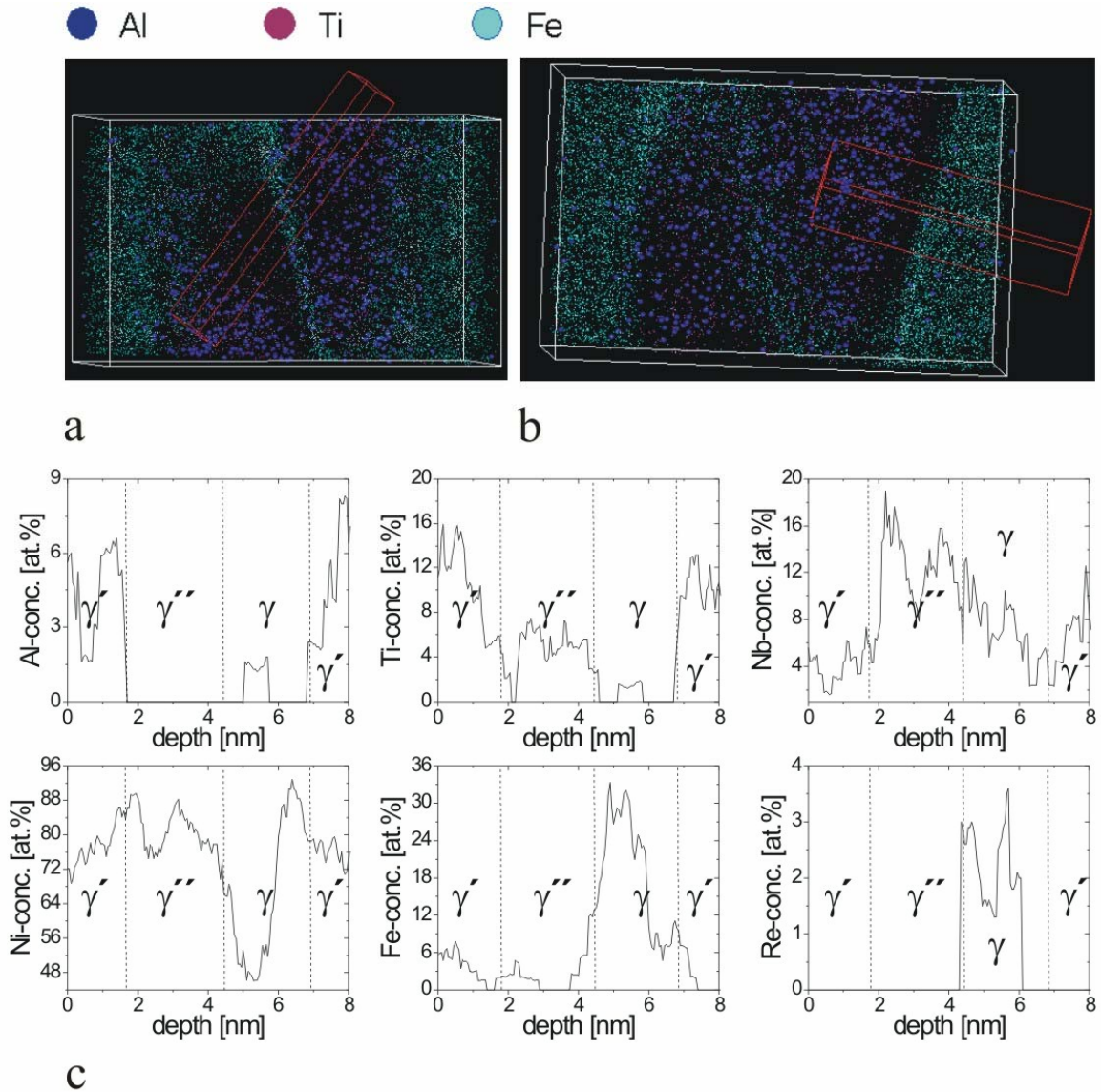


Fig. 3.22. (a) Reconstruction of two co-precipitates which are separated from one another by an approximately 2 nm thick gap. The arrangement of elements like Al (dark blue), Ti (lilac) and Fe (light blue) is shown in a volume of $9 \times 9 \times 14.4$ nm³. (b) The small rotation of the co-precipitate exposes a face of γ' phase coated with a shell of γ'' phase (see the co-precipitate on the right). (c) The depth profiles are built in the red box with a moving step of 0.05 nm, see Fig. 3.22a. Concentration values are determined in 0.7 nm thick slices with a cross section of 1.5×1.5 nm².

An important objective of the present chapter is to investigate the influence of Re on the alloy structure as well as to determine the behavior of Re atoms in the alloy. It is found that Re concentrates mostly in the matrix having a concentration 3 – 4 times higher than in the precipitates, see Table 3.4. Re is not found to create “bow-waves” in the γ matrix ahead of the precipitates [Warren 1998]. Although depth profiles of Re-distributions show the enrichment of Re atoms up to 2 – 3 at.% (Fig. 3.19, 3.20b, 3.21b, 3.22b), this does not prove the existence of Re-enriched shells surrounding interfaces. The behavior of Re has to be rather explained by two factors. Firstly, Re is not homogeneously distributed in the matrix. Secondly, depletion of Re in precipitates causes a small enrichment of Re around the growing precipitates.

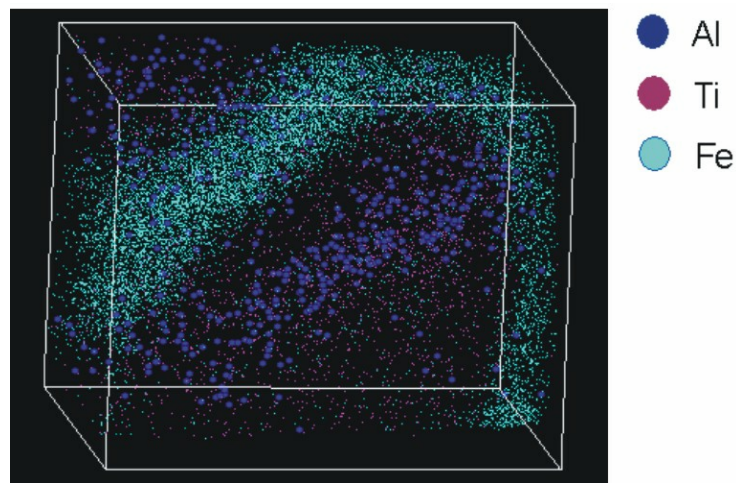


Fig. 3.23. The reconstruction of a co-precipitate which has a sandwich-like $\gamma''/\gamma'/\gamma''$ morphology. The arrangement of elements like Al (dark blue), Ti (lilac) and Fe (light blue) is represented in a volume of $9 \times 9 \times 12.5 \text{ nm}^3$.

The microstructure of the Re-containing Inconel 706 does not exhibit considerable changes after a modified stabilization heat treatment, as compared with the pure alloy (see Fig 3.7 and Fig. 3.16).

The volume fraction of the γ matrix can be evaluated from Table 3.4. We use the same approach as for the pure Inconel 706 after modified stabilization heat treatment. We ignore again the small amount of other phases, e.g. that of the η phase (which mostly concentrates at the grain boundaries) and evaluate equation (3.2) only for the matrix formers Cr, Ni and Fe. Thus we obtain $f_\gamma = 88 \pm 3 \%$ for the volume fraction of the matrix.

Table 3.4. Chemical composition (in at.%) of phases in Re-containing Inconel 706 alloy as measured by three-dimensional atom probe (“ind” and “copr” mean individual precipitates and co-precipitates respectively).

	Ni	Al	Ti	Nb	Cr	Fe	Re
γ	36.9 ± 1	0.36 ± 0.04	0.38 ± 0.05	0.7 ± 0.2	17.2 ± 1	43.6 ± 0.5	0.79 ± 0.05
γ'_{ind}	76.1 ± 2	3.1 ± 0.3	12.1 ± 2	5.2 ± 1	0.78 ± 0.2	2.6 ± 0.4	0.25 ± 0.1
γ'_{copr}	76.45 ± 3	3.36 ± 0.8	12.63 ± 2	4.67 ± 1	0.38 ± 0.2	2.31 ± 0.3	0.20 ± 0.1
γ''_{ind}	75.26 ± 2	0.11 ± 0.1	9.15 ± 1	12.92 ± 2	0.63 ± 0.3	1.62 ± 0.9	0.32 ± 0.2
γ''_{copr}	75.02 ± 3	0.1 ± 0.1	8.77 ± 2	13.33 ± 3	0.85 ± 0.3	1.66 ± 0.6	0.274 ± 0.2

3.2.2 Microstructure after modified stabilization heat treatment and after ageing at 750°C for 750 h

As can be understood from Fig. 3.24 [DFG 2002], the plate-like η precipitates appear in the grain interior. They differ from the γ'' needles on the basis of their spatial orientation. An examination at higher magnification (Fig. 3.25) shows that in comparison with Fig. 3.16a small precipitates have increased in size. The $[001]_{\gamma}$ zone axis diffraction pattern (inset in Fig. 3.25a) clearly displays superlattice reflections from both the γ' and γ'' phases. However, in order to clarify the phase of particles of different morphology a number of SAED images of $\{100\}$ planes are taken. The locations which were investigated by this way are marked in Fig. 3.25. The diffraction image Fig. 3.26a corresponds to location 1 and shows the pattern of a γ' phase. There is also the weak pattern of γ'' . At location 2 a needle-like precipitate yields the pattern of a γ'' phase (see Fig. 3.26b), though the weak pattern of γ' phase is also visible. The patterns from location 3 in the middle of a round precipitate are illustrated in Fig. 3.26c. They correspond to both the γ' and γ'' phases. Another needle-like precipitate was investigated by diffraction from location 4. The corresponding pattern is shown in Fig 3.26d. It clearly identifies the precipitate as γ'' . The needle-like γ'' precipitates indicated by numbers “2” and “4” are perpendicular to each other. The respective SAD images also present different orientations of the γ'' phase (compare Fig. 3.26b and 3.26d) and show the relationship between the orientations of the γ'' precipitates and the orientation of their lattice in the matrix. The needle-like γ'' precipitates are approximately 200 nm long and are oriented in the $\langle 001 \rangle_{\gamma}$ directions.

The seventh precipitate produces a SAED image as shown Fig. 3.27a, showing the superlattice reflection from the γ' phase, but also some weak patterns of the γ'' . This can be explained by the

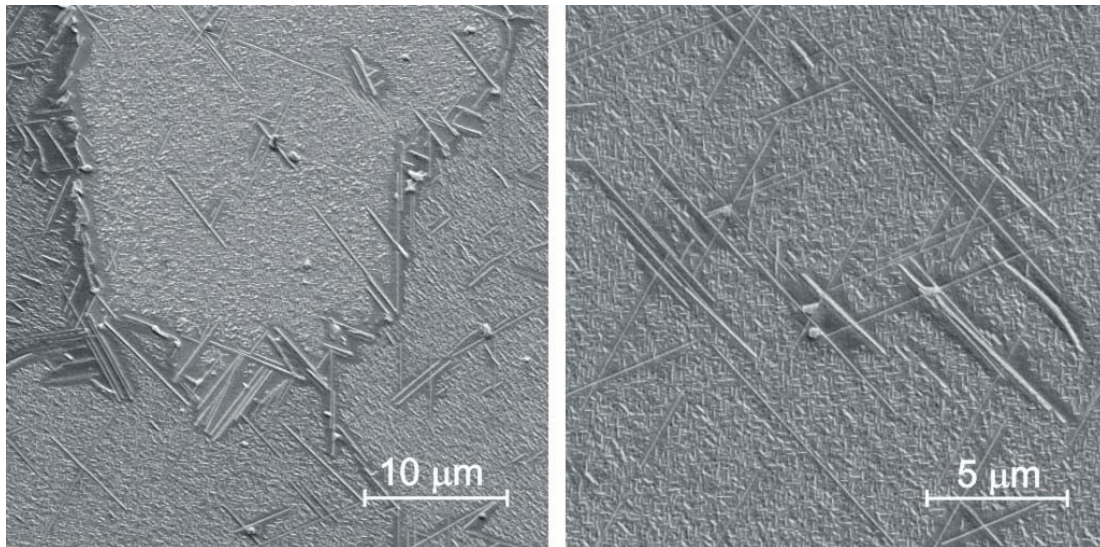


Fig. 3.24. SEM image introduces a typical microstructure of MST heat treated Re-alloyed Inconel 706 after ageing at 750°C for 750 h: (a) grain boundary and (b) intracrystalline region.

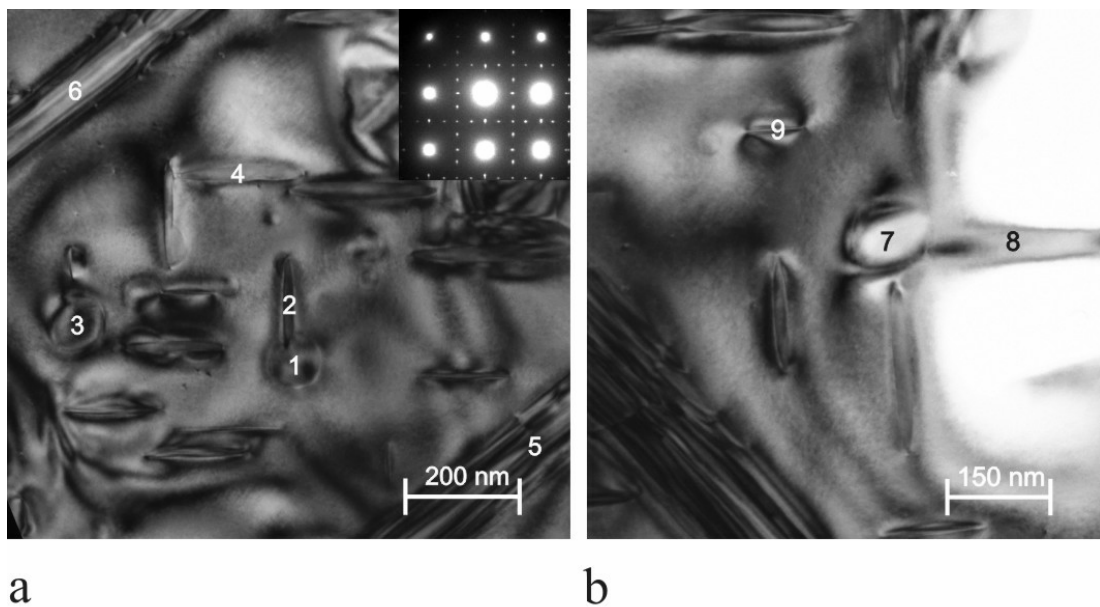


Fig. 3.25. Bright field TEM micrograph showing the microstructure of Re-containing Inconel 706 alloy heat treated under MST conditions after further ageing at 750°C for 750 h. A $[001]_{\gamma}$ zone axis diffraction image is represented in the inset. The places of interest are numbered (a) 1 – 6 and (b) 7 – 9. The images in (a) and in (b) have the same orientation showing the microstructure of two neighboring areas.

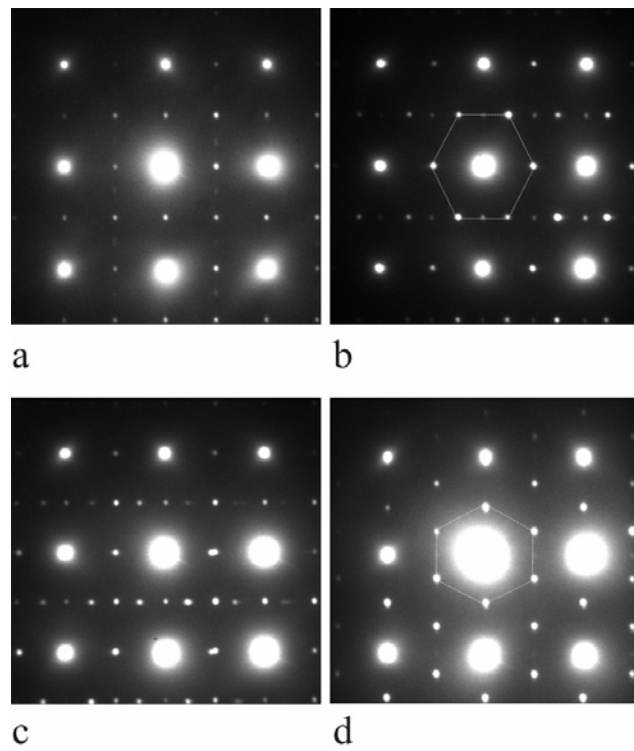


Fig. 3.26. Selected area diffraction from locations (a) 1, (b) 2, (c) 3 and (d) 4 as given in Fig. 3.25a.

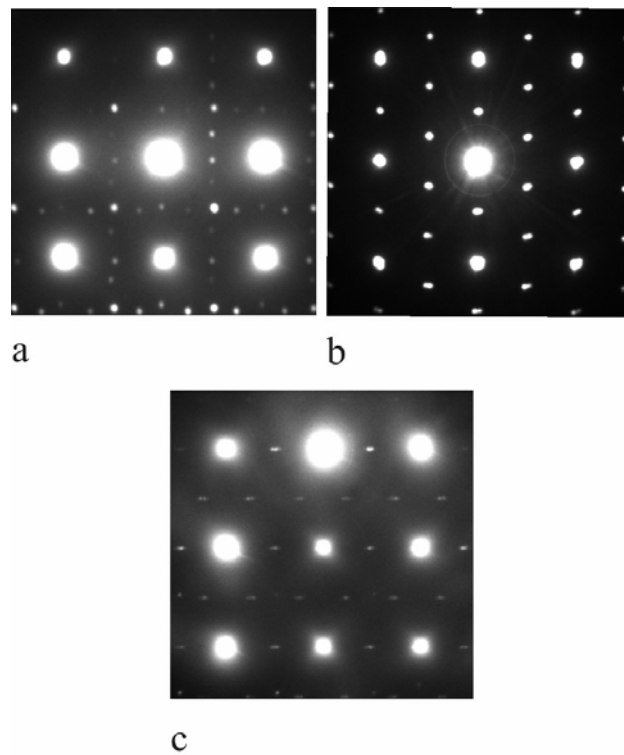


Fig. 3.27. Selected area diffraction from locations (a) 7, (b) 8 and (c) 9 as given in Fig. 3.25b.

vicinity of two needles which have different orientations. The SAED image from the “eighth” precipitate is represented in Fig. 3.27b, clearly identifying the needle as a γ'' precipitate (as expected). In such a way it is found out that rounded precipitates (like those numbered as 1, 3 and 7 in Fig. 3.25) are γ' .

At first sight the ninth precipitate looks like a bean-shaped precipitate. The SAED image from this precipitate shows the typical pattern of the γ'' phase (Fig. 3.27c). The precipitate is probably a γ'' needle, as mentioned above. It is just smaller than other γ'' precipitates.

The precipitates 5 and 6 are noticeably larger than all other precipitates mentioned above. It is obvious that they differ also in their orientation as compared with γ'' needle-like precipitates. The SAED images of these precipitates are summarized in Fig. 3.28. These patterns are very similar to those of the γ' phase.

In order to investigate the nature of the large precipitate in more detail, the foil was rotated into a $\{110\}$ pole. Such a bright field TEM image is showing in Fig. 3.29a. The electron diffraction image was taken from location 10, corresponding to the precipitate of interest. The pattern in Fig. 3.29b corresponds to a η phase. The morphology of η precipitates can be derived from Fig. 3.29c. They grow into micrometer sized plates. The matrix was not in any pole in this case. However, the SAED image taken from the plate 11 (Fig. 3.29d) clearly shows the diffraction pattern which is typical for the hexagonal lattice.

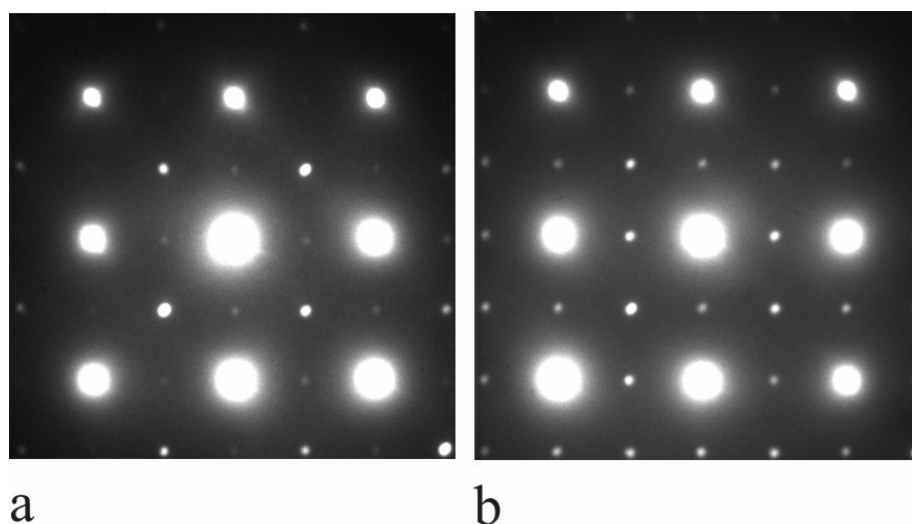


Fig. 3.28. Selected area diffraction from locations (a) 5 and (b) 6. The arrangement of these places is given in Fig. 3.25a.

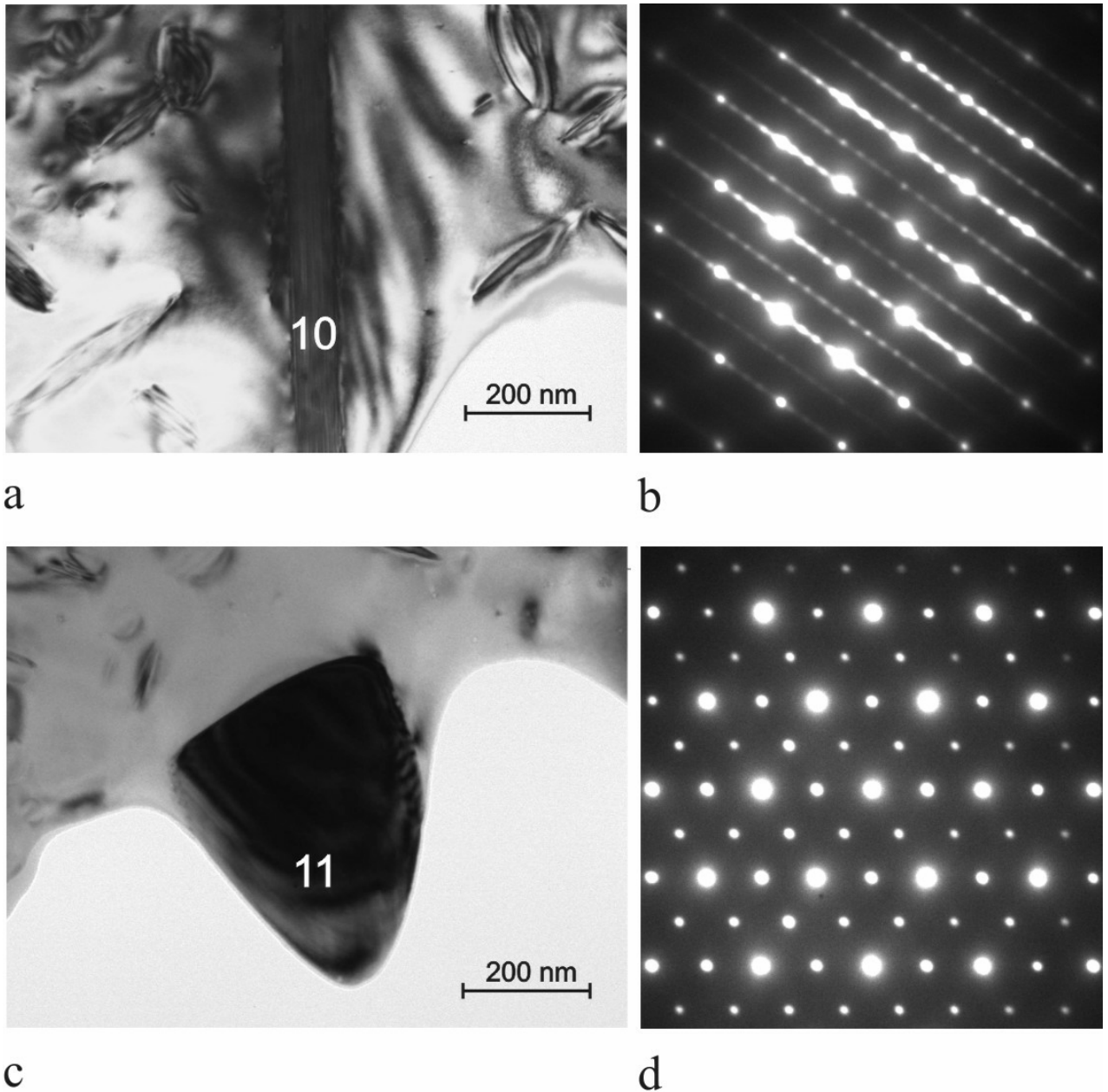


Fig. 3.29. Bright field TEM micrograph the Re-containing Inconel 706 alloy heat treated under MST conditions after further ageing at 750°C for 750 h. (a) Large precipitate; (b) $[110]_{\gamma}$ zone axis selected area electron diffraction pattern taken from location 10 in (a); (c) large plate-like precipitate; (d) selected area electron diffraction pattern taken from location 11 in (c).

Fig. 3.30a displays the reconstructed positions of Ti (purple), Al (dark blue) and Fe (light blue) atoms in a volume of $14 \times 14 \times 235 \text{ nm}^3$, as measured by 3DAP. Three precipitates enriched in Ti are clearly visible. One sees only parts of the precipitates since these precipitates are larger than reconstructed volume. The red arrow gives the direction of the depth analysis. The corresponding depth profiles are given in Fig. 3.30b. Concentration values are determined in 0.5 nm thick slices with a cross section of $4.5 \times 4.5 \text{ nm}^2$. The cross section was chosen larger than before because the

precipitate of interest is much more larger than the precipitates investigated above. The depth profiles show that the transition between Fe-enriched and Fe-depleted regions occurs within 2 nm. It can be clearly seen that Fe enrichment consists of a “bow wave” in the matrix ahead of the growing γ'' phase. Ti experiences a sharp reduction already at the beginning of the transition region of Fe. Re concentrates in the matrix. In contrast to Fe, Re does not show any features of a “bow wave” enrichment. Two precipitates at the right of the reconstructed volume are shown in detail in Fig. 3.31a. The image indicates that these precipitates are delimited by means of a thin matrix-boundary.

Moreover, an enrichment of Al atoms is evident in one of the precipitates (see the precipitate on the right), indicating the existence of a γ' phase as well. Probably the precipitates tend to merge. Therefore, the distributions of atoms close to the boundary is of great interest. Therefore, depth profiles were taken through the boundary along the red box, as shown in Fig. 3.31a. The results for the basic elements are represented in Fig. 3.31b. Fe has an enrichment up to 14 at.% within the boundary. The decrease of Fe-concentration happens within less as 2 nm. It means that Fe-atoms diffuse along the boundary towards the matrix. Re is practically missing in the investigated volume, whereas Nb experiences depletion by 4 at.%.

The average composition of the matrix and of the γ'' phase is given in Table 3.5. The average concentration of the γ'' phase was derived from three precipitates shown in Fig. 3.30a.

Table 3.5. Chemical composition (in at.%) of phases in Re-containing Inconel 706 alloy after ageing at 750°C for 750 h as measured by three-dimensional atom probe.

	Ni	Al	Ti	Nb	Cr	Fe	Re
γ	30.9 ± 0.5	0.42 ± 0.02	0.69 ± 0.01	1.7 ± 0.2	21.1 ± 0.2	44.5 ± 0.5	0.75 ± 0.01
γ''	71.1 ± 2	0.13 ± 0.02	8.9 ± 0.8	17.3 ± 1	0.56 ± 0.04	1.96 ± 0.08	0.05 ± 0.04

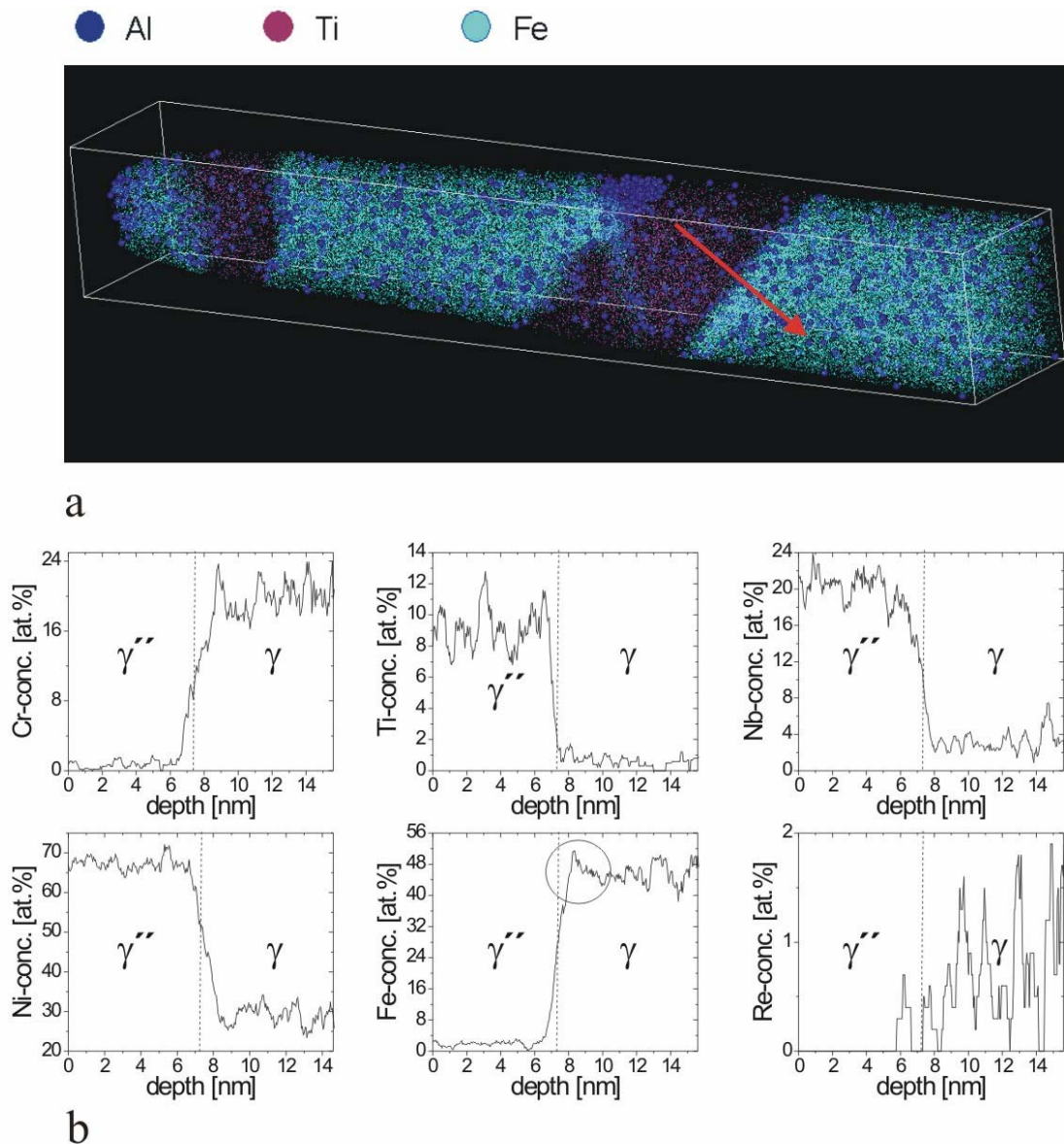


Fig. 3.30. (a) Three-dimensional reconstruction of the spatial arrangement of Ti (purple), Al (dark blue) and Fe (light blue) atoms in a volume of $14 \times 14 \times 235 \text{ nm}^3$, representing three γ'' precipitates embedded into the matrix. (b) Depth profiles are constructed perpendicular to the external γ''/γ interface from left to right with a moving step of 0.05 nm. Concentration values are determined in 0.5 nm thick slices with a cross section of $4.5 \times 4.5 \text{ nm}^2$.

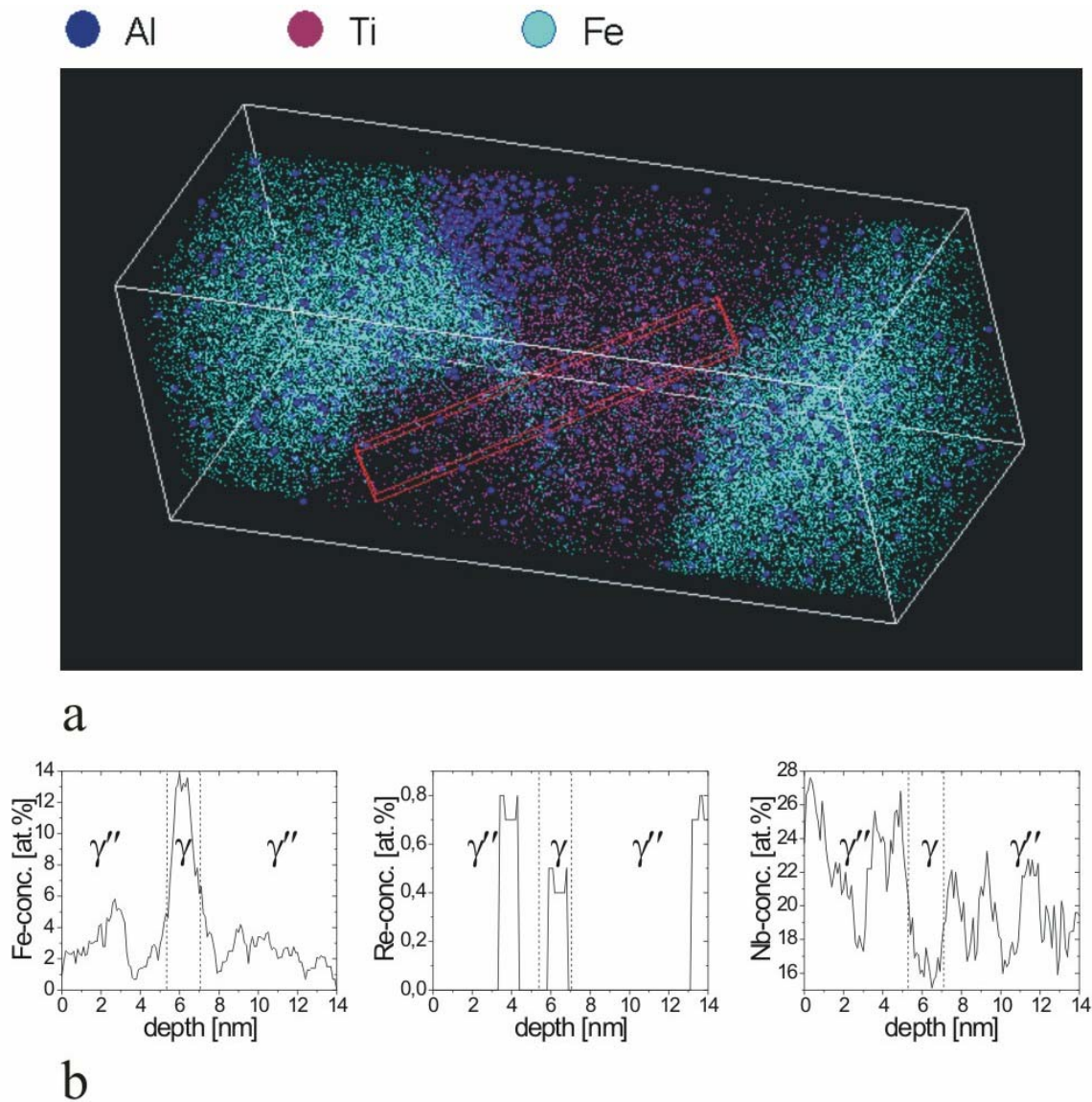


Fig. 3.31. (a) Three-dimensional reconstruction of the spatial arrangement of Ti (purple), Al (dark blue) and Fe (light blue) atoms in a volume of $11.4 \times 11.4 \times 31.4 \text{ nm}^3$, representing in detail two close γ'' precipitates, shown in Fig. 3.30a. (b) Depth profiles are taken perpendicular to the internal matrix-boundary from left to right with a moving step of 0.1 nm. Concentration values are determined in 1 nm thick slices with a cross section of $2 \times 2 \text{ nm}^2$.

3.3 DT 706 superalloy

3.3.1 Microstructure after modified stabilization heat treatment

Fig. 3.32a shows a bright field TEM micrograph and a corresponding $[001]_{\gamma}$ selected area electron diffraction pattern of the DT 706 alloy after modified stabilization heat treatment. The microstructure consists of primary and secondary precipitates with two size distributions embedded in a matrix. Whereas the large precipitates with sizes 40 – 60 nm are cubic, the small precipitates are about 20 nm large and have spherical morphology. The superlattice reflections in the diffraction pattern in Fig. 3.32a arise from γ' and γ'' precipitates [Paulonis 1965]. The dark field image shown in Fig. 3.32b was performed with the beam reflection $\vec{g} = [110]$, which is allowed for both γ' and γ'' phases [Gao 1995]. As can be seen from Fig. 3.32b γ' phases grows into cubic precipitates having their six faces coated with a shell of γ'' phase. However the surface of the γ' precipitates is not fully covered. The modified stabilization heat treatment produces also long plate-like η precipitates that are formed mainly on the grain boundaries and some in the grain interior (see Fig. 3.33).

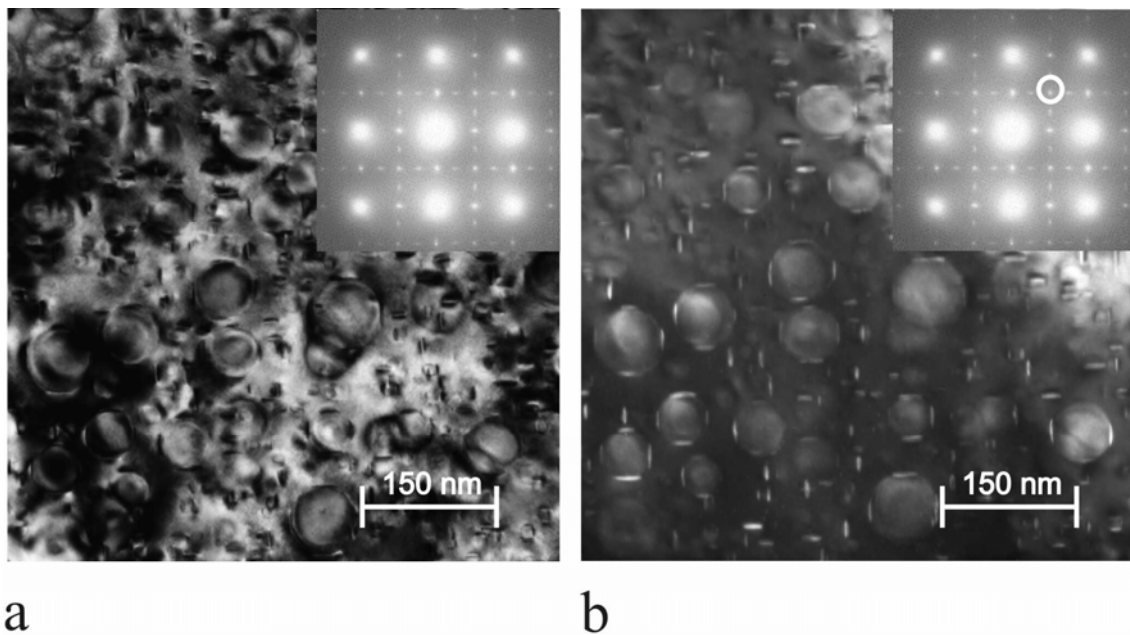


Fig. 3.32. Microstructure of DT 706 alloy after MST heat treatment: (a) bright field TEM image and (b) dark field TEM image of fine γ' cubes coated with shells of γ'' phase. $[001]_{\gamma}$ zone axis diffraction patterns are given in the insets. The dark field image was performed using the diffraction vector $\vec{g} = [110]$ (as indicated in the image by the circle).

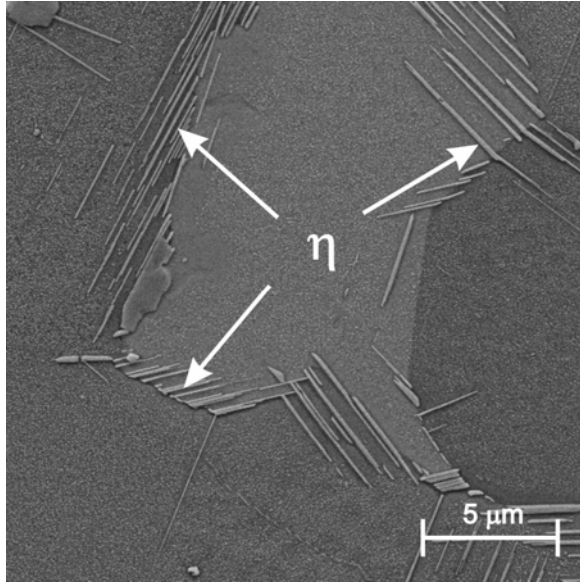


Fig. 3.33. SEM image showing typical plate-like η precipitates at the grain boundaries formed in DT 706 alloy after MST heat treatment [DFG 2002].

The 3DAP analysis is shown in Fig. 3.34. 3D reconstruction of the positions of the Ti (red) and Al (blue) atoms was carried out in a volume of $13 \times 13 \times 1415 \text{ nm}^3$. As the reconstructed volume was too long, only parts of the volume are shown which contain at least one precipitate. All reconstructed precipitates are enriched both in Ti and Al. Therefore, they are interpreted as γ' particles. Fig. 3.34 clearly shows the presence of secondary γ' precipitates (Nr. 2, 6, 7, 9, 10, 11). Some of them are small enough to be reconstructed in full size. The diameter of the secondary precipitates ranges from 6 to 25 nm. The sizes of the primary and secondary precipitates are in accordance with the estimate based on the TEM micrograph given above.

The average compositions of the matrix and the γ' phase are given in Table 3.6. Precipitate no. 2 (γ'_{sec}) slightly deviates in Al content from the averaged concentration of the γ' precipitates and is also the smallest one to be found in the reconstructed volume (see Fig. 3.34).

The volume fraction of the γ matrix can be evaluated from Table 3.6. The same approach is used as for pure Inconel 706 after modified stabilization heat treatment, see equation (3.2). We ignore the small amount of other phases, e.g. that of the η phase (which mostly accumulates at grain boundaries) and evaluate equation (3.2) only for the matrix formers Cr, Ni and Fe. Thus we obtain $f_{\gamma} = 76 \pm 4 \%$ for the volume fraction of the matrix.

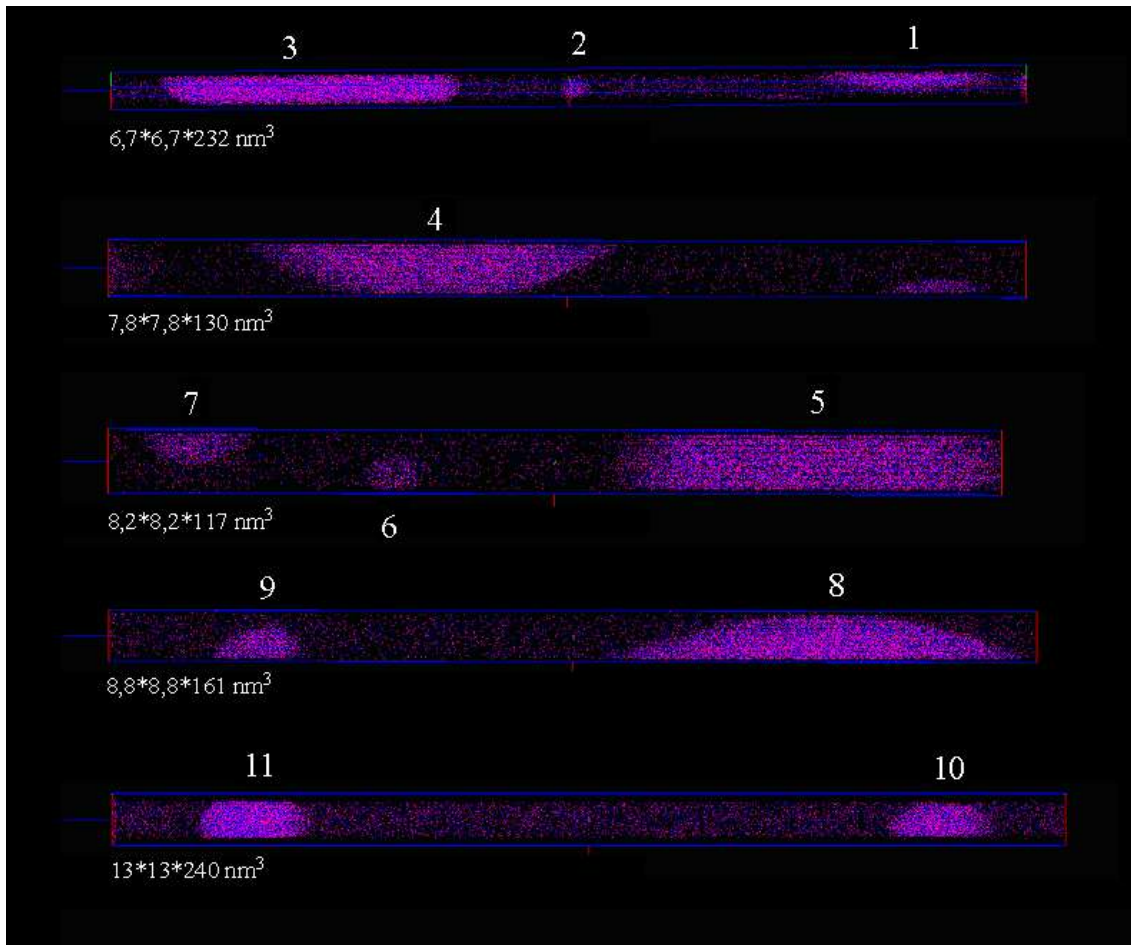


Fig. 3.34. Three-dimensional reconstruction of Ti (lilac) and Al (dark blue) atom positions in DT 706 after modified stabilization heat treatment. The entire reconstructed volume is $13 \times 13 \times 1415 \text{ nm}^3$.

Table 3.6. Chemical composition (in at.%) of γ' phase and matrix in DT 706 alloy as measured by three-dimensional atom probe (“pr” and “sec” denote primary and secondary γ' precipitates, respectively).

		Ni	Al	Ti	Nb	Cr	Fe
γ		44.8 ± 0.4	0.46 ± 0.03	0.57 ± 0.01	1.8 ± 0.2	24.3 ± 0.3	28.2 ± 0.6
Precipitate, no.	1	70.53	8.57	12.39	5.11	0.42	2.98
	2	68.93	11.01	11.01	5.85	0.97	2.22
	3	70.05	7.95	13.96	4.90	0.56	2.59
	4	70.00	7.92	13.92	5.12	0.54	2.51
	5	69.50	8.04	14.48	4.87	0.54	2.58
	6	69.44	7.23	12.94	6.61	0.63	3.15
	7	72.62	8.51	10.70	4.74	0.41	3.02
	8	70.29	8.16	13.86	4.64	0.47	2.59
	9	68.71	7.67	12.22	7.59	0.68	3.13
	10	69.75	9.17	11.70	5.77	0.76	2.85
	11	70.40	9.46	10.69	6.39	0.44	2.62
γ'_{pr}		70.1 ± 0.8	8.1 ± 0.6	13.7 ± 1	4.9 ± 0.4	0.5 ± 0.1	2.7 ± 0.4
γ'_{sec}		69.9 ± 3	8.8 ± 2	11.5 ± 2	6.2 ± 2	0.7 ± 0.4	2.8 ± 0.6

3.3.2 Microstructure after modified stabilization heat treatment and after ageing at 750°C for 750 h

The microstructure of DT 706 after ageing at 750°C for 750 h is shown in Fig. 3.35. The diffraction pattern in the $[001]_{\gamma}$ zone axis (insets in Fig. 3.35a and 3.35b) show the presence of both γ' and γ'' precipitates. The dark field image shown in Fig. 3.35b was obtained using $\vec{g} = [110]$. The superlattice reflections from the γ'' precipitates appear weaker as compared with the analogous reflections shown in Fig. 3.32. The γ'' phase covers the faces of cubic γ' precipitates. Not all the faces are covered, as can be seen from the Fig. 3.35b. The γ' precipitates have grown up to 100 nm after this heat treatment.

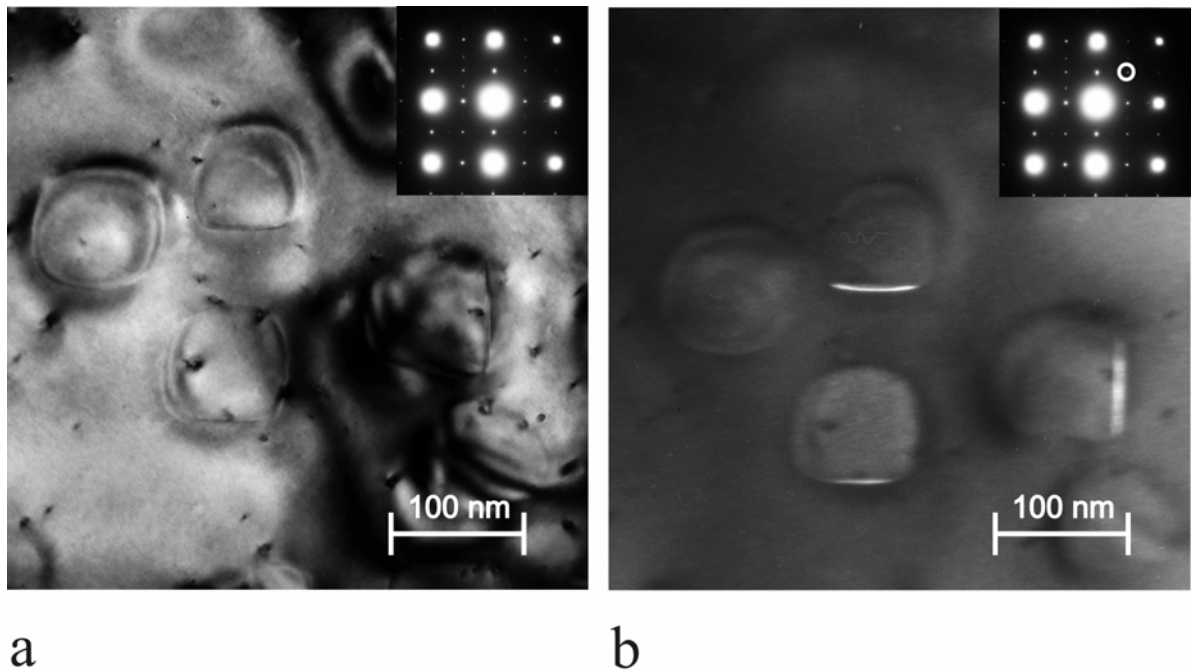


Fig. 3.35. Microstructure of DT 706 after MST and ageing at 750°C for 750 h: (a) bright field TEM image and (b) dark field TEM image of fine γ' cubes coated with shells of γ'' phase. $[001]_{\gamma}$ zone axis diffraction patterns are given as insets. The dark field image was performed using the diffraction vector $\vec{g} = [110]$ (as indicated in the image by the circle).

Fig. 3.36a shows the reconstruction of Ti, Al, Nb and Fe atom positions in a volume of $7.2 \times 7.2 \times 12 \text{ nm}^3$. Three regions enriched in Fe, Nb and Al and Ti are visible. Since Al is a constituent of the $\text{Ni}_3(\text{AlTi})$ based γ' phase, the region enriched in Al (on the left side of the reconstructed volume) has been identified as γ' phase. The Nb-enriched region was identified as the $\text{Ni}_3(\text{NbTi})$

based γ'' phase. Both regions represent a γ'/γ'' co-precipitate on the left side of the volume. The remaining region, depleted in both Ti and Al and enriched in Fe, is the γ matrix.

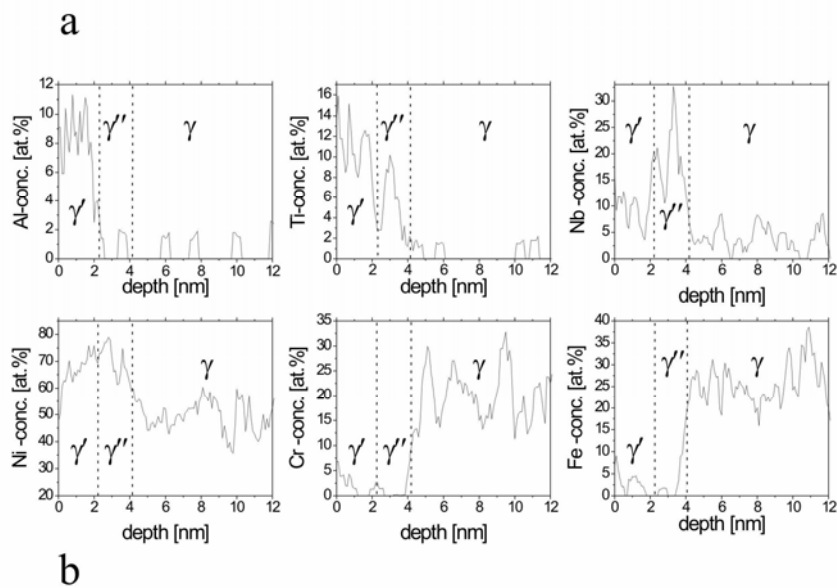
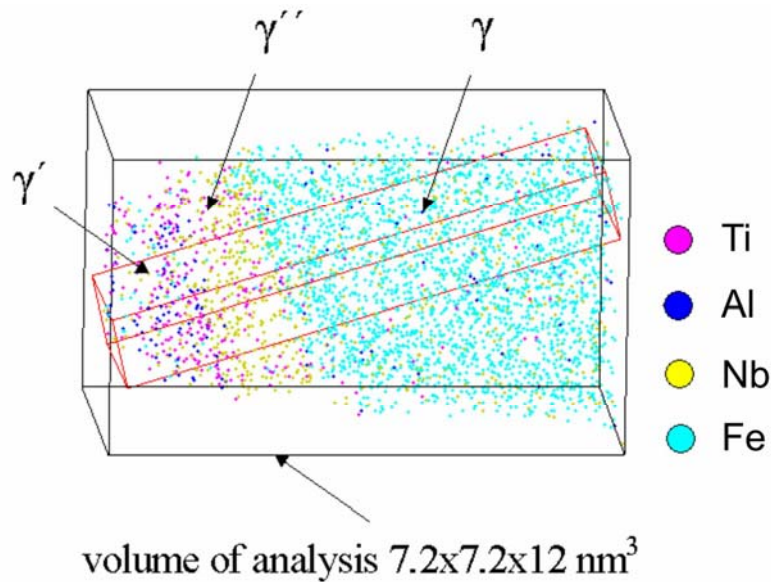


Fig. 3.36. (a) Three-dimensional elemental mapping of Ti (lilac), Al (blue), Nb (dark yellow) and Fe (light blue) after ageing of DT 706 for 750 h at 750°C. The analysed volume of $7.2 \times 7.2 \times 12 \text{ nm}^3$ contains a part of a γ'/γ'' co-precipitate. The indicated red box through the co-precipitate was used for evaluating the (b) concentration depth profiles. Concentration values were determined in slices of $2 \times 2 \times 0.5 \text{ nm}^3$ with a step of 0.1 nm.

The chemical nature of the interfaces γ'/γ'' and γ/γ' is of particular interest. The micro-chemical information near and across the interfaces is obtained from the concentration depth profiles which were taken along a box of $2 \times 2 \times 12 \text{ nm}^3$ indicated in the analyzed volume. This box was selected in such a way that the γ'/γ'' interface is cut perpendicularly. The corresponding set of depth profiles for the main alloying elements is plotted in Fig. 3.36b. The dashed lines indicate γ'/γ'' and γ''/γ interfaces. The phase boundary between γ' and γ'' is sharp being just a few atomic planes wide. The boundary between γ'' and the matrix is less sharp, about 1 nm wide. The concentration distribution of Nb within the γ'' phase is not uniform. A depletion at the interface γ''/γ was observed. The thickness of the γ'' precipitates is about 2 nm as can be seen in Fig. 3.36. Cr is depleted at the γ''/γ interface.

A γ'/γ interface was also investigated by 3DAP. Fig. 3.37a shows the three dimensional reconstruction of Ti and Fe atoms in a volume of $10.3 \times 10.3 \times 21 \text{ nm}^3$. The region enriched in Fe corresponds to the matrix, the region enriched in Ti to the γ' precipitate. Fig. 3.37a represents only a part of a γ' precipitate. Therefore, it is not evident whether the precipitate is an individual- or a co-precipitate.

The depth profiles through the interface are plotted in Fig. 3.37b. The profiles were taken along the box of $2 \times 2 \times 7.5 \text{ nm}^3$ shown in Fig. 3.37a. The crosshatched area shows the transition region (about 1 nm thick) from the γ' precipitate to the matrix. This region is enriched in Ni and depleted from Nb, Ti and Cr.

To facilitate comparison of the phase chemistry of the matrix, individual precipitates and co-precipitates, the average composition of each phase is listed in Table 3.7. The composition of the η phase measured by EDX is also given.

Table 3.7. Chemical phase compositions (in at.%) as measured by 3DAP in DT 706 after ageing at 750°C for 750 h. The composition of the η phase was measured using EDX.

	Ni	Al	Ti	Nb	Cr	Fe
γ	50.0 ± 0.2	0.54 ± 0.03	0.44 ± 0.03	1.4 ± 0.05	21.27 ± 0.2	26.36 ± 0.2
$\gamma'_{\gamma'/\gamma''}$	70.6 ± 2.8	6.6 ± 1.5	12.6 ± 2.0	7.3 ± 1.6	0.4 ± 0.4	2.5 ± 0.9
$\gamma''_{\gamma'/\gamma''}$	69.7 ± 3.2	0.74 ± 0.6	7.5 ± 1.8	16.9 ± 2.6	3.1 ± 1.2	2.0 ± 1
$\gamma'_{\gamma'/\gamma}$	72.5 ± 1.3	4.20 ± 0.6	12.5 ± 0.9	7.8 ± 0.8	0.64 ± 0.2	2.34 ± 0.4
η	71.4 ± 3	4.7 ± 2	11.3 ± 2	5.4 ± 0.8	2.68 ± 2	4.5 ± 2

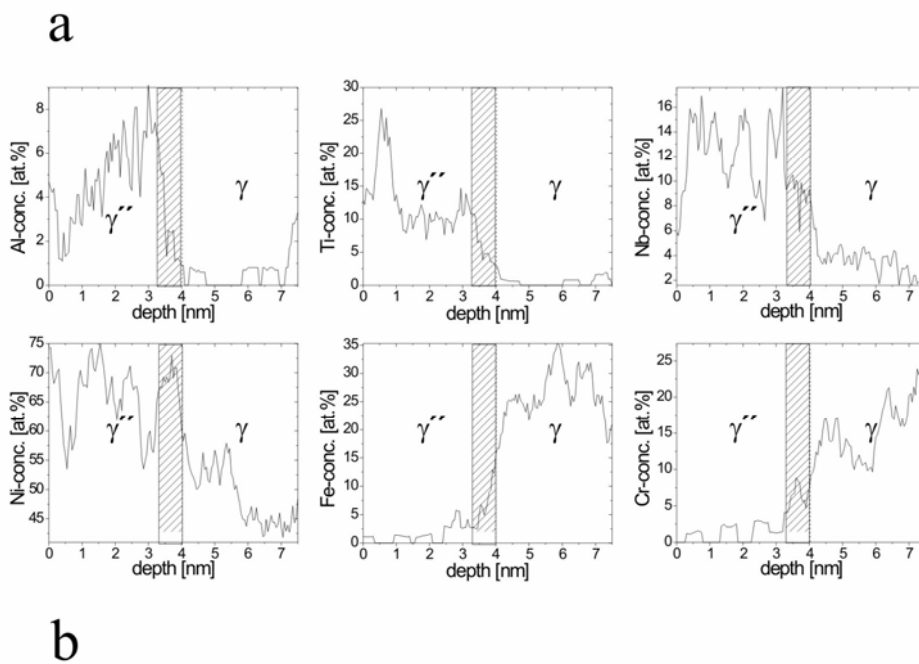
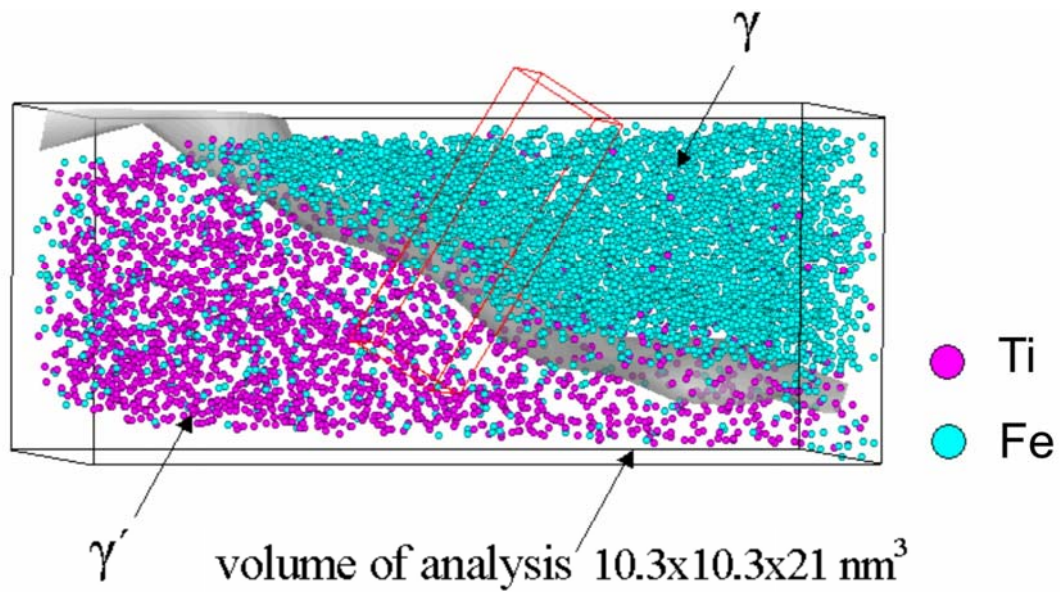


Fig. 3.37. (a) Three-dimensional elemental mapping of Ti (lilac) and Fe (blue) in DT 706 after ageing at 750°C for 750 h. A γ' precipitate is partially visible. The analysed volume is $10.3 \times 10.3 \times 21 \text{ nm}^3$ large. The iso-surface (grey) corresponds to 5.8 at.% Ti. (b) Corresponding depth profiles are constructed along the red box with a moving step 0.1 nm. Concentration values were determined in $2 \times 2 \times 0.5 \text{ nm}^3$ large slices.

3.3.3 Microstructure after modified stabilization heat treatment and after ageing at 750°C for 5000 h

Fig. 3.38a shows a bright field TEM micrograph and a corresponding $[001]_{\gamma}$ selected area electron diffraction pattern of the DT 706 alloy after modified stabilization heat treatment and after ageing at 750°C for 5000 h. The dark field image shown in Fig. 3.38b was obtained using a diffraction vector $\vec{g} = [110]$. The $[001]_{\gamma}$ zone axis diffraction patterns (insets in the Fig. 3.38a and 3.38b) show the presence of γ' precipitates only.

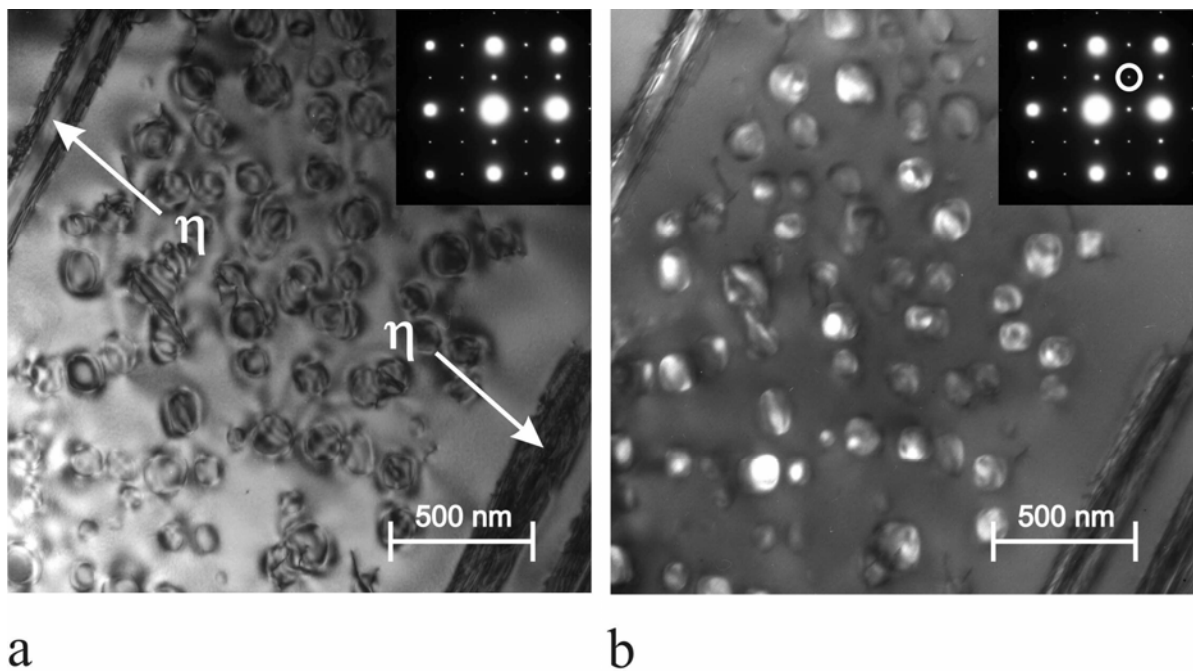


Fig. 3.38. Microstructure of DT 706 alloy after MST heat treatment and ageing at 750°C for 5000 h: (a) bright field TEM image and (b) dark field TEM image of fine γ' cubes. $[001]_{\gamma}$ zone axis diffraction patterns are given as insets. The dark field image was obtained using a diffraction vector $\vec{g} = [110]$ (as indicated in the image by the circle).

The diffraction pattern does not show any superlattice reflections from γ'' precipitates. Therefore, the γ'' plates covering the faces of cubic γ' precipitates were not detected from the dark field micrograph, see Fig. 3.38b. The γ' precipitates have grown up to about 150 nm after this heat treatment. Beside the γ' precipitates, about 200 nm thick η precipitates are also observed in the TEM micrographs. The vicinity of these η precipitates is free of any γ' precipitates within 200 nm.

The SEM image in Fig. 3.39 shows that η precipitates grow not only at the grain boundaries but in the grain interior as well.

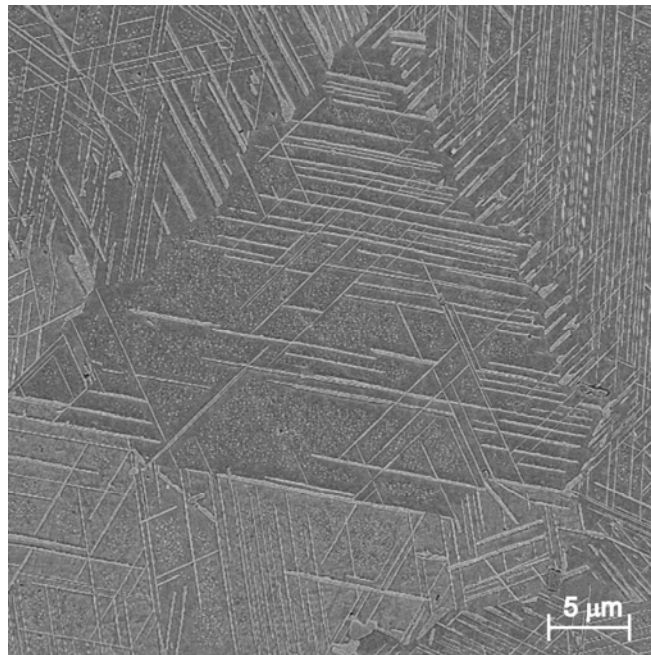


Fig. 3.39. SEM image with typical plate-like η precipitates at the grain boundaries and in the grain interior formed in DT 706 after MST heat treatment and ageing at 750°C for 5000 h.

The average chemical compositions of the γ , γ' and η phases measured by EDX are listed in Table 3.8.

Table 3.8. Chemical composition of phases (in at.%) as measured by EDX in DT 706 after ageing at 750°C for 5000 h.

	Ni	Al	Ti	Nb	Cr	Fe
γ	49.3 ± 0.6	1.5 ± 0.8	1.2 ± 0.8	1.1 ± 0.2	21.6 ± 0.2	25.35 ± 2
γ'	66.7 ± 3	9.6 ± 2	10.3 ± 2	2.9 ± 0.8	4.1 ± 2	6.4 ± 2
η	67.2 ± 4	6.2 ± 1	9.1 ± 1	5.5 ± 1	5 ± 2	7.1 ± 3

4 Calculation of internal coherent stresses and elastic strain energies in Inconel 706 after direct ageing

4.1 Motivation

As mentioned in the introduction (Chapter 1) the morphology development of the secondary phases γ' , γ'' and η in Inconel 706 during exposure to a service temperature of 750°C is of great interest, as it is directly related to the alloy performance under these conditions. The equilibrium microstructure depends on the elastic strain energy that arises from a precipitate misfit [Khachaturyan 1983]. Thus, one needs to investigate the local mismatch-induced elastic stress and energy distributions in the multi-phase Inconel 706 system to better understand the microstructure development.

After a heat treatment Inconel 706 is in a quasi-equilibrium state: changes of the microstructure due to the chemical potential are not expected even after a long time at the service temperature. The phases neither nucleate nor dissolve. Changes of the microstructure are related only to the minimization of elastic strain energy which induces diffusion of elements.

In the present study attention is focused on Inconel 706 after DA heat treatment. The precipitates to be investigated are individual γ' and γ'' precipitates and γ'/γ'' co-precipitates. The behavior of the η phase is not of interest since it does not nucleate after DA heat treatment (see section 3.1.2).

The actual question currently is: Why does co-precipitation take place? If co-precipitates are expected to be more stable at further heat treatment, their morphology evolution would be of special importance. Finite-element (FE) modeling can be useful as it allows for an effective calculation of elastic stress and energy distributions within matrix and inclusions [Müller 1992, Chen 1999].

The aim of the work described in this chapter is to use a finite-element method (FEM) to compute coherency strain effects of inhomogeneous coherent particles with a non-dilatational misfit strain on the morphological evolution in the alloy. The stability of microstructure after DA heat treatment will be analyzed in relationship to energy and mean normal stress distributions. A theory of monophasic ellipsoidal inclusions in an anisotropic matrix with different elastic modules has already been developed [Khachaturyan 1983, Jong 1977]. FEM is applied as complicated multiphase co-precipitates have to be considered.

4.2 Material model

The morphology of the real precipitates in Inconel 706 is shown in Fig. 3.4a, Fig. 3.5a, Fig. 3.8 and Fig. 3.9. The images shows a prolate spheroidal shape of inclusions. The model morphology of individual- and co-precipitates is shown schematically in Fig. 4.1. The prolonged spheroidal precipitates are simulated with a major axis $2c = 10$ nm and an aspect ratio $\frac{c}{a} = 1.5$ [Kindrachuk 2004]. The box sizes d and D (see Fig. 4.2a and Fig. 4.2b) are chosen such to be comparable with the given volume fractions of the phases. In particular a 75 vol.% of the γ matrix is used [Kindrachuk 2004, Mukherji 2003A], which leads to $\frac{D}{d} = 1.5$. The interaction between two co-precipitates is investigated as shown in Fig. 4.2c, where the distance between the neighboring precipitates $F = \frac{5}{2} \cdot (d - a) = 2.38$ nm. The lattice parameters are used in the present 3-dimensional FE study for all the phases as measured by means of laboratory and synchrotron X-ray diffraction after direct ageing heat treatment on bulk samples [Mukherji 2003A]. The $\langle 100 \rangle_{\gamma'}$ directions of γ' ($a_{\gamma'} = 3.579$ Å) are parallel to those of the f.c.c. matrix ($a_{\gamma} = 3.591$ Å). The c -axis of the tetragonal γ'' is parallel to the long dimension of the individual particles and lies along the $\langle 100 \rangle_{\gamma}$ directions of the matrix. According to [Shibata 1996] the orientation at the γ'/γ'' interface is subjected to the conditions $(001)_{\gamma''} // \{001\}_{\gamma'}$ and $[100]_{\gamma''} // \langle 100 \rangle_{\gamma'}$, as shown in Fig. 4.1. The lattice constants for tetragonal γ'' are $a_{\gamma''} = 3.569$ Å and $c_{\gamma''} = 7.572$ Å. Since the difference between the lattice parameter of the γ'' phase and the matrix along the c -direction is so large, it is suggested that the γ'' phase has a vacancy type misfit of 5.3 % in the $[001]_{\gamma''} // [100]_{\gamma}$ direction, when one unit cell of γ'' is fitted into two unit cells of the matrix. Consequently, a purely dilatational mismatch $e_{ij}^0 = -0.0033 \cdot \delta_{ij}$ is assumed for γ' , whereas a tetragonal mismatch of opposite signs for γ'' is found, namely in the case of a γ'/γ'' co-precipitate (in the global coordinate system, see Fig. 4.1):

$$e_{ij}^0 = 0.053 \cdot \delta_{1i} \delta_{1j} - 0.0061 \cdot (\delta_{2i} \delta_{2j} + \delta_{3i} \delta_{3j}) \quad (4.1)$$

and

$$e_{ij}^0 = 0.053 \cdot \delta_{3i} \delta_{3j} - 0.0061 \cdot (\delta_{1i} \delta_{1j} + \delta_{2i} \delta_{2j}) \quad (4.2)$$

for an individual γ'' particle. δ_{ij} is Kronecker's symbol.

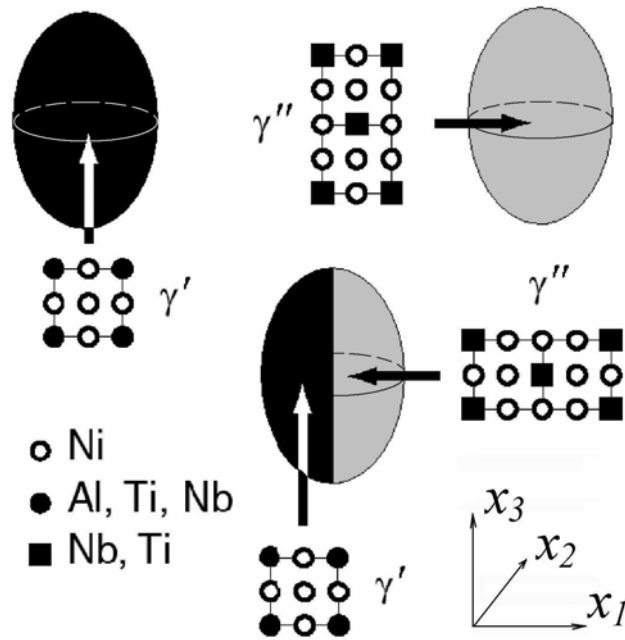


Fig. 4.1. Schematic representation of the morphology of the individual and co-precipitates. Black indicates the γ' phase, grey area the γ'' phase. The matrix is white. $x_1 // [100]_\gamma$, $x_2 // [010]_\gamma$ and $x_3 // [001]_\gamma$.

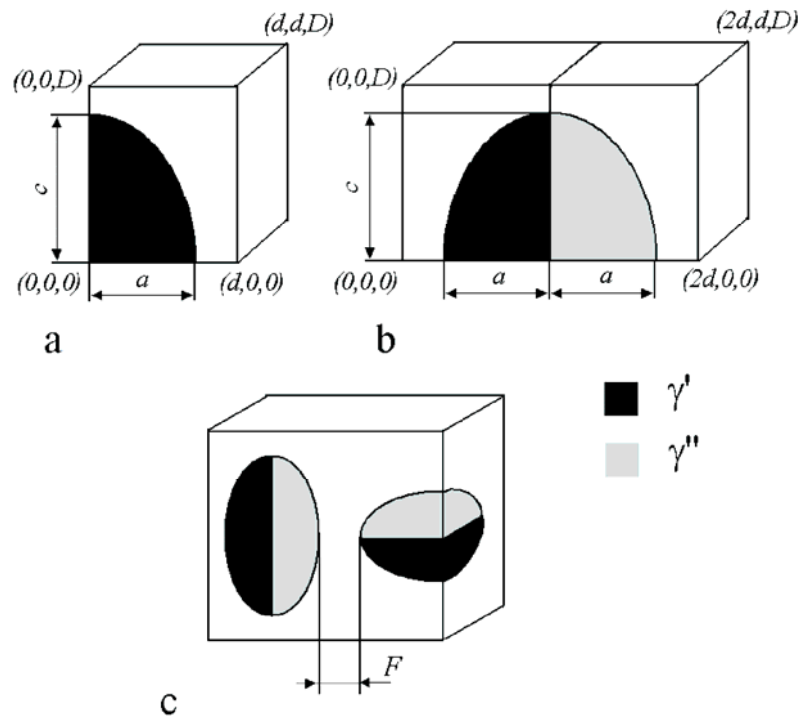


Fig. 4.2. Representative volumes to be analyzed for (a) individual precipitates, (b) co-precipitates and (c) two interacting precipitates. $a = 3.3$ nm, $c = 5$ nm, $d = 4.26$ nm, $D = 6.4$ nm and $F = 2.38$ nm.

After direct ageing the alloy is subjected to exposure to the service temperature of 750°C. Therefore, the elastic constants of the phases should be employed at this temperature. As the elastic constants of the matrix and of γ' and γ'' precipitates in Inconel 706 are not known, it is assumed for the simulation that the γ' phase is elastically stiffer than the γ matrix at temperatures about 750°C. This assumption is supported by experimental investigations [Siebörger 2001, Fahrman 1999]. The values of C_{ij} are listed in Table 4.1. Due to the similar crystal structures and chemical compositions of the γ' and the γ'' phases it is supposed that the elastic behavior of both phases are similar. Therefore, in the present study the elastic constants of the γ' phase are used for the γ'' phase.

The elastic constants for the cubic structure γ matrix and γ' phase can be expressed as follows:

$$[C]_i = \begin{bmatrix} C_{11} & C_{12} & C_{12} & 0 & 0 & 0 \\ C_{12} & C_{11} & C_{12} & 0 & 0 & 0 \\ C_{12} & C_{12} & C_{11} & 0 & 0 & 0 \\ 0 & 0 & 0 & C_{44} & 0 & 0 \\ 0 & 0 & 0 & 0 & C_{44} & 0 \\ 0 & 0 & 0 & 0 & 0 & C_{44} \end{bmatrix}$$

The same matrix is assumed for the γ'' phase, paying attention to the misfit effect only. The γ'' precipitates have a tetragonal crystal structure. In general, this kind of crystal has at least 6 independent elastic constants with additional C_{33} , C_{66} and C_{13} ($C_{23} = C_{13}$) in comparison to the cubic crystal system.

Table 4.1. The approximated elastic constants (in GPa) of the phases at 750°C. The ratio of anisotropy is $A = \frac{2C_{44}}{C_{11} - C_{12}}$.

	C_{11}	C_{12}	C_{44}	A
<i>Material</i>				
γ	170	110	90	3
γ'	200	140	100	3.(3)
γ''	200	140	100	3.(3)

The lattice mismatch was simulated by assuming a different thermal expansion behavior for each phase, see for example [Müller 1992, Chen 1999, Feng 1996]. The corresponding thermal expansion coefficients are

$$\begin{aligned}
\alpha_{ij}^{matrix} &= 0, \\
\alpha_{ij}^{\gamma'} &= -3.34 \cdot 10^{-3} \cdot K^{-1} \cdot \delta_{ij}, \\
\alpha_{ij}^{\gamma''} &= 5.43 \cdot 10^{-2} \cdot K^{-1} \cdot \delta_{1i} \delta_{1j} - 6.13 \cdot 10^{-3} \cdot K^{-1} \cdot (\delta_{2i} \delta_{2j} + \delta_{3i} \delta_{3j}), \text{ co-precipitate,} \\
\alpha_{ij}^{\gamma''} &= 5.43 \cdot 10^{-2} \cdot K^{-1} \cdot \delta_{3i} \delta_{3j} - 6.13 \cdot 10^{-3} \cdot K^{-1} \cdot (\delta_{1i} \delta_{1j} + \delta_{2i} \delta_{2j}), \text{ individual precipitate.}
\end{aligned}$$

Depending on the type of precipitate one should use different thermal expansion coefficients $\alpha_{ij}^{\gamma''}$ for the γ'' phase in the same global coordinate system (see Fig. 4.1). By applying a temperature increment of 1 K for all models one introduces the lattice mismatch (4.1) and (4.2) at the γ/γ' , γ/γ'' and also γ'/γ'' interfaces.

Due to the symmetry of the problem only $\frac{1}{8}$ of the individual precipitates and a quarter of the co-precipitates need to be analyzed.

Several assumptions are used for the FE model. Firstly, the coherent conjugation at the γ/γ' , γ/γ'' and γ'/γ'' boundaries was taken into account (see Fig 3.9). Secondly, absolutely sharp interfaces have been imposed. This is an approximation since in reality the γ/γ' and γ/γ'' boundaries are not perfectly sharp (the transition zone is about 1 nm thick). Moreover, there are Nb-enriched shells surrounding the individual γ' precipitates. The elastic properties of the phases are nonhomogeneous in real alloys, particularly in the vicinity of the mentioned phase boundaries.

4.3 Results of FE calculations

4.3.1 Mean normal stress and elastic strain energy distribution: case of individual γ' precipitate

The following boundary conditions are used for the constraints (Fig. 4.2a): $u_x(0, y, z) = 0$, $u_y(x, 0, z) = 0$, $u_z(x, y, 0) = 0$. The three cell boundaries at $x = y = d$ and $z = D$ are kept flat: $u_x(d, y, z) = const$, $u_y(x, d, z) = const$, $u_z(x, y, D) = const$. These boundary conditions mean that the box shown in Fig. 4.2a is the representative volume for the structure to be investigated. In other words, the microstructure investigated in this part consists exclusively of γ' precipitates oriented in the same direction, i.e. parallel to the $[001]_y$ direction of the matrix.

Fig. 4.3a shows the mean normal stress distribution as given by the FE model containing $\frac{1}{8}$ of the symmetry section of the ellipsoidal γ' particle. Within the precipitate the mean normal stress has a

tensile character. The highest stress value of about 400 MPa is attained in the upper part of the γ' ellipsoid. In the γ matrix a compressive mean normal stress is obtained. The largest compressive stress value of -200 MPa is found in all three $\langle 100 \rangle_\gamma$ directions. The elastic strain energy density is presented in Fig. 4.3b. The maximum elastic strain energy density is found at the γ/γ' interface where it is approximately 60 times larger than the average value over the γ' precipitate and the average value in the γ matrix. Elastic strain energy is quite uniform within the γ' precipitate. In the γ matrix, however, a concentration of elastic strain energy in both the $[100]_\gamma$ and $[010]_\gamma$ directions is observed (see Fig. 4.3b).

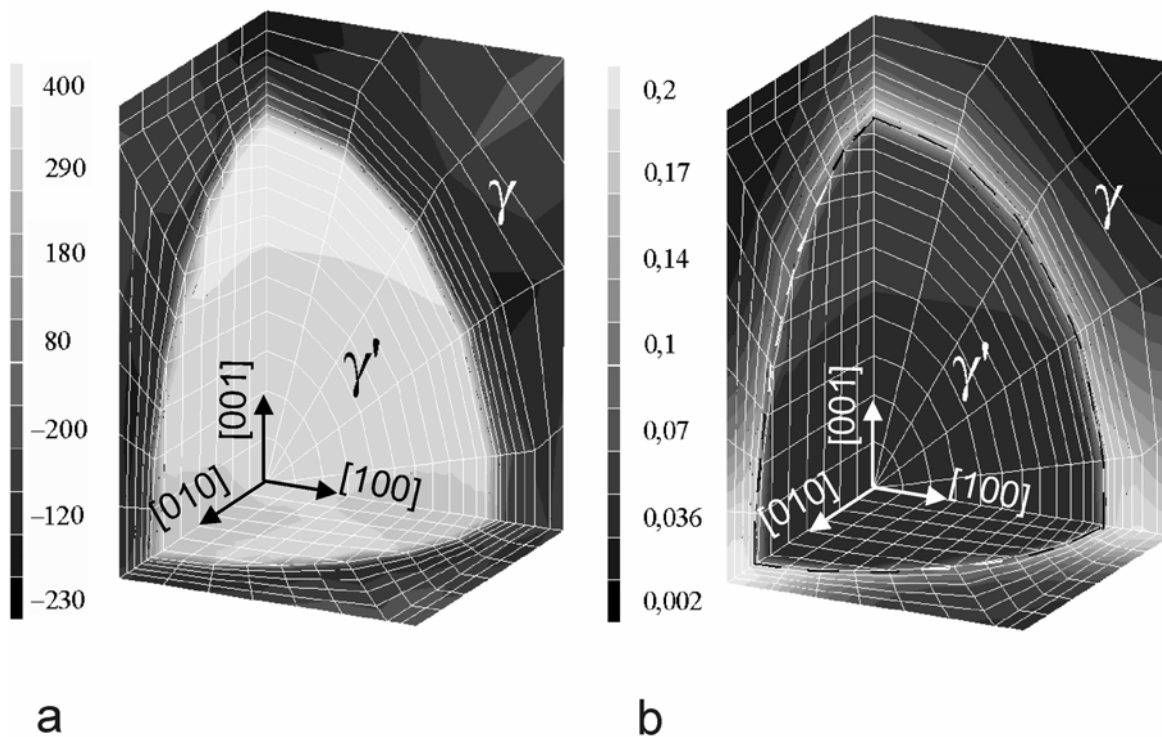


Fig. 4.3. The distribution of (a) mean normal stress (in MPa), and (b) elastic strain energy (in 10^7 J/m^3) in a γ' precipitate. The dashed curve denotes the γ'/γ boundary. The arrows in the picture indicate the crystallographic directions in the γ' phase which coincide with those of the γ matrix.

4.3.2 Mean normal stress and elastic strain energy distribution: case of individual γ'' precipitate

The same boundary conditions are applied as for γ' precipitates. The anisotropy of stress (energy density) arises from the precipitate geometry and the tetragonal structure of the γ'' phase. Individual γ'' precipitates are subjected to compressive mean normal stresses (see Fig. 4.4a) in contrast to γ' .

The highest stress values of -1800 MPa within the precipitate have been calculated in the $[001]_{\gamma''}$ direction. There is no change of stress character at the interface with the matrix. It changes to tensile only in the $[100]_{\gamma''}$ and $[010]_{\gamma''}$ directions. Strain energy density (see Fig. 4.4b) is comparable within the precipitate and at the γ/γ'' interface. The energy density is extremely low in the matrix, but there are still channels in the $\langle 100 \rangle_{\gamma}$ directions with increased energy storage (in average 5 – 10 times more than elsewhere in the matrix). Thus, the tetragonal misfit causes a strong stress and a strain energy anisotropy of the individual γ'' ellipsoid. There are three $\langle 100 \rangle_{\gamma}$ directions in which the elastic strain energy is especially large which may lead to precipitate instability in these directions.

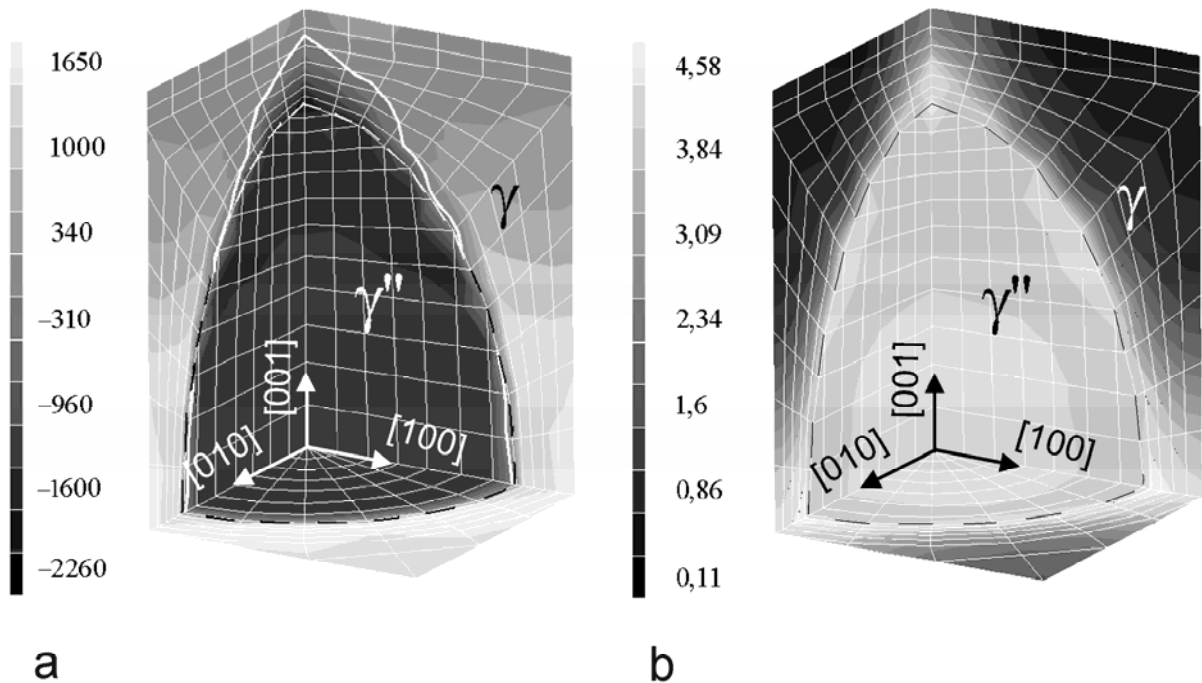


Fig. 4.4. The distribution of (a) mean normal stress (in MPa) and (b) elastic strain energy (in 10^7 J/m^3) within a γ'' precipitate. The white bold isolines denote vanishing stress, the dashed curve the γ''/γ boundary. The arrows in the picture indicate the crystallographic directions in the γ'' phase which coincide with those of the γ matrix.

4.3.3 Mean normal stress and elastic strain energy distribution: case of individual γ''/γ' precipitate

Considering the symmetry of the problem one performs the calculation for a quarter section of the ellipsoid as shown in Fig. 4.2b. Similar boundary conditions are employed as in the former case:

$u_x(0, y, z) = 0$, $u_y(x, 0, z) = 0$, $u_z(x, y, 0) = 0$. The other three boundaries at $x = 2d$, $y = d$ and $z = D$ remain flat: $u_x(2d, y, z) = const$, $u_y(x, d, z) = const$, $u_z(x, y, D) = const$. The microstructure investigated in this part consists of only γ'/γ'' co-precipitates oriented in the same direction, parallel to the $[001]_{\gamma}$ direction of the matrix.

One observes a complicated stress state inside and around the co-precipitate (Fig. 4.5a). The dashed curves denote the phase boundaries between the precipitate and the matrix. In order to study the internal γ'/γ'' interface, the calculated section is chosen according to Fig. 4.5. The white bold isolines show the transition between tensile and compressive stresses. The mean normal stress is tensile near the γ/γ' interface. The character of stress still remains the same when crossing the interface boundary, but it decreases within the precipitate. Compressive stresses appear beyond the isoline. Consequently, the γ'/γ'' interface as well as the entire γ'' phase are totally compressed. A negative stress value -1500 MPa is calculated in the $[001]_{\gamma''} // [100]_{\gamma}$ direction (on the matrix side of the external γ''/γ interface). The most significant stress changes occur in the same $[001]_{\gamma''}$ direction. The matrix becomes more strained around the γ'' part of the co-precipitate, at the same time stretched in the $[010]_{\gamma'}$ and $[001]_{\gamma'}$ directions. An analysis of energy density shows that the γ''/γ interface and particularly the matrix in the $[100]_{\gamma} // [001]_{\gamma''}$ direction are the regions with the most elevated elastic strain energy within the analyzed volume (Fig. 4.5b). The energy density is lower in the γ'' based semi-ellipsoid as compared to the individual γ'' precipitate and even decreases at the γ'/γ interface in comparison to the energy density at the γ'/γ interface of the individual γ' . Thus, the merger of two individual precipitates into a single γ'/γ'' co-precipitate reduces the elastic strain energy accumulated in a representative volume. This originates from stress relaxation by joining precipitates with different stress states (tensile in γ' and compressive in γ'' precipitate correspondingly).

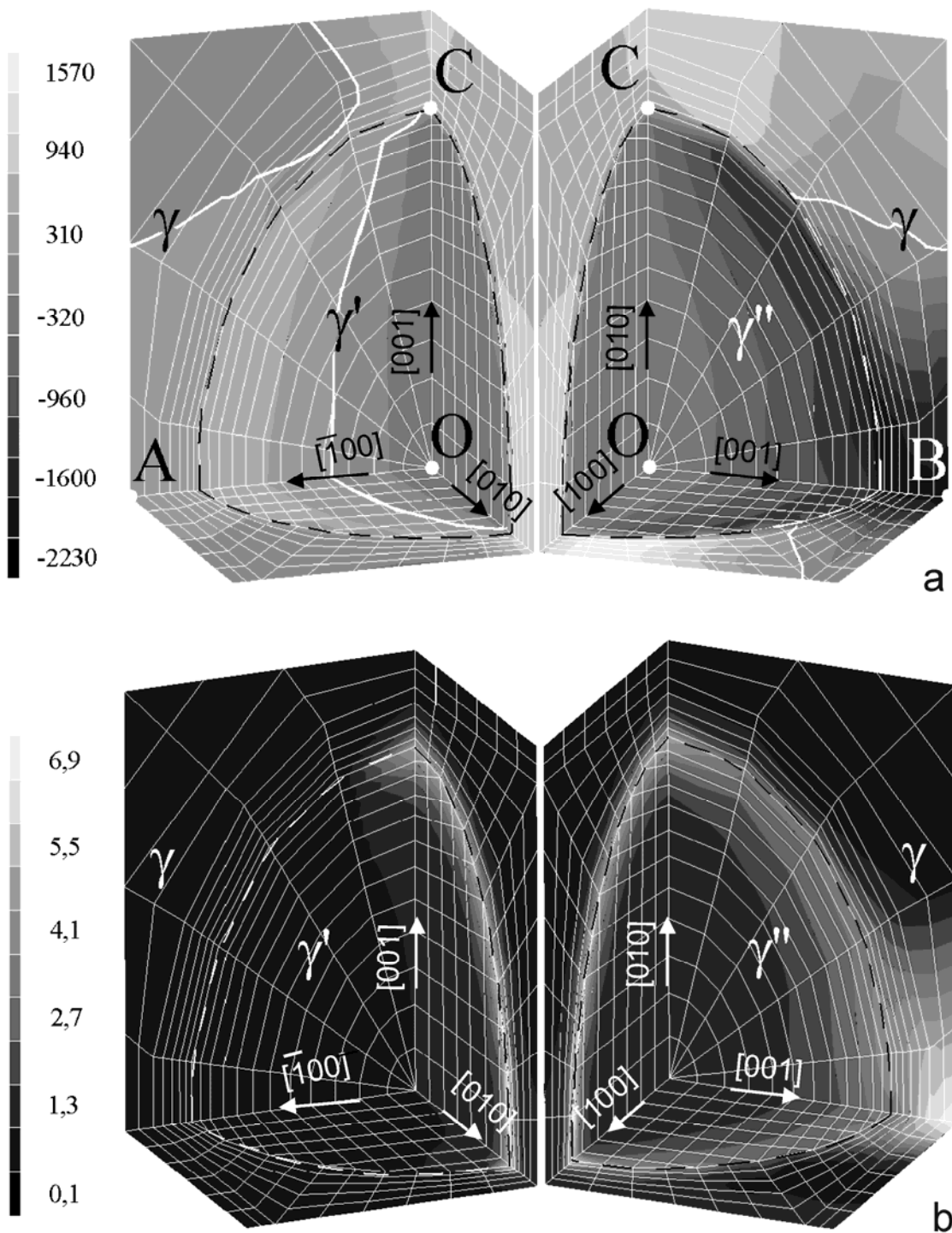


Fig. 4.5. The distribution of (a) mean normal stress (in MPa) and (b) elastic strain energy (in 10^7 J/m^3) in a γ'/γ'' co-precipitate. The white bold isolines signify vanishing stress. The dashed curves denote the γ'/γ boundary (on the left) and γ''/γ (on the right). The cross section lies along the γ'/γ'' interface. The arrows indicate the crystallographic directions in γ' (left) and γ'' (right) phases. The crystallographic directions in the γ matrix coincide with those of the γ' phase.

4.4 Coherency of interfaces

Let us assess the validity of the approximation made in the calculation concerning coherency of interfaces. One should estimate the lower limit for the critical size of the precipitates. It can be seen as the minimum size at which the particles can be kept coherent.

The criterion of Brooks for a spherical precipitate [Brooks 1952] gives a critical radius r_c as

$$r_c = \frac{b}{2\delta}, \quad (4.3)$$

where b is the Burgers vector module and δ is the dilatational misfit. The critical sizes of the ellipsoid can then be recalculated using the curvature of the ellipsoid in the “C” and “B” points (Fig. 4.5a). Hence one obtains for the critical parameters $c_c = \frac{9}{4}r_c$ and $a_c = \frac{4}{9}r_c$. $c \leq c_c$ and $a \leq a_c$ are two independent criteria. Therefore, the ratio c_c/a_c must not be equal to the aspect ratio, i.e. 1.5, as in the present model. The calculation of the critical radius is made in points “C” and “B” to find c_c and a_c , respectively. With this purpose the tangential misfit components are used which are introduced in (4.1) or (4.2) instead of δ in (4.3). It is sufficient to calculate just a_c for the individual γ' precipitate because the γ' phase has a dilatational mismatch to the matrix. The results are listed in Table 4.2. The experimentally observed values of semi-minor and semi-major axes lie between 3.3 – 5 and 5 –

Table 4.2. The lower estimate for the critical sizes of the precipitates.

<i>Precipitate</i>	interface	a_c , nm	c_c , nm
γ'	γ/γ'	17	-
γ''	γ/γ''	1	46.5
	γ/γ'	17	-
γ'/γ''	γ/γ''	9.2	5.4
	γ'/γ''	9.4 ¹	-

7.5 nm, so there is reason to believe that the γ' and the γ'/γ'' particles are coherent. However, the appearance of dislocations near the equator of the individual γ'' precipitate is possible, especially in the $[100]_{\gamma''}$ and $[010]_{\gamma''}$ directions (see Fig. 4.4). However, the interaction between the precipitates

¹ The internal γ'/γ'' boundary within the co-precipitate is plane, this was taken into account according to [Merwe 1963].

occurs by decreasing the magnitude of stresses. Moreover, the interfaces of the precipitates are not ideally sharp. Therefore, the values of the critical parameters which are listed in the table are underestimated.

An effective medium approach can be applied if the dislocation density is low. In this case the first term in (4.2) has to be replaced by an effective misfit taking into account the dislocation and the interaction energy (i.e. the energy released by the formation of the dislocation).

Thus, summarizing the approximations and the results of the present calculations it should be noted that the elastic strain energy being produced per precipitate as well as the stress values are lower in reality. However, the results of the FE calculations remain valid in a qualitative sense including the predictions on morphology evolution.

5 Discussion

In the present thesis the microstructure development and partitioning of alloying elements were investigated in the Inconel 706 superalloy after DA and MST heat treatments and after ageing at 750°C for different ageing times. The superalloy was modified in order to improve its performance in operation. The investigated modifications of the Inconel 706 superalloy include the Re-containing Inconel 706 superalloy and the DT 706 superalloy. The Re-alloyed Inconel 706 contains 0.69 at.% (2.23 wt.%) of Re. The DT 706 superalloy differs from the pure Inconel 706 alloy in the content of Ti, Al, Ni and Fe. The results of the investigations are discussed below. The aim of the present thesis is to know the microstructure in detail and the microstructure development under service conditions, to analyze the chemical composition of the phases, to understand the morphology development of the precipitates and at least to investigate the influence of Re and of alloying elements on the microstructure stability.

5.1 Inconel 706 and its Re-containing modification

5.1.1 Microstructure before and after heat treatment

The examination whether the alloying elements are homogeneously distributed in the specimens after solution heat treatments at 980°C for 3 h and for 10 h was checked at first by the statistical WDF analysis of the 3DAP results. It shows that Al is homogeneously distributed, independent of the duration of solution heat treatment (Fig. 3.3). Aluminum is a γ' former, so there are no fluctuations of concentrations which could induce the nucleation of γ' precipitates directly after solution heat treatment. Nb shows a heterogeneous distribution after 3 h and after 10 h of solution heat treatment (Fig. 3.3). These principal wavelengths of the Nb distribution after 3 h are 10 nm and 130 nm, whereas after 10 h it is larger than 212 nm. However, it is clear that the number of regions with increased concentration of Nb (beyond the bounds of statistical oscillation) rapidly decreases as the time of solution treatment increases up to 10 h. Such regions could be the potential places to nucleate γ'' precipitates. Additionally, the nucleation of γ' or γ'' precipitates requires non-statistical fluctuations of Ni. This is not the case for the specimens solution heat treated for 10 h. If the duration of solution heat treatment is only 3 h a heterogeneous distribution of both Ni and Nb occurs. Therefore, the nucleation of γ'' precipitates seems to be more probable during MST heat treatment which includes solution

treatment for 3 h than during the MST with 10 h solution heat treatment. The statistically treated results of the 3DAP analysis show the development of inhomogeneity of distinct wavelength.

The measurements of dislocation density (see 3.1.1) show an expected result: after solution heat treatment for 10 h the number of dislocations is two times smaller than that after 3 h heat treatment. The dislocations can act as heterogeneous sites for nucleation of precipitates [Cahn 1957, Christian 1965]. Therefore, the intragranular precipitation in Inconel 706 is favorable also due to the higher dislocation density if solution treatment lasts only 3 h.

The microstructure of Inconel 706 after MST heat treatment is presented in section 3.1.3. A bimodal distribution of precipitates was observed: fine γ' precipitates and γ'/γ'' or $\gamma''/\gamma'/\gamma''$ co-precipitates (15 – 20 nm) and larger γ'' needles (about 50 – 100 nm). However, γ'' needles do not exist in the MST sample if the corresponding solution heat treatment lasts 10 h [Del Genovese 2005]. It is supposed, that the nucleation of intermetallic phases in the MST sample observed here after 3 h solution treatment can be explained by the heterogeneous distribution of Ni and Nb and by the higher dislocation density than already mentioned above.

The microstructure of Inconel 706 after DA contains fine γ' , γ'' precipitates and γ'/γ'' co-precipitates (10 – 15 nm). In contrast to the MST sample the larger γ'' needles were not found. However, the main difference between the microstructures after DA and MST is the precipitation of η plates at the grain boundaries in the MST samples (compare Fig. 3.4 and Fig. 3.7). The grain boundaries in the DA samples are free of η precipitates. The reason for the formation of η precipitates is the stabilization stage at 820°C for 10 h after solution heat treatment. 820°C is above the temperature below the γ' and γ'' phases can exist [Shibata 1996a]. Thus the precipitation of the η phase at the grain boundaries is favored. The precipitation of the η phase improves the high stress rupture properties of Inconel 706 heat treated under MST conditions [Härkegard 1997].

The composition of the matrix between the precipitates is very similar in the DA and MST samples (see Table 3.1). The composition of the γ' and γ'' phases measured after DA is similar to that measured after the MST heat treatment. The difference is only that the content of Nb of the γ'' phase in the co-precipitates is about 4 at.% higher (see Fig. 3.10a) for the MST samples as compared with the value measured in the co-precipitates for the DA sample.

The MST samples were investigated after ageing at 750°C because of their good resistance against creep crack propagation in contrast to the DA samples. Coarsening of precipitates (see Fig. 3.12) occurs during ageing at 750°C for 750 h (further MST750). The γ' phase forms cubic precipitates about 60 nm large whereas the γ'' phase forms discs, which are about 300 nm in diameter. The η phase

nucleates and grows not only intergranularly but intragranularly as well, forming large plate-like precipitates (tens of microns).

The compositions of the γ' and of γ'' phases in the MST750 sample are close to the corresponding compositions of these phases in the MST sample. A small increase of Ti (about 2 at.% was measured in the γ' phase after ageing for 750 h. An increase in Ti leads to an increase of the lattice parameter of the γ' phase [Mishima 1985]. A decrease of Fe content in the matrix leads to a decrease of the lattice parameter of the γ matrix. Therefore, an increase of lattice misfit in the MST sample between the γ' phase and the matrix after ageing for 750 h is assumed .

Further ageing of the MST samples at 750°C up to 5000 h (further MST5000) leads to the full dissolution of the γ' and γ'' phases and only plate-like η precipitates remain in the microstructure of the superalloy (see Fig. 3.14). After ageing for 750 h or 5000 h the matrix of the MST samples contains 4 at.% less Fe (which is replaced by Cr). This is in accordance with the high content of Fe in the η phase formed during ageing. Ageing for 5000 h leads to the highest content of Ni in the matrix, 3–4 at.% more as compared with the values measured in the DA, MST and MST750 samples. This is explained by the increase in volume fraction of the matrix from 86 % as calculated for the MST samples to 93 % as calculated for the MST5000.

The measurement of the η phase by 3DAP was carried out in the MST5000 sample, as listed in Table 3.3. The composition of the η phase in the MST5000 sample is similar to that measured by EDX in the MST750 sample (see Table 3.2).

The result of the heat treatment at 750°C for 5000 h is that precipitation strengthening (represented by micro-hardness measurements see Fig. 5.1) of Inconel 706 by the intermetallic γ' and γ'' phases is completely lost. Therefore, 0.69 at.% (2.23 wt.%) of Re was added, in order to reduce the coarsening rates of the γ' and γ'' precipitates at the service temperatures 700 – 750°C [Giamei 1985].

The microstructure of the Re-containing MST sample is not considerable altered when compared to that in the pure MST sample. The morphology of the fine γ' , γ'' precipitates and γ'/γ'' co-precipitates is seen in Fig's. 3.17, 3.18, 3.20 – 3.23. The depth profiles shown in Fig. 3.19 taken through the precipitates illustrate an increase of Ni content by about 10 at.% within the co-precipitate close to external γ/γ' , γ/γ'' interfaces and close to internal γ'/γ'' interface (see both Fig. 3.19a and Fig. 3.19b). Ni has a smaller atomic radius than Nb and Ti. Therefore, Ni-enriched regions within the co-precipitates are expected to be under compressive stress. Thus, the diffusion of Nb and Ti atoms through Ni-enriched regions is difficult. These areas of external interfaces are oriented parallel to the internal γ'/γ'' boundary (or perpendicular to the $[001]_{\gamma''}$ direction). Since Nb and Ti are precipitate formers

further coarsening of co-precipitates seems to be easier perpendicular to the $[001]_{\gamma''}$ direction, i.e. along the γ'/γ'' boundary. This conclusion is in agreement with the morphology of the co-precipitates being observed in Fig. 3.18.

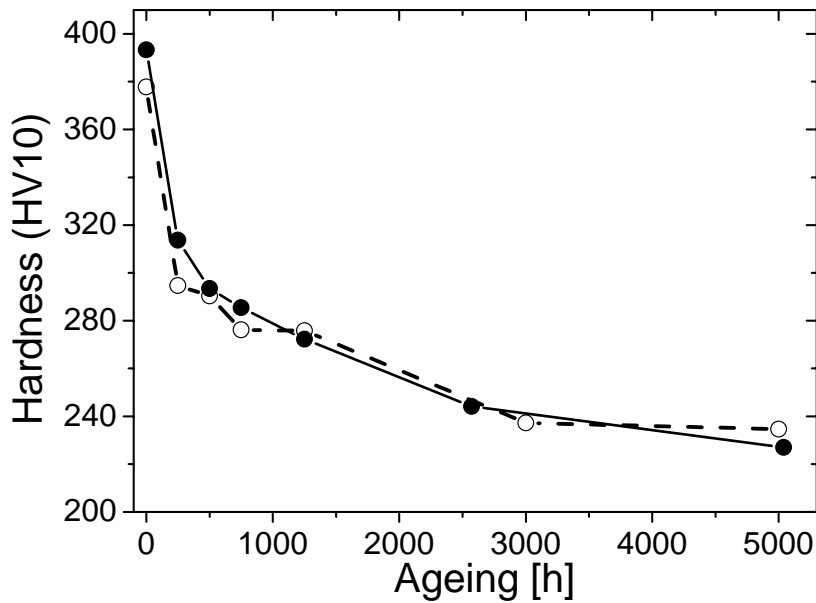


Fig. 5.1. Micro-hardness evolution of pure (open circles) and Re-containing (filled circles) Inconel 706 superalloys heat treated under MST conditions as a function of the ageing time at 750°C.

The lattice misfit between the γ' phase and the matrix in Inconel 706 is negative [Mukherji 2003]. The γ' phase of the Re-containing MST sample contains 4 – 5 at.% less Ti (compare Tables 3.4 and 3.1) when compared to that in the pure MST sample. This leads to a decrease of the lattice mismatch between the γ' phase and the matrix. A negative lattice misfit parameter caused by the addition of Re in the superalloys was already observed by [Murakami 1994, Blavette 1988, MacLachlan 2001, Schulze 2000]. Whether the addition of Re influences the composition of the γ' precipitates was not yet known.

Ageing of the Re-containing Inconel 706 superalloy also leads to coarsening of the fine precipitates and co-precipitates and to the nucleation and growth of the η phase (see Fig 3.24). Fig. 5.2 shows the microstructure of the Re-containing MST samples aged at 750°C for 5000 h. The strengthening γ' and γ'' precipitates and γ'/γ'' co-precipitates are dissolved. The microscopically observed phases are correlated to the macroscopic mechanical properties. As a measure of the macroscopic mechanical properties the micro-hardness for both pure and Re-containing Inconel 706 alloys after ageing at 750°C for different times is plotted in Fig. 5.1. As can be seen there is no significant effect of Re on hardness. Indeed, the addition of Re increases the hardness value of the alloy only in the initial stage (MST

condition) without further ageing because of mixed crystal hardening of the matrix. A rising hardness with higher concentrations of Re was also shown for different nickel-based CMSX superalloy [Durst 2004]. Unfortunately, Re does not stabilize the microstructure of Inconel 706, as was expected at the beginning of the present investigation. The reason may be that Re does not form “bow-waves” [Warren 1998] ahead of the growing γ' , γ'' precipitates and γ'/γ'' co-precipitates either in the MST or in the MST750 samples (see depth profiles in Fig's. 3.19 – 3.22 and in Fig. 3.30). Such “bow waves” were detected in the superalloy RR3000 [Warren 1998]. Formation of “bow-waves” at the γ' interface or clusters in the matrix [Wanderka 1995] were observed in the alloys with a small volume fraction of the matrix (less than 30 %) which is much lower than in our case (86 %). However, in the present investigation no Re-rich clusters were observed in the matrix. An increase in Re in the alloy is not expected to give the effect because Re solubility in Inconel 706 is very low. A high amount of Re will lead to the formation of undesired Re-rich precipitates.

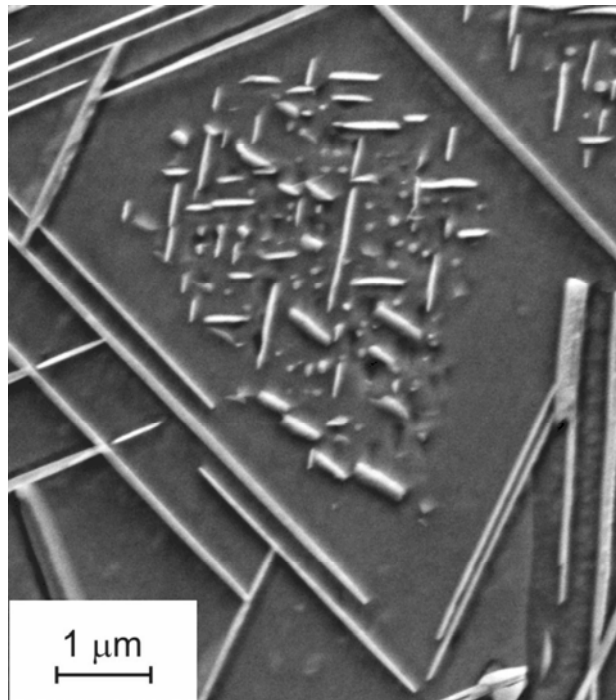


Fig. 5.2. SEM micrograph of the microstructure of the Re-containing MST samples aged at 750°C for 5000 h. The η precipitates are seen intragranularly.

5.1.2 FEM analysis

Whether the co-precipitation takes place is determined by the sum of interface energy and elastic strain energy. In the present FEM study all interfaces between individual phases in Inconel 706 are assumed to be coherent. Negligibly small interface energies are expected for all three coherent phase boundaries γ/γ' , γ/γ'' and γ'/γ'' . The occurrence of γ'/γ'' co-precipitation depends, therefore, on elastic strain

energies induced by the lattice mismatch. The morphology development of precipitates during phase transformation tends to minimize elastic strain energy. In the present investigation elastic strain energies for γ' and γ'' precipitates as well as for γ'/γ'' co-precipitates have been calculated. The total strain energy per γ'' precipitate is $1.7 \cdot 10^{-17}$ J, while the total strain energy per γ'/γ'' precipitate merely is $5.64 \cdot 10^{-18}$ J. In order to form a γ' -based precipitate a minimum energy of $4 \cdot 10^{-19}$ J is necessary. In comparison with the precipitation of individual γ'' precipitates, γ'/γ'' co-precipitation is energetically more favorable and is, therefore, predominant during ageing. Co-precipitates are “non-compact”. One still open question is why the entire γ'' phase does not exist in the form of co-precipitates? The present simulation shows the preferential ways of morphological evolution.

Coarsening of co-precipitates can be discussed in more detail by using stress depth profiles. The direction $[100]_{\gamma'} // [001]_{\gamma''}$ is selected since stress gradients are negligible in other directions (see Fig. 4.5a). The AOB line was taken since much energy is concentrated here (Fig. 4.5b). The stress and energy distributions of individual γ' and γ'' precipitates and also of γ'/γ'' co-precipitates are plotted in Fig. 5.3. The profiles for individual precipitates are quite symmetric to the center of the precipitate, which is denoted by the broken line at 4.26 nm.

The elastic energy density inside a co-precipitate is always lower than that inside the γ'' precipitate (Fig. 5.3b), but they are nearly equal at both sites of the external γ''/γ interface. The elastic energy density of γ'/γ'' co-precipitates approaches the values for γ'' at the γ''/γ interface and the values for γ' at the γ/γ' interface. Here, the matrix accumulates less energy as compared with individual γ' precipitates. Co-precipitates are more stable compared to γ'' precipitates, although they still possess a high-energy accumulation area.

The mean normal stress gradients (Fig. 5.3a) in the high-energy accumulation region (the vicinity of point “B”, in Fig. 4.5a) are of great importance as they cause stress-induced atom diffusion. The compressive stress near the γ''/γ interface is larger than that within the co-precipitate. This leads to a larger decrease of lattice parameters near the boundary. Thus, some of the atoms with larger atomic radii such as Nb, Ti and Al (which are precipitate formers) will diffuse preferably towards the γ'/γ'' interface. This means that diffusion is more favorable in the $(001)_{\gamma''}$ planes of the γ'' phase in the co-precipitate, whereas the γ''/γ interface can not be moved. In this way the γ'' semi-ellipsoids transform into discs oriented normal to the $[001]_{\gamma''}$ direction.

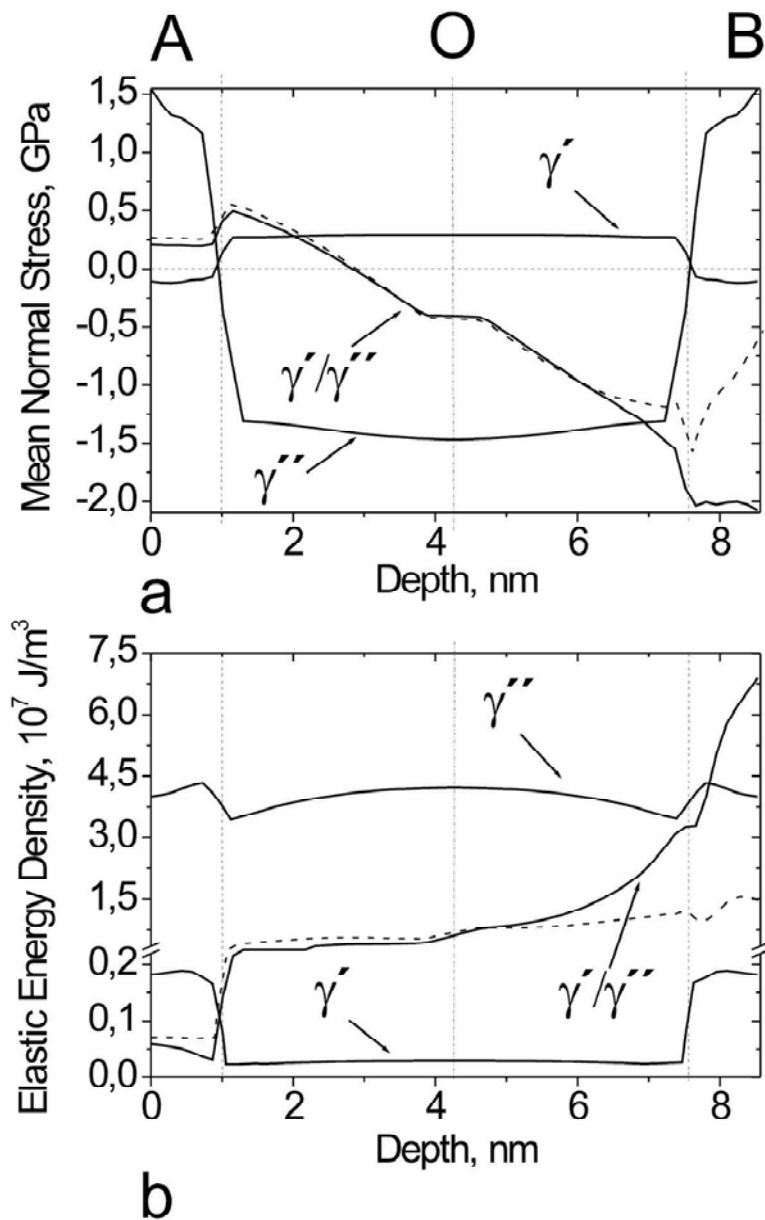


Fig. 5.3. Distributions of (a) mean normal stress and (b) elastic strain energy density across the precipitate along the path AOB (see Fig. 4.5a). The vertical broken lines indicate phase interfaces. The line at 4.26 nm denotes the γ'/γ'' phase boundary which should be neglected for the individual precipitates. The other two lines at 0.98 nm and 7.54 nm show the position of external boundaries with the matrix. The dotted lines reveal the effect of interactions between two co-precipitates.

The same approach can be employed for the γ' part of the co-precipitate. This part is not exposed to such high stress gradients and should behave similar in all $\langle 100 \rangle_{\gamma'}$ directions. Nevertheless, forming of a new γ'' surface may make coarsening of a γ' phase to be slightly advantageous perpendicular to the $[001]_{\gamma''}$ direction in order to partly cover the newly produced free surface. As a result, γ'' plates with an attached γ' phase appear. This is consistent with the experimental observations [Baranski 2003] in

which the alloy structure has been studied after 750 h of ageing at 750°C. The volume of completely developed γ' and γ'' phases depends on chemical free energy reduction and cannot be discussed in terms of strain energy. This assumption can only be used for developing precipitates.

The energies and stresses calculated here can not be apply for a long-range stress field. It is not possible to apply the present model which regards single precipitates for a microstructure with a long-ranging stress field. A representative volume containing several co-precipitates cannot be correctly constructed because of a multiphase precipitate nature. However, it is clear that the highest energy reduction occurs when the “C” and “B” poles of two co-precipitates begin to interact (as shown in Fig. 4.2c). This alters the energy and stress depth profiles of a co-precipitate as shown by the dotted lines in Fig. 5.3. The energy density deviates from that of the co-precipitate alone. In particular the energy density is lowered in the vicinity of the γ''/γ boundary. The co-precipitate undergoes an energy levelling along the AOB line and weak stress relaxation in front of the γ''/γ interface (Fig. 5.3a). In the matrix strong stress gradients appear near this boundary which are oriented outwards. These gradients act as barriers for atoms with larger radii when they try to penetrate into the precipitate. In contrast, Cr and Fe, as matrix formers, diffuse towards the phase boundary. Hence, the growth of the precipitate in the $[001]_{\gamma''}$ direction becomes less favorable owing to the interaction between two co-precipitates. This explains the tendency for the γ'' phase of the co-precipitate to grow into plates with $(001)_{\gamma''}$ habit planes.

5.2 DT 706 as a modified Inconel 706 superalloy

Another superalloy, namely DT 706, was also investigated to find out whether the small deviations in composition compared to pure Inconel 706 can stabilize the microstructure at 750°C. As was shown above, the main instability of the microstructure of Inconel 706 at 750°C is rapid coarsening of the γ'' phase and formation of the η phase intragranularly. The stabilization of the γ'/γ'' co-precipitates and γ'' precipitates is expected by an increase of the ratio Al+Ti to Nb [Gou 1994, Xie 1994] from 1.22 to 1.85 for pure Inconel 706 and for DT 706, respectively.

The microstructure of the DT 706 superalloy after the MST/DT heat treatment consists of primary co-precipitates and secondary γ' precipitates. The primary co-precipitates have a cubic γ' particle at the core covered with a mantle of γ'' . This morphology is referred to as “compact”. The size of the primary co-precipitates lies in the range of 40–60 nm. The secondary γ' precipitates have sizes up to 20 nm.

They are of spherical morphology. The secondary precipitates are well observed in the 3DAP reconstruction, see Fig. 3.34. Cozar and Pineau [Cozar 1973] suggested that the main factors for the formation of co-precipitates of “compact” morphology might be a ratio of Al+Ti to Nb higher than 0.9 and the initial size of γ' precipitates before the formation of the γ'' phase. The minimum initial size of the γ' precipitates was found to be about 20 nm [Cozar 1973]. The required condition (to achieve the “compact” morphology) concerning the minimum Al+Ti to Nb ratio is satisfied in both superalloys, the Inconel 706 and the DT 706. However, co-precipitates of the “compact” morphology do not form in Inconel 706 unlike in DT 706. This means that individual γ' precipitates larger than 20 nm (according to Cozar) form in DT 706 during stabilization heat treatment at 835°C for 10 h (see the definition of MST/DT heat treatment in Chapter 2). The phase interfaces of these precipitates may serve as the places of heterogeneous nucleation of the γ'' phase during final ageing at 720°C for 8 h, so, that the “compact” morphology develops in this way.

MST/DT heat treatment also produces plate-like η precipitates, mainly at grain boundaries, as in Inconel 706 superalloy heat treated under **MST** conditions (see Fig. 3.33).

The composition of the γ' phase is similar in the primary and secondary precipitates within the uncertainties (see Table 3.6). It contains about 5 at.% more Al and correspondingly less Ti as compared with the composition of the γ' phase in pure Inconel 706. Thus, the lattice parameter of the γ' phase should be smaller in DT 706 than compared with pure Inconel 706 [Mishima 1985].

Coarsening of the co-precipitates in the MST/DT sample was also observed after ageing at 750°C for 750 h. The co-precipitates achieve sizes up to 100 nm. However not all the faces of cubic γ' co-precipitates are covered with mantles of the γ'' phase. The co-precipitates have lose their “compact” morphology. It should be noted that the γ' phase contains less Al and correspondingly more Nb (about 2 at.%) after ageing than before.

A γ'' slice was reconstructed by means of 3DAP, see Fig. 3.36. The region close to the γ'/γ'' interface is enriched in Nb and depleted from Ti. We suggest that the dissolution of the γ'' phase probably occurs by diffusion of Nb along the γ'/γ'' interface.

Intragranular precipitation of the η phase takes place in the MST/DT sample during ageing at 750°C for 750 h, similar to that in Inconel 706. The η precipitates of the DT 706 superalloy contain 3 at.% more Al as compared with that of Inconel 706. This can be explained by the higher amount of Al in DT 706 when compared to the pure Inconel 706. We suggest that the larger content of Al in the γ' phase stabilize this phase.

The individual γ' precipitates have grown up to 150 nm in size after ageing at 750°C for 5000 h. The γ'' phase was not detected. The η precipitates are observed at grain boundaries and in grain interiors as well. The conclusion from this investigation is that DT 706 has an advantage compared with Inconel 706 because the matrix of DT 706 is γ' precipitation-strengthened even after ageing at 750°C for 5000 h.

6 Summary

In the present thesis the Ni-Fe-base Inconel 706 superalloy was investigated. The alloy is used as disc material owing to its good stability at temperatures up to 600°C. The good mechanical properties are due to precipitation strengthening by γ' and γ'' intermetallic phases. However, the alloy had been modified in order to be used at higher service temperatures, i.e. above 700°C. Two modified alloys, namely Re-containing Inconel 706 and DT 706 are investigated in this work. The latter differs mainly in its content of Nb, Al and Ti from the pure Inconel 706 superalloy. The development of the microstructure of the pure and modified alloys is investigated after ageing at 750°C for 750 and 5000 h.

The microstructure and the development of different phases and their morphology was analyzed by transmission electron microscopy (TEM) and three dimensional atom probe (3DAP). Furthermore, finite element (FE) calculations were applied to understand the development of distinct precipitation morphologies.

The 3DAP results, treated by the statistical wave depending filtering (WDF) analysis indicate heterogeneous distributions of Ni and Nb in the specimens of pure Inconel 706 which are solution treated at 980°C for 3 h. Specimens solution heat treated at 980°C but for 10 h have a distinct heterogeneous distribution of Nb.

Solution heat treatment at 980°C for only 3 h seems to be most advantageous for the precipitation strengthening of Inconel 706.

The microstructure of Inconel 706 depends strongly on the age-hardening treatment. Both direct ageing (DA) and modified stabilization heat treatment (MST) of Inconel 706 produce individual γ' and γ'' precipitates and γ'/γ'' co-precipitates. MST heat treatment produces also η precipitates which form at grain boundaries. After DA precipitates, with an average size of about 10 nm, are generally smaller than after MST with an average size of about 20 nm. Additionally, much bigger individual γ'' precipitates with sizes above 50 nm were also observed. They are semi-coherent with the matrix. All the precipitates are oriented parallel to the $\langle 001 \rangle$ lattice directions of the γ matrix.

The chemical composition of individual γ' precipitates does not essentially differ from that of co-precipitates. γ'/γ'' interfaces are very sharp, with a width of about one atomic layer, in contrast to γ/γ' and γ'/γ'' interfaces which are about 1 nm thick. The composition of the matrix was found to be

similar, independent of the heat treatment used. The estimated volume fraction of the γ matrix after MST heat treatment is about 86 %.

Small Nb-shells around γ' precipitates were detected after DA. The concentration of Nb within these shells amounts to 18 at.%. It is suggested that the shells may serve as origins for the heterogeneous formation of the γ'' phase.

During ageing at 750°C for 750 h nucleation and growth of the η phase occurs not only intergranularly, but intragranularly as well. The γ' phase forms cubic precipitates with sizes about 60 nm whereas the γ'' phase forms discs, which are approximately 300 nm in diameter. Further ageing of the MST samples at 750°C up to 5000 h leads to the full dissolution of the γ' and γ'' phases and only plate-like η precipitates (with sizes about 5–10 microns) remain in the microstructure of the superalloy.

Thus, the precipitation strengthening of the Inconel 706 superalloy by the intermetallic γ' and γ'' phases becomes completely lost after ageing for 5000 h.

The distribution of the elastic strain energy and hydrostatic stress was calculated by the finite element method in the microstructure of Inconel 706 heat treated under DA conditions. The highest energy density was found in the regions surrounding γ'/γ and γ''/γ interfaces. Co-precipitates γ'/γ'' develop together from the individual precipitates because this is energetically favorable with respect to the reduction of the elastic energy in individual γ'' precipitates. In this way the total surface of γ'/γ and γ''/γ interface decreases and energetically free γ'/γ'' interfaces appear.

The coarsening of precipitates was considered in the view of the hydrostatic stress distribution. The stress gradients show a tendency to grow of γ'' particles with a tetragonal misfit strain into plates oriented perpendicularly to the longer mismatch dimension.

Thus, using FEM simulations it is possible to predict the morphology development of the precipitates.

The modified Re-containing Inconel 706 has a similar microstructure after MST heat treatment as the pure Inconel 706 alloy. Individual γ' , γ'' precipitates and γ'/γ'' co-precipitates are good observable in the austenitic γ matrix. Re concentrates only in the matrix, practically being absent in the intermetallic phases. Unfortunately, Re does not form “bow-waves” (Re enriched zones) in front of the γ'/γ'' interface of the growing precipitates and co-precipitates. So, there are no barriers for the precipitate coarsening. After ageing for 5000 h, the microstructure of Re-alloyed Inconel 706 is similar to that of the pure alloy: there are only η plates (with sizes of about 1 – 10 microns) embedded

into the matrix. The pure and Re-containing Inconel 706 have similar hardness as a function of the ageing duration at 750°C.

The modification of the Inconel 706 superalloy by Re-addition seems to be ineffective to stabilize the material during service at elevated temperatures.

DT 706 heat treated under MST conditions shows bimodal distribution of the precipitates. All six faces of the larger γ' precipitates of cubic-like morphology (approximately 50 nm in size) are coated by γ'' shells, i.e. they are of so called “compact” morphology. The smaller individual γ' precipitates have sizes of about 20 nm and are of spherical morphology. The γ' phase contains about 5 at.% more Al and correspondingly less Ti as compared with the composition of the γ' phase in the pure Inconel 706 superalloy. During ageing at 750°C for 750 h coarsening of the co-precipitates occurs. Moreover, the co-precipitates lose their “compact” morphology, since not any more all six faces of the γ' precipitates are covered with a shell of the γ'' phase. After treatment under model service conditions at 750°C for 5000 h individual γ' precipitates with sizes of about 150 nm were detected. The γ'' phase was not more observed. The η precipitates are present at grain boundaries and in grain interiors as well.

Therefore, DT 706 has an advantage over the Inconel 706 superalloy because DT 706 remains γ' precipitation-strengthened even after service at 750°C for 5000 h.

References

- [Baranski 2003] T. Baranski, Studienarbeit, Technische Universität Braunschweig, 2003, p. 99.
- [Berger 2001] C. Berger, J. Granacher and A. Thoma, Superalloys 718, 625, 706 and Various Derivatives, TMS, Warrendale, PA (2001) 489.
- [Bethge 1987] H. Bethge, Electron Microscopy in Solid State Physics, Elsevier, New York (1987).
- [Blavette 1986] D. Blavette, P. Caron and T. Khan, Scripta Metall. **20** (1986) 1395.
- [Blavette 1988] D. Blavette, P. Caron and T. Khan, Proceedings "Superalloys 1988", The metallurgical Society, Warrendale, PA (1988) 305.
- [Blavette 1993] D. Blavette, A. Bostel, J. Sarrau, B. Deconihout and A. Menand, Nature **363** (1993) 432.
- [Blavette 1996] D. Blavette, P. Duval and M. Guttman, Acta Mater. **44** (1996) 4995.
- [Bostel 1989] A. Bostel, D. Blavette, A. Menand and J. Sarrau, J. de Physique **50-C8** (1989) 501.
- [Brooks 1952] H. Brooks, in: Metal Interfaces, American Society for Metals, Cleveland (1952) 20.
- [Cahn 1957] J. Cahn, Acta Metall. **5** (1957) 169.
- [Cerezo 1988] A. Cerezo, T. Godfray and G. Smith, Rev. Sci. Instrum. **59** (1988) 862.
- [Chen 1999] C. R. Chen, S. X. Li and Q. Zhang, Mater. Sci. & Eng. A. **272** (1999) 398.
- [Christian 1965] J. Christian, The Theory of Transformation in Metals and Alloys, Pergamon, New York (1965).
- [Clark 1967] B. Clark and F. Pickering, JISI **205** (1967) 70.
- [Clough 1960] R. Clough, American Society of Civil Engineers, Second Conference on Electronic Computation, Pittsburgh 1960.
- [Cliff 1975] G. Cliff and G.W. Lorimer, J. Microsc. **103** (1975) 203.
- [Collier 1988] J. Collier, A. Selious and J. Tien, Superalloys 1988, TMS, Warrendale, PA (1988) 43.
- [Cozar 1973] R. Cozar, A. Pineau, Metall. Trans. **4** (1973) 47.
- [Cozar 1991] R. Cozar, M. Rouby, B. Mayonobe and C. Morizot, Superalloys 718, 625 and Various Derivatives, TMS, Warrendale, PA (1991) 423.
- [Czubayko 2000] U. Czubayko, Y. Zhang, N. Wanderka, V. Naundorf and H. Wollenberger, Z. Metallkd. **91** (2000) 897.

- [Deconihout 1995] B. Deconihout, A. Bostel, M. Bouet, J. Sarrau, P. Bas and D. Blavette, *Appl. Surf. Sci.* **87/88** (1995) 428.
- [Del Genovese 2006] Del Genovese, Ph.D. Thesis, Technische Universität Braunschweig, to be published in 2006.
- [DFG 2002] DFG project, Untersuchung der Phasenumwandlungen und Korngrenzenchemie von Inconel 706 mittels 3D Atomsonde: Erarbeitung von Grundlagenkenntnissen und Ansätzen zur Werkstoffoptimierung Teilprojekt 2: Hochauflösende Analytik mittels 3-dimensionalen Atomsonde, under WA 1378/5-1 and WA 1378/5-2, (2002).
- [Drechsler 1960] M. Drechsler, D. Wolf, *Proceedings „International Congress for Electron Microscopy“* **4** (1960) 835.
- [Durst 2004] K. Durst, M. Göken, *Mater. Sci. & Eng. A.* **387/389** (2004) 312.
- [Edington 1976] J. Edington, *Interpretation of Transmission Electron Micrographs*, volume 3 of *Monographs in Practical Electron Microscopy in Materials Science*, Chap. III, p. 9, Philips Technical Library, Macmillan, London (1976).
- [Eiselstein 1970] H. Eiselstein, *Materials Engineering Congress*, Cleveland 1970.
- [Eiselstein 1991] H. Eiselstein, D. Tillack, *Superalloys 718, 625, 706 and Various Derivatives*, TMS, Warrendale, PA (1991) 1.
- [Fahrman 1999] M. Fahrman, W. Hermann, E. Fahrman, A. Boegli, T. Pollock and H. Sockel, *Mater. Sci. & Eng. A.* **260** (1999) 212.
- [Feng 1996] H. Feng, H. Biermann and H. Mughrabi, *Mater. Sci. & Eng. A.* **214** (1996) 1.
- [Gao 1995] M. Gao and R. Wei, *Scripta Metall. Mater.* **32** (1995) 987.
- [Giamei 1985] A. F. Giamei, D. L. Anton, *Metall. Trans. A.* **16A** (1985) 1997.
- [Gou 1994] E. Guo, F. Xu and E. Loria, *Superalloys 718, 625, 706 and Various Derivatives*, TMS, Warrendale, PA (1994) 721.
- [Härkegard 1997] G. Härkegard, W. Balbach, K. Stärk and J. Rösler, *Superalloys 718, 625, 706 and Various Derivatives*, TMS, Warrendale, PA (1997) 425.
- [Heck 1994] K. Heck, *Superalloys 718, 625, 706 and Various Derivatives*, TMS, Warrendale, PA (1994) 393.
- [Helms 1996] A. Helms, C. Adascyik, and L. Jackman, *Superalloys 1996*, TMS, Warrendale, PA (1996) 427.
- [Hirsch 1965] P. Hirsch, R. Nicholson, A. Howie, D. Pashley and M. Whelan, *Electron Microscopy of Thin Crystals*, Chap. XVII, p. 423, Butterworths, London (1965).
- [Hirsch 1965a] P. Hirsch, R. Nicholson, A. Howie, D. Pashley and M. Whelan, *Electron Microscopy of Thin Crystals*, Butterworths, London (1965).

- [Hutton 2004] D. Hutton, Fundamentals of Finite Element Analysis, McGraw-Hill, New York (2004).
- [Jong 1977] K. Jong, D. Barnett and H. Aaronson, Metall. Trans. A. **8A** (1977) 963.
- [Kang 1994] B. Kang, Superalloys 718, 625, 706 and Various Derivatives, TMS, Warrendale, PA (1994) 579.
- [Kellogg 1980] G. Kellogg and T. Tsong, J. Appl. Phys. **51** (1980) 1184.
- [Khachaturyan 1983] A. G. Khachaturyan, Theory of Structural Transformations in Solids, Chap. VII, VIII, X and XI, Wiley, New York (1983).
- [Kindrachuk 2004] V. Kindrachuk, N. Wanderka, J. Banhart, D. Muherji, D. Del Genovese and J. Rösler, Steel Research **75** (2004) 74.
- [Kuhlman 1994] G. Kuhlman, A. Chakrabarti, R. Beaumont, E. Seaton and J. Radavich, Superalloys 718, 625, 706 and Various Derivatives, TMS, Warrendale, PA (1994) 441.
- [Leisch 1994] M. Leisch, J. Anal. Chem. **349** (1994) 102.
- [MacLachlan 2001] D. W. MacLachlan, D. M. Knowles, Mater. Sci. & Eng. A. 302 (2001) 275.
- [Mannan 2000] S. Mannan, S. Patel and J. deBarbadillo, Superalloys 2000, TMS, Warrendale, PA (2000) 449.
- [Merrick 1962] H. Merrick and R. Nicholson, Proceedings „International Congress for Electron Microscopy“ **K** (1962) 8.
- [Merwe 1963] J. H. van der Merwe, J. Appl. Phys. **34**(1) (1963) 123.
- [Miller 1989] M.K. Miller, G.D.W. Smith, Atom Probe Microanalysis: Principles and Application to Materials Problems, Materials Research Society, Pittsburgh, PA (1989).
- [Miller 1996] M.K. Miller, A. Cerezo, M.G. Hetherington, G.D.W. Smith, Atom Probe Field Ion Microscopy, Oxford University Press, Oxford (1996).
- [Mishima 1985] Y. Mishima, S. Ochiai, T. Suzuki, Acta Metall. Mater. **33** (1985) 1161.
- [Moll 1971] J. Moll, G. Maniar and D. Muzyka, Metall. Trans. A. **2A** (1971) 2143.
- [Moll 1971a] J. Moll, G. Maniar and D. Muzyka, Metall. Trans. A. **2A** (1971) 2153.
- [Mukherji 2003] D. Mukherji, P. Strunz, D. Del Genovese, R. Gilles, J. Rösler and A. Wiedenmann, Metall. and Mater. Trans. A. **34A** (2003) 2781.
- [Mukherji 2003A] D. Mukherji, R. Gilles, B. Barbier, D. del. Genovesse, B. Hasse, P. Strunz, T. Wroblewski, H. Fuess and J. Rösler, Scripta Mater. **48** (2003) 333.
- [Müller 1960] E. Müller, Adv. Electron. Electron Phys. **13** (1960) 83.

- [Müller 1965] E. Müller, *Science* **149** (1965) 591.
- [Müller 1969] E. W. Müller, T. T. Tsong, *Field Ion Microscopy*, Elsevier, New York (1969).
- [Müller 1992] L. Müller, U. Glatzel and M. Feller-Kniepmeier, *Acta Metall. Mater.* **40**(6) (1992) 1321.
- [Murakami 1994] H. Murakami, H. Harada and H. Bhadeshia, *Appl. Surf. Sci.* **76/77** (1994) 177.
- [Nazmy 1997] M. Nazmy, M. Staubli and C. Nosedá, *Superalloys 718, 625, 706 and Various Derivatives*, TMS, Warrendale, PA (1997) 419.
- [Paulonis 1965] D. Paulonis, J. Oblakxand and D. Duvall, *Trans. ASM* **62** (1965) 611.
- [Reimer 1997] L. Reimer, *Transmission Electron Microscopy*, Springer-Verlag, Berlin (1997).
- [Remy 1979] L. Remy, J. Laniesse and H. Aubert, *Mater. Sci. & Eng.* **38** (1979) 227.
- [Rüsing 2002] J. Rüsing, N. Wanderka, U. Czubyko, V. Naundorf, D. Mukherji and J. Rösler, *Scripta Mater.* **46** (2002) 235.
- [Schilke 1994] P. Schilke, J. Pepe, and R. Schwant, *Superalloys 718, 625, 706 and Various Derivatives*, TMS, Warrendale, PA (1994) 1.
- [Schulze 2000] C. Schulze, M. Feller-Kniepmeier, *Mater. Sci. & Eng. A.* **281** (2000) 204.
- [Shibata 1996] T. Shibata, Y. Shudo, T. Takahashi, Y. Yoshino and T. Ishiguro, *Superalloys 1996*, TMS, Warrendale, PA (1996) 627.
- [Shibata 1996a] T. Shibata, Y. Shudo and Y. Yoshino, *Superalloys 1996*, TMS, Warrendale, PA (1996) 153.
- [Shibata 1997] T. Shibata, T. Takahashi, Y. Yoshino, M. Kusuhashi, J. Taira and T. Ishiguro, *Superalloys 718, 625, 706 and Various Derivatives*, TMS, Warrendale, PA (1997) 379.
- [Siebörger 2001] D. Siebörger, H. Knake and U. Glatzel, *Mater. Sci. & Eng. A.* **298** (2001) 26.
- [Smith 1953] S. Smith, *Trans. ASM* **45** (1953) 556.
- [Speich 1963] G. Speich, *Trans. AIME* **227** (1963) 754.
- [Sundararaman 1988] M. Sundararaman, P. Mukhopadhyay and S. Banerjee, *Metall. Trans. A.* **19A** (1988) 453.
- [Takahashi 1994] T. Takahashi, T. Ishiguro, K. Orita, J. Taira, T. Shibata and S. Nakata, *Superalloys 718, 625, 706 and Various Derivatives*, TMS, Warrendale, PA (1994) 557.
- [Takahashi 2001] T. Takahashi, T. Shibata, J. Taira and T. Kure, *Superalloys 718, 625, 706 and Various Derivatives*, TMS, Warrendale, PA (2001) 269.
- [Wagner 1982] R. Wagner, *Field-Ion-Microscopy in Materials Science*, Springer-Verlag, Berlin (1982).

- [Wanderka 1995] N. Wanderka, U. Glatzel, Mater. Sci. & Eng. A. **203** (1995) 69.
- [Wanderka 2004] N. Wanderka, V. Naundorf, J. Banhart, D. Mukherji, D. Del Genovesse and J. Rösler, Surf. Interface Anal. **36** (2004) 546.
- [Warren 1998] P. J. Warren, A. Cerezo and G. D. W. Smith, Mater. Sci. & Eng. A. **250** (1998) 88.
- [Xie 1994] X. Xie, Q. Liang, J. Dong, W. Meng et al., Superalloys 718, 625, 706 and Various Derivatives, TMS, Warrendale, PA (1994) 711.
- [Zhang 1996] Y. Zhang and F. Marquis, Superalloys 1996, TMS, Warrendale, PA (1996) 391.

Acknowledgments

I would like to thank the people who contributed to this work, especially

Dr. Nelia Wanderka for her kindness guidance during the study. I feel gratitude for introduction to 3DAP and TEM. Her great joy of getting new results and her encouragement of writing this thesis have strongly motivated me;

Prof. Dr. John Banhart for the possibility to work in his department, for his support of my research and continual interest in success of the thesis and also for proofreading this thesis;

Prof. Dr. Joachim Rösler for taking over the part of the reviewer and for creative advices at the times of project meetings;

Ph. D. Student Dominique Del Genovese for many fruitful discussions, ideas and for a nice collaboration in the project!

Dr. Weiye Chen for his assistance with the finite element calculations;

Dr. Michael-Peter Macht and Dr. Christian Abromeit for valuable advices and critical discussions concerning the text of this thesis;

Dr. Tzanka Kokalova and Dr. Carl Wheldon for their great assistance with written English;

Christiane Förster und Holger Kropf for preparation of excellent EM samples;

Alexander Rack and my roommates Stefan Mechler and Stefan Höring for their willingness to help me in various questions and problems;

Yvonne Herzog and Christian Abromeit for their support and help with various bureaucracy;

Jörg Bajorat for technical support;

Ingrid Dencks, Elvira Garcia-Matres and Andre Heinemann ... for a sincere sense of humour 😊.

All members of the group for the nice attitude. It was a real pleasure to work together with you!

My friends Svetlana, Alexander, Alexei, Egor, Olga and Eugen, Ilona and Yuriy, whom I have met in Berlin.

And primarily my sister and my parents, who helped me to live in Germany being far away from here.

This work was financially supported by the Deutsche Forschungsgemeinschaft (DFG) under WA 1378/5-1 as a project together with TU Braunschweig under Prof. Dr. J. Rösler and Ph.D. Student D. Del Genovese.